ENSEMBLE FORECASTING OF CORONAL MASS EJECTIONS USING THE WSA-ENLIL WITH CONED MODEL

THESIS

Daniel J. Emmons II, Captain, USAF
AFIT/APPLPHY/ENP/12-M04

DEPARTMENT OF THE AIR FORCE
AIR UNIVERSITY

AIR FORCE INSTITUTE OF TECHNOLOGY

Wright-Patterson Air Force Base, Ohio

AFIT/APPLPHY/ENP/12-M04

ENSEMBLE FORECASTING OF CORONAL MASS EJECTIONS USING THE WSA-ENLIL WITH CONED MODEL

THESIS

Presented to the Faculty

Department of Engineering Physics

Graduate School of Engineering and Management

Air Force Institute of Technology

Air University

Air Education and Training Command

in Partial Fulfillment of the Requirements for the

Degree of Master of Science in Applied Physics

Daniel J. Emmons II, BS

Captain, USAF

March 2012

AFIT/APPLPHY/ENP/12-M04

ENSEMBLE FORECASTING OF CORONAL MASS EJECTIONS USING THE WSA-ENLIL WITH CONED MODEL

Daniel J. Emmons II, BS
Captain, USAF

Approved:

Lt Col Ariel O. Acebal (Chairman)	6 MARCH 2012 Date
William F. Bailey, PhD (Member)	6 Mar 12 Date
Antti A. Pulkkinen, PhD (Member)	2/24/2012 Date
Aleksandre Taktakishvili, PhD (Member)	2/27/2012 Date

Abstract

The combination of the Wang-Sheeley-Arge (WSA) coronal model, ENLIL heliospherical model version 2.7, and Coned Model version 1.3 (WSA-ENLIL with Coned Model) was employed to form ensemble forecasts for 15 halo coronal mass ejections (CMEs). The input parameter distributions were formed from 100 sets of CME cone parameters derived from the Coned Model. The Coned Model employed image processing along with the bootstrap approach to automatically calculate cone parameter distributions from SOHO-LASCO imagery based on techniques described by *Pulkkinen et al.* [2010]. The cone parameter distributions were used as input to WSA-ENLIL to calculate the temporal evolution of the CMEs, which were analyzed to determine the propagation times to the L_1 Lagrangian point and the maximum K_p indices due to the impact of the CMEs on the Earth's magnetosphere. The *Newell et al.* [2007] maximum K_p index formula was employed to calculate the maximum K_p indices based on the solar wind parameters near Earth. The propagation time forecasts outperformed a number of reference models, including the Shock Time of Arrival (STOA) model and the Interplanetary Shock Propagation Model (ISPM), which are both currently used by the Air Force Weather Agency (AFWA). The maximum K_p ensemble forecasts performed the same as the ENLIL "single-shot" best estimates. The mean absolute forecast errors were calculated to be 9.1 *hours* for the propagation time and 1.7 for the maximum K_p index. The forecasts for 5 of the 15 events had accuracy such that the actual propagation time lay within the ensemble average plus or minus one standard deviation, and 8 of the 15 events had the actual propagation time within the range of the ensemble. The maximum K_p index forecasts for 10 of the 15 events had the actual maximum K_p index inside the range of the ensemble.

The analysis was repeated using Coned Model version 1.2, which resulted in a set of propagation times less accurate than Coned Model version 1.3, and maximum K_p indices slightly more accurate. The model robustness was analyzed by varying input parameters other than the cone parameters, and the model was found to be robust with forecast changes of less than 5% due to the parameter variations.

Acknowledgements

First, I would like to thank my wife for putting up with me even though I locked myself in the office for most of the last year. Thanks for not leaving me.

I would like to thank Lt Col Acebal for being such a great advisor and mentor. Thanks for making sure that I put my full effort into this project, and for helping me with all the problems along the way. It's been a pleasure to work for you, and I am very grateful for all the time and effort you spent teaching me about space weather and guiding me through this research.

I would also like to thank the folks at CCMC, especially Antti and Sandro, for giving me the opportunity to work on a great project with a great group of people. I had a wonderful time working with you all, and I really appreciate all of the time and effort you spent preparing this project for me and guiding me along the way.

I would also like to thank Dr. Bailey for introducing me the wonderful world of plasma physics. Thanks for passing on your knowledge of the great MHD equations, and for your willingness to help.

Last, but not least, I would like to thank my family for all of their support and encouragement.

Daniel J. Emmons II

Table of Contents

Page

List of Figures

Figure Page

List of Tables

Table Page

Table Page

ENSEMBLE FORECASTING OF CORONAL MASS EJECTIONS USING THE WSA-ENLIL WITH CONED MODEL

I. Introduction

Coronal mass ejections (CMEs) are the cause of the most severe geomagnetic storms [*Gosling*, 1993]. Geomagnetic storms can cause a variety of problems at Earth including radio wave propagation disruption [*Tascione*, 1994], degradation of satellite performance [*Afraimovich et al.*, 2003], and disruption of electrical systems on the Earth's surface [*Boteler et al.*, 1998]. For these reasons, the United States Air Force and NASA have a great interest in predicting the arrival times and impacts of CMEs at Earth.

A number of models have been developed to estimate the propagation time of CMEs. Some of the earlier models were shock propagation models based on type II meter wave burst measurements, such as the Shock Time of Arrival (STOA) model [*Dryer*, 1974] and the Interplanetary Shock Propagation Model (ISPM) [*Smith and Dryer*, 1990]. Both STOA and ISPM are currently employed by the Air Force Weather Agency (AFWA) to predict the arrival times of CMEs. Empirical forecast models have been developed recently, including the model developed by *Gopalswamy et al.* [2001] which treats the CME as a kinematic object which experiences accelerations or decelerations to match the ambient solar wind speed at distances near 1 AU.

The most current and advanced method of forecasting CMEs is based on numerically solving the magnetohydrodynamic (MHD) equations governing the motion of the CME over time. One example of this type of model is ENLIL, a time-dependent three-dimensional model which solves the magnetohydrodynamic equa-

tions for plasma mass, momentum, magnetic field, and energy density using a modified Total-Variation-Diminishing Lax Friedrichs finite difference approximation [*Odstrčil and Pizzo*, 1999]. ENLIL can accept the output of the Wang-Sheeley-Arge (WSA) coronal model for use as the boundary conditions in the finite difference computations. The WSA model calculates the background solar wind solution based on solar magnetogram measurements [*Arge and Pizzo*, 2000]. ENLIL can also accept the output of the Cone Model to initialize the CME velocity, angular width, and axis of propagation.

The Cone Model, developed by *Zhao et al.* [2002], assumes that the CME has the shape of a cone with constant angular width, propagates in a radial direction, and experiences isotropic expansion. A technique to manually determine the cone parameters from SOHO/LASCO imagery was developed by *Xie et al.* [2004]. Previous analyses have been completed using the analytic Cone Model along with WSA-ENLIL to forecast the propagation times and impacts of CMEs, and have showcased the effectiveness of the WSA-ENLIL with Cone Model combination (e.g. *Taktakishvili et al.* [2009], *Taktakishvili et al.* [2010]).

The analytic Cone Model relies on a manual determination of the CME outer boundary from LASCO imagery, which is susceptible to user bias. The development of the Coned Model, an automated version of the Cone Model, removed the user from the process [*Pulkkinen et al.*, 2010]. The Coned Model uses image processing to automatically determine the location of the CME mass from LASCO imagery, and then calculates a distribution of possible cone parameters using a bootstrap approach. The distribution of cone parameters represents a dynamic quantification of the uncertainty of the cone parameters based on LASCO imagery, and will vary for each event as the LASCO images vary for each event.

The performance of the WSA-ENLIL with Coned Model has been analyzed with

the median values of the cone parameter distributions used as input for a single WSA-ENLIL run. The *Taktakishvili et al.* [2011] analysis showed that the analytic Cone Model and the Coned Model (automatic Cone Model) had reasonable agreement in the forecasts with a mean absolute propagation time forecast error of 6.9 $hours$ for the analytic Cone Model and 11.2 $hours$ for the Coned Model. The performance of the WSA-ENLIL with Coned Model version 1.2 was analyzed by *Falkenberg et al.* [2011], with the conclusion that the CME velocity and angular width were underestimated by the Coned Model. Coned Model version 1.3 is the most current version of the Coned Model, and has included a modification in the optimization routine to increase the CME velocity and width estimations following the results of the *Falkenberg et al.* [2011] analysis.

With the production of the cone parameter distributions from the Coned Model readily available, an ensemble forecast can be calculated. An ensemble forecast is a collection of two or more forecasts which verify at the same time [*Sivillo et al.*, 1997].The weather community has long known of the improvement in forecast accuracy due to the use of ensemble forecasting [*Leith*, 1974]. Ensemble forecasting also allows for a quantification of forecast uncertainty based on uncertainty in the measurements of the initial conditions, which is impossible for single forecasts. This quantification of forecast uncertainty could provide important additional information to operational forecasts of CMEs.

This analysis applied the ensemble forecasting technique to 15 halo-CMEs using the WSA-ENLIL with Coned Model. The ensembles were created from 100 sets of initial states (cone parameters), derived from Coned Model version 1.3, which were used as input to WSA-ENLIL version 2.7 to obtain distributions of future states. The distributions of future states were analyzed to produce distributions of propagation times to the L_1 Lagrangian point and distributions of the maximum K_p indices due

to the impact of the CME on the Earth's magnetosphere.

The relative performance of the propagation time forecasts were analyzed by comparing the ensemble forecasts to a number of reference models. Two of the reference models, STOA and ISPM, were used as reference models to determine the most accurate model to use for future AFWA operational forecasts of CMEs. The relative performance of the maximum K_p forecasts were compared to the results of single ENLIL forecasts based on the best estimates of the cone parameters.

The analysis was repeated using Coned Model version 1.2 to determine the most accurate version of the Coned Model. The robustness of the WSA-ENLIL with Coned Model was also analyzed by varying input parameters other than the cone parameters and calculating the amount of change in the forecasts due to the variations in the input parameters.

The remainder of this document is structured as follows: Chapter 2 provides the background for this analysis, including a discussion on CMEs, the WSA-ENLIL with Coned Model, and ensemble forecasting. Chapter 3 provides the methodology used in the analysis. The results are displayed and discussed in Chapter 4. Finally, Chapter 5 has the conclusion of the analysis.

II. Background

This chapter provides the background required to understand this analysis. First, coronal mass ejections are introduced. Then, the particulars of the models composing WSA-ENLIL with Coned Model are described. Next, the previous analyses completed using ENLIL are briefly mentioned. Finally, an ensemble forecasting primer is presented.

2.1 Coronal Mass Ejections

2.1.1 Physical Characteristics

Coronal Mass Ejections (CMEs) are the largest-scale eruptions in our solar system, in terms of spatial extent. They are characterized by an ejection of plasma and associated magnetic field from the solar corona into interplanetary space. The original definition of a CME stated that a CME is an observable change in the coronal structure that involves the creation and outward motion of a discrete, white-light structure in the coronagraph field of view [*Hundhausen et al.*, 1984]. Further research discovered that CMEs also emit light in the extreme ultraviolet, x-ray, and radio portions of the spectra. The visible electromagnetic radiation from CMEs is created by Thompson scattered radiation by free electrons in the corona.

CMEs appear to have many shapes, but much of the difference is due to the projection of the CMEs on the measurement sensors. The same CME will appear to have a different shape if viewed from a different angle. Halo-CMEs are Earth-directed CMEs that appear to form a halo around the Sun, as viewed from Earth. There are two main classification of CME shape: narrow and normal. Narrow CMEs appear to have jet-like structures and are usually located at at open magnetic field lines such as coronal holes. The angular width of the narrow CMEs is usually around 10° [*Chen*,

2011].

Normal CMEs are typically described as having a three-part structure which consists of a bright frontal loop, followed by a dark cavity and a bright core [*Illing and Hundhausen*, 1985]. The bright core is composed of the erupting filament [*House et al.*, 1981]. The angular width of a normal CME is greater than 10°. Coronagraph images of the two CME structures are displayed in Figure 1.

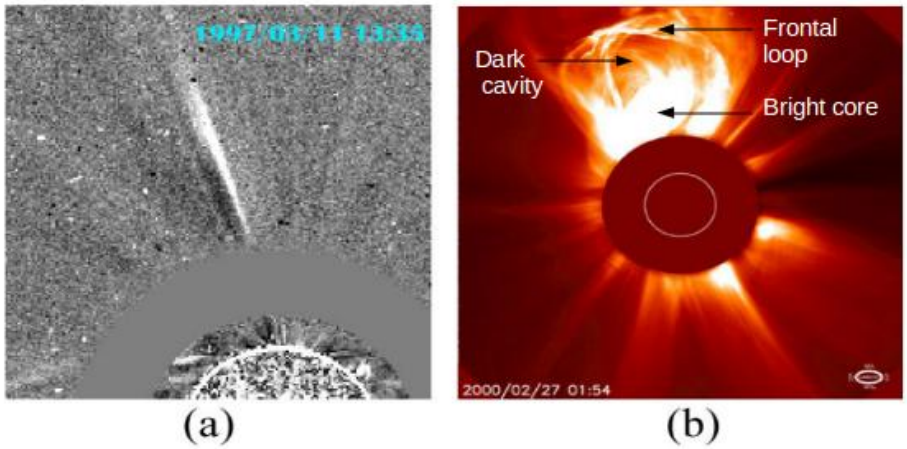

Figure 1. Images of the two typical CME structures adapted from *Chen* [2011]: (a) Narrow CME, (b) Normal CME with three part structure.

The standard three-part structure of a normal CME is only observed in approximately 30% of CMEs [*Webb and Hundhausen*, 1987]. Many of the CMEs that do not contain the three-part structure will contain two of the parts. The variation in CME structure has to do with the complex creation of the CMEs as well as the ambient conditions during the eruption of the CME.

The mass of a CME is typically in the range of $10^{11} - 4 \times 10^{13}\, kg$, with an average mass of $3 \times 10^{12}\, kg$ (*Jackson* [1985], *Gopalswamy and Kundu* [1992], *Hudson et al.* [1996]). The mass can be estimated using the Thompson scattering formulae applied to the coronagraph images of CMEs [*Chen*, 2011].

The occurrence rate of CMEs follows the solar cycle with the peak of CME occurrence lagging behind the peak of solar activity by $6 - 12$ months [*Raychaudhuri*, 2004]. During the solar minima the CME occurrence rate is between 0.5 to 2 per day, while during solar maxima the occurrence rate is between 6 to 8 per day (*Gopalswamy et al.* [2003], *Yashiro et al.* [2004], *Robbrecht et al.* [2009]). Solar cycle 23 was found to produce over 13,000 CMEs.

The projected velocity of a CME (projected onto the two-dimensional plane of a measurement device) is usually in the range of $20\,km/s$ to $> 2000\,km/s$ [*Chen*, 2011]. A CME will occasionally reach velocities of up to $3500\ km/s$. The average CME velocity during solar minimum is approximately $300\ km/s$, and is approximately $500\ km/s$ during solar maximum [*Yashiro et al.*, 2004]. The average velocity of halo CMEs is approximately $960\ km/s$, which is much faster then the velocity of normal CMEs [*Chen*, 2011].

The total energy of a CME, including kinetic and potential (gravitational) energies, is typically in the range of $10^{22} - 10^{25}\ J$ [*Emslie et al.*, 2004]. A one-megaton nuclear detonation can release energy on the order of $10^{15}\,J$ (Hiroshima's "Little Boy" bomb produced around $5 \times 10^{13}\ J$), which implies that the energy found in a CME is on the order of $10^7 - 10^{10}$ one-megaton nuclear detonations.

CMEs are often associated with solar flares, but many flares are not associated with CMEs. Approximately 70% of C-class, 44% of M-class, and 10% of X-class flares are not associated with CMEs (*Wang and Zhang* [2007], *Yashiro et al.* [2005]). Associated flares and CMEs are thought to be different parts of the same magnetic eruption [*Zhang et al.*, 2001].

2.1.2 Eruption

The typical energy densities found in a CME are in the range of $10^{-2} - 10\ J/m^3$ [*Chen*, 2011]. Table 1 displays the different sources of energy found in the solar corona along with estimations of the typical values observed. It is obvious, from the energy sources, that the energetic CMEs must obtain their energy from the magnetic energy.

The CME energy comes from the release of magnetic energy by a process called magnetic reconnection. Most CMEs are formed by this rapid release of magnetic energy in the corona. But, very weak CMEs may obtain their energy from thermal and gravitational potential energies. The thermal energy can be converted to CME energy by the work of a pressure gradient, and the gravitational potential energy can be converted to CME energy by the buoyancy force [*Chen*, 2011].

Table 1. A list of the coronal energy sources including kinetic, thermal, gravitational and magnetic, adapted from *Forbes* [2000].

Form of Energy	**Energy Density ($\mathbf{J/m^3}$)**	**Observed Averaged Value**
Kinetic ($\frac{1}{2}m_p n V^2$)	8×10^{-4}	$n = 10^{15} m^{-3}$, $V = 1\ km/s$
Thermal (nkT)	1×10^{-2}	$T = 10^6\ K$
Gravitational ($nm_p gh$)	5×10^{-2}	$h = 10^5\ km$
Magnetic ($B^2/2\mu_0$)	40	$B = 10^{-2}\ T$

The manner in which the magnetic energy is released depends on a number of factors including CME type (narrow or normal) and the magnetic topology before and during the eruption. Narrow CMEs are believed to be formed as the result of a magnetic reconnection between small magnetic dipoles [*Wang et al.*, 1998]. This could be due to the reconnection of dipoles such as a coronal loop and an open magnetic field in the coronal holes.

Normal CMEs are most likely formed from an erupting flux rope system [*Chen*, 2011]. A flux rope can be thought of as a twisted magnetic flux tube, and is the result

of a complex magnetic field structure which becomes twisted. Before eruption, the flux rope may be supporting a filament which is kept in equilibrium by the overlying magnetic field of the corona. An instability in the magnetic structure can cause the flux rope to rise which will form additional instabilities in the wake of the rising flux rope. Antiparallel magnetic fields will then be able to reconnect below the flux rope which will lead to a solar flare if the reconnection takes place quickly [*Chen*, 2011]. The magnetic reconnection below the flux rope removes the constraint holding the flux rope, and the flux rope will erupt and propagate radially outwards after the reconnection takes place.

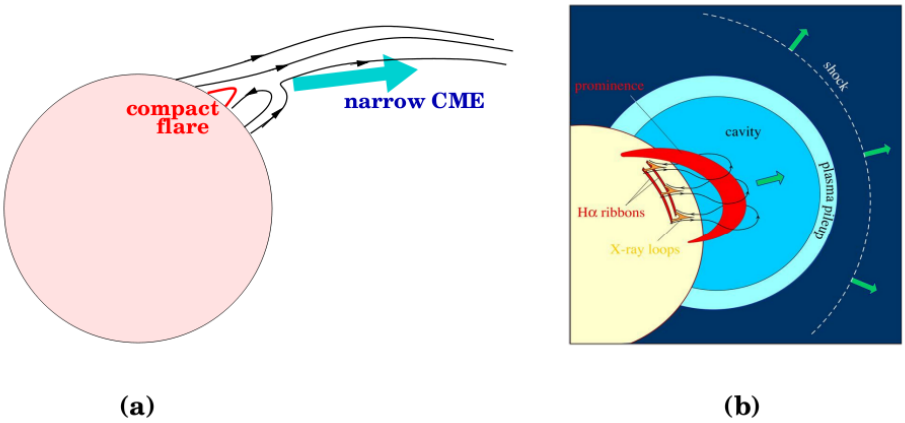

Figure 2. Diagrams of CME eruptions for narrow and normal CMEs: (a) Narrow CMEs, adapted from *Chen* [2011], (b) Normal CMEs, adapted from *Forbes* [2000].

The shock formed by the erupting flux rope forms the frontal loop of the CME. If the reconnection does not take place quickly enough to create a solar flare, the CME may still erupt due to a loss of equilibrium or MHD instabilities [*Chen*, 2011]. This description of CMEs is known as the standard model for CMEs/flares. The standard model helps to describe the association of solar flares with CMEs, and explains why some CMEs are associated with flares while others are not. Figure 2 shows a schematic

model of the two different types of eruptions.

2.1.3 Propagation

The majority of CMEs follow a three stage process: initiation, impulsive acceleration, and propagation [*Zhang et al.*, 2001]. The initiation phase is characterized by slow radial propagation at speeds of less than 80 km/s for a period of about 10 minutes. The CMEs then undergo an impulsive acceleration which can last from minutes to tens of minutes and experience accelerations in the range of $100 - 500\ m/s^2$. The propagation phase is characterized by a nearly constant velocity with a relatively small amount of acceleration or deceleration.

After the CME is ejected into the interplanetary medium, it is known as an interplanetary coronal mass ejection (ICME). There are two main methods used to describe the propagation phase of an ICME. The first method is an analytical method which uses ordinary differential equations to describe the motion and geometry of the ICME as a function of time as it is subjected to accelerations, decelerations, and deformation forces [*Forbes et al.*, 2006]. This method treats the CME as a kinematic object, and propagates the object throughout space while accounting for the different forces that the object experiences while propagating. The second method involves simulating the magnetohydrodynamics (MHD) of the CME and its surroundings. This is a computational technique which approximates the solution to the MHD partial differential equations governing the plasma over time [*Forbes et al.*, 2006].

While propagating from the Sun to the Earth, slow moving CMEs accelerate while fast moving CMEs decelerate until they reach a speed similar to the speed of the ambient solar wind once they arrive at $1\,AU$ [*Gopalswamy et al.*, 2000]. Employing the analytical method, *Gopalswamy et al.* [2000] derived an empirical formula to describe the average acceleration of an ICME required to reach the measured speed at $1\ AU$,

as a function of the plane-of-sky (POS) measured speed, v, using coronagraph images as

$$a\,[m/s^2] = 1.41 - 0.0035v\,[km/s]. \tag{1}$$

As the CME propagates, it also expands. *Owens et al.* [2005] empirically described the radial expansion of an ICME by

$$V_{expansion}\,[km/s] = 0.266v - 70.61\,[km/s] \tag{2}$$

where $V_{expansion}$ is the radial expansion velocity of the CME, and v is the velocity of the leading edge of the CME. The typical radial extent of a CME, at a distance of 1 AU, has been measured to be between 0.2 and 0.25 AU [*Klein and Burlaga*, 1982].

Not only does a CME expand radially as it propagates, its cross-sectional shape also changes [*Forbes et al.*, 2006]. CMEs have an approximately circular cross-section when they are first ejected, but the forces they experience while propagating are different in the direction of propagation than in the directions perpendicular to propagation. The difference in forces causes a CME to take the cross-sectional shape of an ellipse as it reaches distances around 1 AU. The amount of ellipticity will vary depending on CME characteristics and interplanetary conditions. The ratio of major to minor axes, as measured at 1 AU, are believed to lie between 2 and 4 [*Forbes et al.*, 2006].

The MHD simulation method involves approximating the solution to the following

partial differential equations known as the magnetohydrodynamic equations:

$$\begin{aligned} \frac{\partial}{\partial t}(\rho) + \nabla \cdot (\rho \mathbf{V}) &= 0, \\ \frac{\partial}{\partial t}(\rho \mathbf{V}) + \nabla \cdot (\rho \mathbf{V}\mathbf{V}) &= -\nabla(P) + \nabla \cdot \left(\frac{\mathbf{B}\mathbf{B}}{\mu} \right) + \rho \frac{GM_{sun}}{r^2}, \\ \frac{\partial}{\partial t}(E) + \nabla \cdot (E \mathbf{V}) &= -p \nabla \cdot (\mathbf{V}), \\ \frac{\partial}{\partial t}(\mathbf{B}) &= \nabla \times (\mathbf{V} \times \mathbf{B}), \end{aligned} \tag{3}$$

where ρ is the mass density, $\mathbf{V}$ is the average flow velocity, P is the total pressure (including magnetic and thermal pressures), $\mathbf{B}$ is the magnetic field, μ is the permeability, G is the gravitational constant, M_{sun} is the solar mass, p is the thermal pressure, and E is the thermal energy density ($E = \frac{p}{\gamma - 1}$ where γ is the ratio of specific heats) [*Odstrcil*, 2003].

Two additional continuity equations must also be solved to conserve mass and magnetic field polarity injected by the CME:

$$\begin{aligned} \frac{\partial}{\partial t}(\rho_c) + \nabla \cdot (\rho_c \mathbf{V}) &= 0, \\ \frac{\partial}{\partial t}(\rho_p) + \nabla \cdot (\rho_p \mathbf{V}) &= 0, \end{aligned} \tag{4}$$

where ρ_c is the density of injected CME material and ρ_p is the density of the magnetic field polarity [*Odstrcil*, 2003]. This allows the simulation to trace the magnetic polarity and mass of the CME over time.

2.1.4 Impact

The magnetic field associated with CMEs has a large effect on the Earth's magnetosphere, and can be the cause of severe geomagnetic storms. The magnitude of the impact on the magnetosphere depends on the direction and magnitude of the

magnetic field associated with the CME. If the CME has a southward magnetic field (relative to Earth), the impact will be the greatest.

One method used to describe the impact of a CME on the magnetosphere is to calculate the change in the magnetopause standoff distance. The outer boundary of the Earth's magnetosphere is approximately located at a distance where the pressure of the solar wind equals the magnetic pressure of the Earth's magnetic field. The radial distance where the dynamic and magnetic pressures are equal, measured from the center of the Earth, is called the magnetopause standoff distance [*Prölss*, 2004]. A geomagnetic storm produced by a CME will compress the Earth's magnetosphere and decrease the magnetopause standoff distance by increasing the dynamic pressure of the solar wind. The amount of compression can be calculated by determining the radial distance at which the pressure from the Earth's magnetic field balances the dynamic pressure from the CME.

While the magnetopause standoff distance provides a decent estimate of the combination of solar wind density and speed due to a CME, it does not necessarily provide a good estimate of the magnitude of the associated geomagnetic storm. The K index is a ground based measurement of disturbances in the Earth's magnetic field relative to calm geomagnetic conditions, and provides a good indication of the general level of magnetic activity caused by solar wind [*Tascione*, 1994]. The K index measures the variation in the horizontal component of the Earth's magnetic field in mid-latitudes using three hour intervals. It uses a semi-logarithmic scale with integer values ranging from 0-9. A K index of one indicates calm magnetic conditions, and five or higher indicates a geomagnetic storm. A K index of nine represents the most severe geomagnetic storm. The planetary K index (K_p index) is calculated from the combination of 12 K index measurements made at different locations worldwide between geomagnetic latitudes of 48° and 63° [*Tascione*, 1994]. The K_p index is used to describe the

worldwide magnitude of a geomagnetic storm.

Newell et al. [2007] showed that the K_p index can be correlated to solar wind parameters by the use of the coupling function

$$\frac{d\Phi_{MP}}{dt} = v^{4/3} B_T^{2/3} sin^{8/3}(\theta_c/2) \tag{5}$$

where $\frac{d\Phi_{MP}}{dt}$ is the coupling function, v is the speed at which the interplanetary magnetic field (IMF) lines approach the magnetopause and can be approximated by the solar wind speed, B_T is the magnitude of the IMF, and θ_c is the IMF clock angle. The IMF clock angle is defined by $\theta_c = arctan(B_y/B_z)$, where B_z refers to the north-south component of the IMF relative to Earth and B_y refers to the component of the IMF perpendicular to both the Sun-Earth line and the north-south line. $\theta_c = 0$ corresponds to a completely northward facing IMF, while $\theta_c = \pi$ corresponds to a completely southward facing IMF.

The K_p index can be calculated from solar wind measurements by using the coupling function along with the appropriate slope fitting the coupling function to the observed K_p index. With the appropriate slope and intercept, the *Newell et al.* [2007] K_p formula is

$$K_p = 0.0002947 \frac{d\Phi_{MP}}{dt} + 1 = 0.0002947 v^{4/3} B_T^{2/3} sin^{8/3}(\theta_c/2) + 1, \tag{6}$$

where v is in km/s and B_T is in nT. This allows for an estimation of the magnitude of a geomagnetic storm strictly from examining solar wind parameters, and provides a tool for CME forecasters to estimate the impact of a CME before the CME arrives.

2.1.5 Measurement

The initial discovery of CMEs occured in the early 1970's (*Rycroft and Runcorn* [1973], *MacQueen et al.* [1974]), but the effects of CMEs have been observed for thousands of years [*Howard*, 2006]. The first effect of CMEs observed by humans was the creation of the aurorae. Sightings of aurorae have been reported in many classical pieces of literature including the Old Testament [*Howard*, 2006].

Even though the effects of CMEs were observed for thousands of years, it was not until the 1970's that the first CME was actually observed. On 13-14 Dec 1971, the first CME was optically observed by the coronagraph onboard NASA's Orbiting Solar Observatory 7 (OSO-7) [*Rycroft and Runcorn*, 1973]. A coronagraph is a device which blocks the direct light of the Sun, by the use of an occulting disc, so that the surrounding light structures can be viewed more clearly. The first observed CME is displayed in Figure 3.

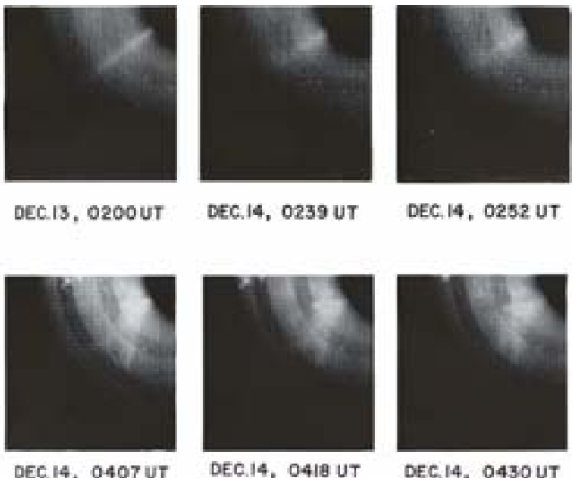

Figure 3. Images of the first CME optically observed, measured during 13-14 Dec 1971, adapted from *Howard* [2006].

A currently deployed coronagraph is onboard ESA (European Space Agency) and NASA's Solar and Heliospherical Observatory (SOHO), which was launched in 1995.

SOHO contains the Large Angle and Spectrometric Coronagraph (LASCO), which can produce images of the solar corona in the visible spectrum from 1.1 to 32 solar radii. LASCO is separated into three different telescopes which have different ranges of observations. The C1 telescope has an observation range of 1.1 to 3 solar radii, the C2 telescope has a range of 1.5 to 6 solar radii, and the C3 telescope has a range of 3 to 32 solar radii. An example of a difference image produced by LASCO C2 is displayed in Figure 4. Difference images show the difference between sequential images, and are used to locate transient events (such as CMEs) while removing the unchanging background features. The difference images from LASCO imagery are used to observe the location of the plasma composing CMEs, and can be used to estimate the velocity of the CMEs.

SOHO is located at the L_1 Lagrangian point, which is the point between the Earth and Sun where the Earth and Sun's gravitational forces are equal. This point is located on the Sun-Earth line, approximately 1.5 million km from the Earth and 148.5 million km from the Sun. This is a prime location to observe Earth directed solar phenomena, such as CMEs.

NASA's Solar Terrestrial Relations Observatory (STEREO) was launched in 2006, and is comprised of two satellites orbiting on opposite sides of the Sun. STEREO contains an instrument suite named Sun Earth Connection Coronal and Heliospheric Investigation (SECCHI), which contains an extreme ultraviolet imager, two coronagraphs, and a heliospheric imager used to study the three dimensional evolution of a CME. The locations of the STEREO satellites allow for CME forecasters to accurately estimate the propagation axes of Earth-directed CMEs. STEREO has been a very important tool for stereographic imaging of CME's, and due to the orbits of the two satellites (drifting away from Earth), we will eventually lose signal and lose the important tool.

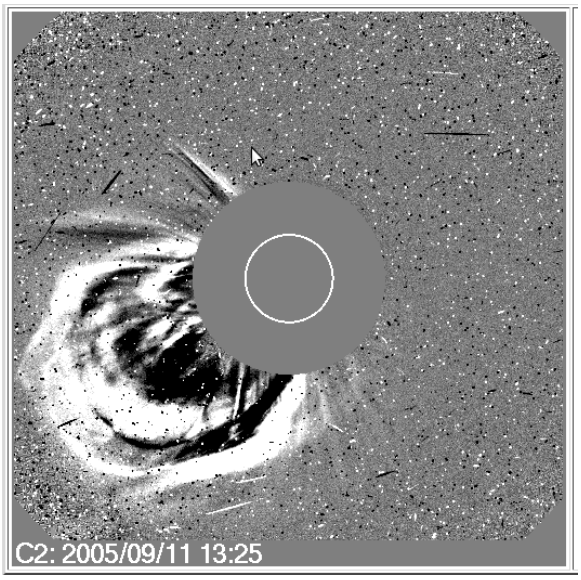

Figure 4. The LASCO C2 difference image of the 11 Sept 2005 CME, which shows the location of the plasma forming the CME.

California Institute of Technology and NASA's Advanced Composition Explorer (ACE) satellite was launched in 1997 and has a variety of instruments used to record the solar wind parameters. The two sensors of particular interest to analyzing CMEs are the MAG instrument and the Solar Wind Electron Proton Alpha Monitor (SWEPAM). The MAG instrument measures the interplanetary magnetic field direction and magnitude. SWEPAM is used to detect solar wind electron and ion directions and energies. ACE is also located at the L_1 Lagrangian point, so the solar wind data collected by ACE are used as the solar wind conditions for Earth. The arrival time of a CME and the impact caused by a CME can be determined from ACE solar wind measurements.

2.2 WSA-ENLIL with Coned Model

The WSA-ENLIL with Coned Model approximates solutions to the MHD equations governing plasma mass, momentum, energy density, and magnetic field. ENLIL

can take input from Coned Model output, and will accept boundary conditions from the Wang-Sheeley-Arge (WSA) coronal model. Therefore, in order to understand the WSA-ENLIL with Coned Model, we must examine ENLIL, the Coned Model, and the WSA model.

2.2.1 Coned Model

The Cone Model assumes a CME has the shape of a cone, and uses this assumption to solve for three different parameters describing the orientation of the cone: the angular width, the radial velocity, and the propagation axis. In 2009, *Pulkkinen et al.* created the Coned Model, which calculates the cone parameters from a time series of LASCO C3 images automatically. The Coned Model uses image processing to automatically determine the location of the CME mass from LASCO imagery. The image processing is composed of three steps: First, the contrast of the image is adjusted by linearly mapping the original values to values covering the full grayscale intensity range. Second, the image is filtered using a median filter. A 25×25 neighborhood is used to compute the median value assigned to individual pixels. Third, the pixels of the filtered image are converted to binary values based on a brightness threshold [*Pulkkinen et al.*, 2010]. An example of this process is displayed in Figure 5.

The cone parameters of interest are displayed in Figure 6. The (y', z') plane is the plane of sky (POS) with x' pointing towards Earth. The angle α is the direction of propagation of the CME along the (y', z') plane. The angle θ defines the rotation of the cone off of the (y', z') plane, and can be described as the angle between the x' and x axes. The angle ω is the opening half-angle of the cone. x_0 is the initial distance of the leading edge of the cone in the rotated coordinates (x, y, z), and v is the velocity of the front of the cone. Δt refers to the time interval between the propagation of the CME from x_0 to x.

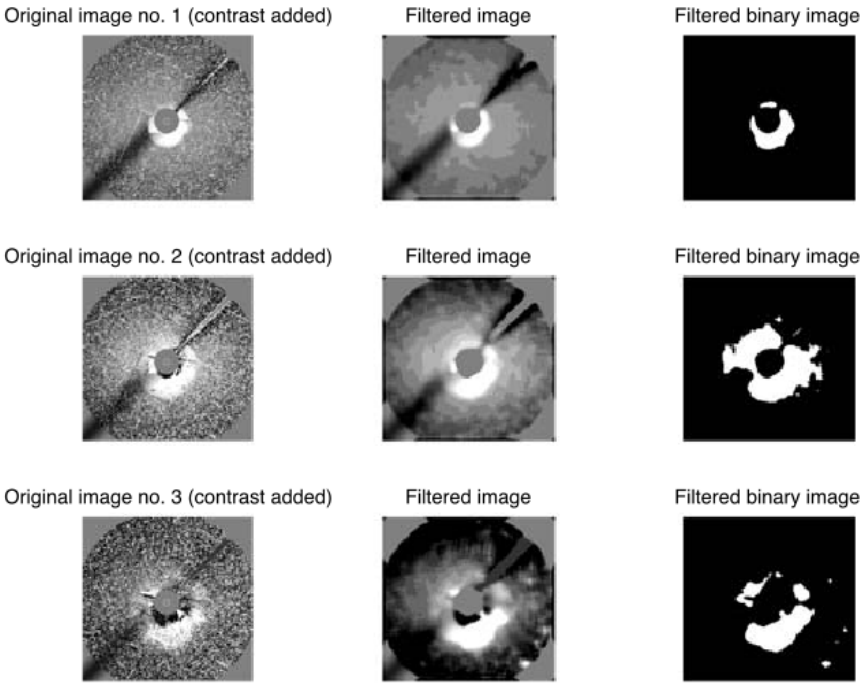

Figure 5. The Coned Model image processing technique applied to a time series of LASCO C3 images of the 13 Dec 2006 CME, used to determine the location of the mass composing a CME. This figure was adapted from *Pulkkinen et al.* [2010].

After the location of the mass of the CME is determined from the image processing, the cone parameters can be inverted from the data. First, the center of mass is computed by

$$y'_m = \frac{1}{N}\sum_i^N y'_i, \tag{7}$$

$$z'_m = \frac{1}{N}\sum_i^N z'_i, \tag{8}$$

where (y', z') refers to the POS, and the summation is over all data points containing the CME mass [*Pulkkinen et al.*, 2010]. The direction of propagation, α, is then calculated by

$$\alpha = tan^{-1}(z'_m/y'_m). \tag{9}$$

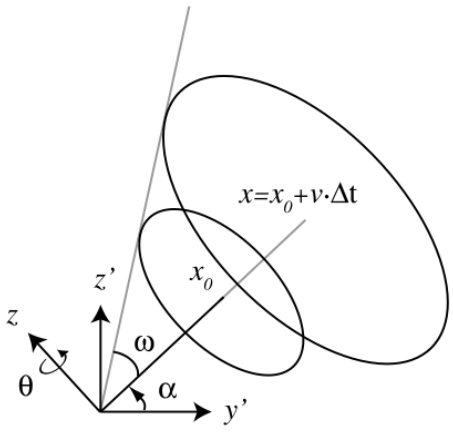

Figure 6. A representation of the cone parameters of interest for the Coned Model, adapted from *Pulkkinen et al.* [2010].

Next, the data are rotated by an angle of $-\alpha$. An inversion scheme is then employed to determine the remaining parameters $\{\theta, \omega, x_0, v\}$. The inversion problem is

$$\min_{\{\theta,\omega,x_0,v\}} \left[\sum_{i}^{N} \sqrt{(\hat{y}_i' - y_i')^2 + (\hat{z}_i' - z_i')^2} + \mu|\omega - \omega_0| \right], \tag{10}$$

where $(\hat{y}_i', \hat{z}_i')$ are the coordinates of the cone front, (y_i', z_i') are the coordinates of the CME mass data, μ is the Lagrange multiplier and ω_0 is a climatological opening half-angle [*Pulkkinen et al.*, 2010]. The coordinates $(\hat{y}', \hat{z}')$ are computed by

$$
\begin{aligned}
&\mathbf{R}_z^T(\theta) \cdot \begin{pmatrix} x \\ x\tan(\omega)\cos(\gamma) \\ x\tan(\omega)\sin(\gamma) \end{pmatrix} \\
&= \begin{pmatrix} x\cos(\theta) - x\tan(\omega)\cos(\gamma)\sin(\theta) \\ x\sin(\theta) + x\tan(\omega)\cos(\gamma)\cos(\theta) \\ x\tan(\omega)\sin(\gamma) \end{pmatrix} \\
&= \begin{pmatrix} \hat{x}'(\gamma) \\ \hat{y}'(\gamma) \\ \hat{z}'(\gamma) \end{pmatrix},
\end{aligned}
\tag{11}
$$

where the operator $\mathbf{R}_z^T(\theta)$ rotates the cone by angle θ about the z-axis, and $x = x_0 + v\Delta t$, where v is the velocity of the cone front and Δt is the time of propagation from x_0 to x [*Pulkkinen et al.*, 2010]. The CME is assumed to be propagating towards Earth with a constant velocity between difference images. The coordinates $(\hat{y}_i', \hat{z}_i')$ in Equation 10 are obtained from $(\hat{y}'(\gamma), \hat{z}'(\gamma))$ by selecting the angle γ which minimizes the distance to the data point (y_i', z_i') [*Pulkkinen et al.*, 2010].

Equation 10 is solved by using a stochastic tunneling approach for optimization [*Wenzel and Hamacher*, 1999]. The climatological value ω_0 was set to 30° based on statistical CME data analyzed by *Cyr et al.* [2000] and *Yashiro et al.* [2004]. The heliocentric latitude and longitude, λ and ϕ, are determined by

$$
\begin{aligned}
\lambda &= \frac{\pi}{2} - \cos^{-1}(\sin(\theta)\sin(\alpha)), \\
\phi &= \tan^{-1}(\tan(\theta)\cos(\alpha)),
\end{aligned}
\tag{12}
$$

where the heliocentric latitude and longitude are angles relative to the ecliptic plane.

To determine the confidence intervals for the calculated cone parameters, a bootstrap approach is employed. The bootstrap approach randomly creates subsets of the original data set and calculates the cone parameters for each subset separately. An example of the cone parameters obtained using the bootstrap approach is displayed in Figure 7. The distributions in this example were determined by calculating the cone parameters from 300 randomly selected points per image, and then repeating the analysis 400 times.

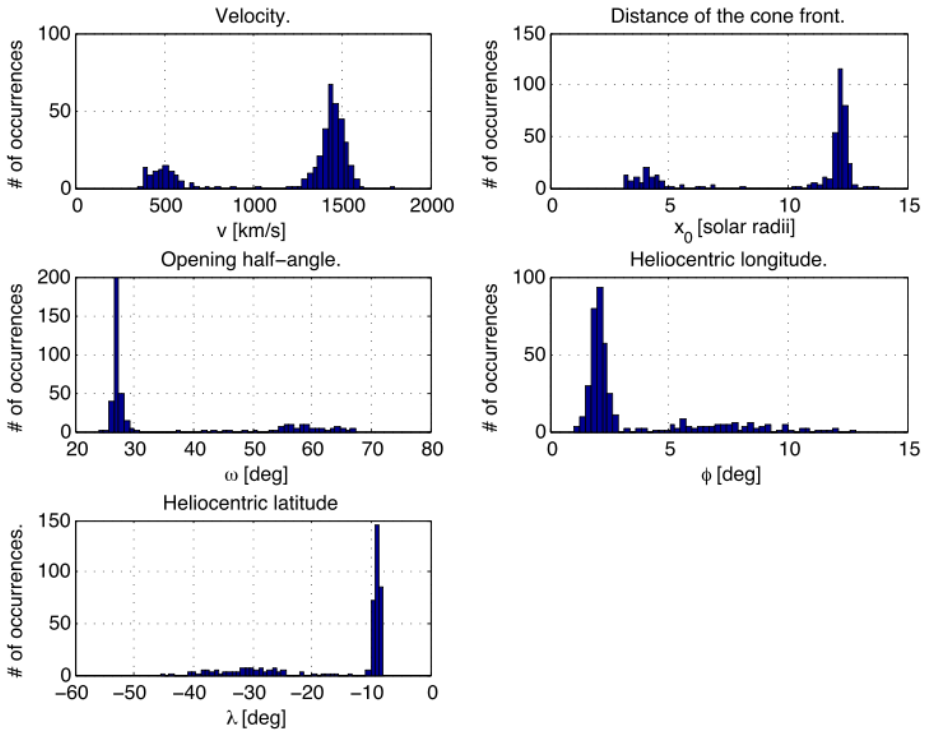

Figure 7. The distribution of the cone parameters obtained using the bootstrap approach for the 13 Dec 2006 CME, adapted from *Pulkkinen et al.* [2010].

The bootstrap approach creates distributions of the cone parameters. The calculated distributions can be used to directly create an ensemble of input parameters for ENLIL, which could be used for ensemble forecasting of the propagation time of a CME to Earth as well as the impact of the CME on the Earth's magnetosphere.

2.2.2 WSA

The Wang-Sheely-Arge (WSA) model is an empirical model used to predict background solar wind speed and interplanetary magnetic field (IMF) polarity based on magnetogram measurements [*Arge and Pizzo*, 2000]. The WSA model has two components: the WSA Potential Field + Current Sheet (WSA PF+CS) model and the WSA Inner Heliosphere (WSA-IH) model. WSA is used to determine the inner boundary conditions for ENLIL, and to determine the ambient solar wind parameters in the heliosphere. It combines a Potential Source Surface model with the Schatten Current Sheet model to predict the magnetic field between the solar surface and a boundary sphere, which is usually set with the source surface radius at 2.5 solar radii [*Arge and Pizzo*, 2000]. The WSA-IH model is then used to propagate the solar wind and magnetic field polarity to 21.5 solar radii, where they are used as the inner boundary conditions for ENLIL.

The magnetic field at the solar surface is derived from magnetogram data measured from Kitt Peak, Mount Wilson, or a Global Oscillation Network Group (GONG) observatory. An example of a magnetogram from the National Solar Observatory (NSO) at Kitt Peak is displayed in Figure 8. The magnetogram provides information on the complex magnetic field structure on the solar surface before and during a CME eruption. The daily magnetogram measurements are used to create full rotation synoptic maps, which are used to determine the magnetic field configuration of the photosphere. The synoptic maps are updated daily.

The Potential Source Surface Model calculates the coronal magnetic field structure at the source surface (2.5 solar radii) in terms of a series expansion of spherical harmonics, with the assumption that the magnetic field is completely radial at this surface. The WSA model truncates the series above $l = 30$ [*Arge and Pizzo*, 2000]. Magnetograms are used to measure the line-of-sight (LOS) component of the photo-

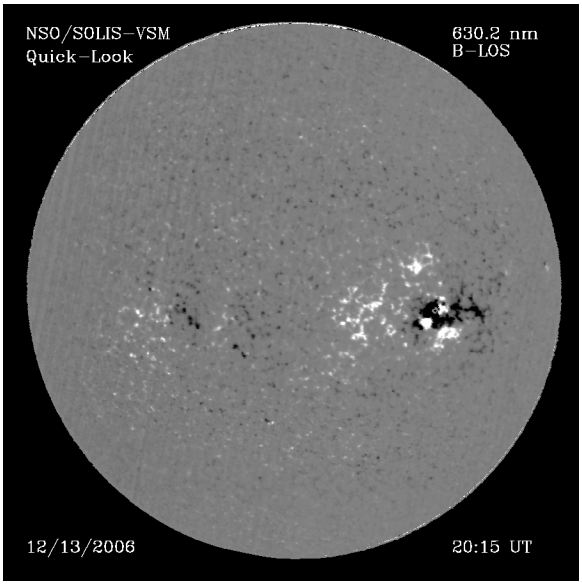

Figure 8. The Kitt Peak magnetogram of the solar photosphere, measured on 13 Dec 2006. The WSA model uses magnetograms, such as this, to estimate the solar wind speed and IMF polarity.

spheric magnetic field. The LOS component of the photospheric magnetic field may be described by

$$B_l = B_r \sin(\theta)\cos(\phi - \phi_0) + B_\theta \cos(\theta)\cos(\phi - \phi_0) - B_\phi \sin(\phi - \phi_0), \tag{13}$$

where B_l is the LOS component of the magnetic field, ϕ_0 is the Carrington longitude of the Sun's central meridian at the time of observation, and θ is the colatitude [*Arge and Pizzo*, 2000]. At the source surface, with the assumption of a completely radial magnetic field, Equation 13 may be reduced to

$$B_l = B_r sin(\theta) cos(\phi - \phi_0). \tag{14}$$

The radial component of the magnetic field, at the source surface, may be solved for in terms of B_l. The measurements obtained by the magnetograms must be corrected for longitudinal and latitudinal projection effects in order to obtain an accurate

estimation of the radial magnetic field at the source surface.

The solar wind speed at the source surface can be calculated using an empirical relationship relating the solar wind speed to the distance to the nearest coronal hole and the divergence of the magnetic field. The empirical relationship may be described by

$$v(f_s) = 267.5 + \left[\frac{410}{f_s^{2/5}}\right] \; [km/s]. \tag{15}$$

f_s refers to the magnetic expansion factor [*Arge and Pizzo*, 2000]. The magnetic expansion factor may be described by

$$f_s = \left(\frac{R_{sun}}{R_{ss}}\right)^2 \left[\frac{B^P(R_{sun})}{B^P(R_{ss})}\right], \tag{16}$$

where R_{ss} refers to the radius of the source surface, $B^P(R_{ss})$ is the computed local magnetic field strength at point P on the source surface, and $B^P(R_{sun})$ is the measured (from magnetograms) magnetic field strength at the photosphere for the point corresponding to P by backtracking along the field line connecting P to the photospheric surface [*Arge and Pizzo*, 2000].

After the solar wind parameters are determined at the source surface, the solar wind can be propagated into the heliosphere. The solar wind is known to flow radially outward from the Sun, in the inertial reference frame. To propagate the solar wind, WSA first produces a synoptic map of the solar wind speed at the source surface. The synoptic map is converted to a grid, where each cell can propagate radially while interacting with the adjoining cells. The cells are allowed to propagate 1/8 AU, at their initial velocity, before they interact with the other cells. At that point, the

velocities are recalculated following the weighting function

$$v_i = \sqrt{\frac{2}{(1/v_i^2) + (1/v_{i+1}^2)}}, \tag{17}$$

where v_i is the velocity of the cell of interest, and v_{i+1} is the velocity of the adjacent cell [*Arge and Pizzo*, 2000]. This process is repeated every 1/8 *AU* until 1 *AU* is reached. The IMF polarity is propagated using a similar procedure, except that an average of overlapping cells is used instead of a weighting function.

The solar wind parameters can be propagated to an outer boundary besides Earth, if required. To use WSA with ENLIL, the magnetic field configuration and solar wind speeds are propagated to 21.5 solar radii, where they are used as the inner boundary conditions. Due to the fact that the synoptic maps are updated pseudo-daily, the boundary conditions are time dependent and account for changes in the ambient solar wind parameters due to changes in the magnetic field of the photosphere and corona.

2.2.3 ENLIL

After the input parameters are obtained from the Coned Model and the boundary conditions are obtained from the WSA model, ENLIL approximates the time dependent solution to the MHD equations governing the plasma from 21.5 solar radii to an appropriate outer boundary (1.1 AU for analyzing the effects of a CME near Earth). ENLIL utilizes a modified Total-Variational-Diminishing Lax-Friedrich (TVDLF) finite difference scheme to approximate the solution to the partial differential MHD equations [*Tóth and Odstrcil*, 1996].

ENLIL is able to solve the equations in one, two, or three dimensions using spherical or Cartesian coordinates [*Odstrcil*, 2003]. ENLIL obtains an approximation for each of the MHD variables at every grid point for every time step. The MHD equa-

tions solved by ENLIL are displayed in Equations 4 and **??**.

The Total-Variational-Diminishing (TVD) algorithms require that the total amount of variation does not increase with time:

$$\sum_j |\Delta U^{n+1}_{j+1/2}| \leq \sum_j |\Delta U^{n}_{j+1/2}|, \tag{18}$$

where $U^{n+1}_{j+1/2}$ is the value of the variable of interest at time-step $n+1$ and spatial position $j+1/2$, and $U^{n}_{j+1/2}$ is the value of the variable of interest at time-step n at the same spatial position $j+1/2$ [*Tóth and Odstrcil*, 1996]. The common convention for describing finite difference schemes places the time-step as the superscript and the spatial-step (position) as the subscript.

A full step for the TVDLF finite difference scheme may be described by

$$\begin{aligned} U^{T}_{j} &= U^{n}_{j} - \frac{\Delta t}{\Delta x}\left(F^{LR}_{j+1/2} - F^{LR}_{j-1/2}\right), \\ U^{n+1}_{j} &= U^{T}_{j} + \frac{1}{2}\left(\Phi^{LR}_{j+1/2} - \Phi^{LR}_{j-1/2}\right), \end{aligned} \tag{19}$$

where U^T describes the value of the variable of interest during the transport stage, U^{n+1} is the value of the variable of interest at the full time step, the L and R superscripts refer to the upwinded left and right states, F^{LR} is the flux at the cell interface, and Φ^{LR} is a dissipative limiter [*Tóth and Odstrcil*, 1996]. The transport stage is the stage where the discrete equations are solved (transported to the next iteration), and the dissipative limiter is used to correct numerical errors from the transport stage. The flux interface follows

$$F^{LR} = [F(U^L) + F(U^R)]/2. \tag{20}$$

For the Lax-Friedrichs scheme, the dissipative limiter follows

$$\Phi_{j+1/2} = \frac{\Delta t}{\Delta x} c^{max}_{j+1/2} \Delta U^{LR}_{j+1/2}, \tag{21}$$

where $\Delta U^{LR}_{j+1/2} = U^{R}_{j+1/2} - U^{L}_{j+1/2}$, and $c^{max}_{j+1/2}$ is the maximum propagation speed of information in the medium of interest [*Tóth and Odstrcil*, 1996]. For the MHD equations, the maximum propagation speed follows

$$c^{max}_{q} = |v_q| + \frac{1}{\sqrt{2}} \left[\frac{\gamma p + \mathbf{B}^2}{\rho} + \sqrt{\left(\frac{\gamma p + \mathbf{B}^2}{\rho} \right)^2 - 4 \frac{\gamma p B^2_q}{\rho^2}} \right]^{1/2}, \tag{22}$$

where v_q is the q^{th} component of the plasma velocity, ρ is the mass density of the plasma, p is the pressure, $\mathbf{B}$ is the magnetic field, and γ is the ratio of the specific heats [*Tóth and Odstrcil*, 1996]. The TVDLF scheme has a truncation error of order $\mathcal{O}(\Delta t^2)$ [*Tóth and Odstrcil*, 1996].

The time-dependent solution to the MHD equations will display the motion of the plasma composing the CME and the effect of the CME on the ambient solar wind and interplanetary magnetic field. The current version of ENLIL assumes no internal magnetic field structure to the CME, but allows the propagation of the CME to distort the interplanetary magnetic field structure.

ENLIL allows the user to select a particular radial distance from the Sun (such as the Earth), and analyze a variety of plasma parameters over time at that particular position. This feature may be utilized to determine the propagation time of a CME to Earth as well as the magnitude of the impact on the Earth's magnetosphere.

2.3 Previous ENLIL Analyses

In 1999, *Odstrčil and Pizzo* used a three dimensional numerical MHD model to analyze the spatial and temporal evolution of solar wind disturbances due to CMEs. This analysis used the TVDLF algorithm to solve the MHD equations in order to analyze the distortion of the structured interplanetary magnetic field due to a propagating CME. The ambient solar wind structure was an idealized representation, and was not based on actual measurements of the solar magnetic field. The solar wind structure was varied to analyze the effects of the solar wind structure on the interaction between the CME and the interplanetary magnetic field. This three dimensional numerical MHD model was the first version of ENLIL.

In 2004, ENLIL was used to analyze the the 12 May 1997 interplanetary CME using an ambient solar wind structure derived from photospheric magnetic field observations [*Odstrcil et al.*, 2004]. The photospheric magnetic field observations were magnetograms measured by the National Solar Observatory at Kitt Peak. The magnetograms were used to find a three dimensional MHD solution to the solar corona based on an empirical model developed by *Riley et al.* [2001]. The MHD solution provided an estimate of the magnetic field and plasma velocity at 30 R_s. The output of the simulation was compared to satellite measurements near Earth, and showed reasonable agreement.

The 12 May 1997 CME was reanalyzed, in 2005, using the Wang-Sheeley-Arge (WSA) model and Mount Wilson Observatory magnetograms to determine the ambient solar wind structure [*Odstrcil et al.*, 2005]. This analysis also used a version of the Cone Model to determine the CMEs angular width, propagation speed and direction from SOHO/LASCO images. Full rotation coronal maps were created by the WSA model, and were used as the inner boundary condition. The coronal maps were updated pseudo daily using a technique developed by *Zhao et al.* [1997]. The simulation

concluded that it was becoming more feasible to simulate large scale structures and ambient solar wind parameters to estimate the propagation times of CMEs to Earth, and that small scale solar wind structures have a large impact on the appearance of the transient disturbances [*Odstrcil et al.*, 2005].

The combination of using the Cone Model to determine the input CME characteristics, using the WSA model to determine the boundary conditions for the ambient solar wind structure, and using ENLIL to solve the MHD equations became the basis of numerical CME modeling.

In 2009, *Taktakishvili et al.* validated the WSA-ENLIL with Cone Model by analyzing the propagation time to Earth and impact on the Earth's magnetosphere for 14 CMEs [*Taktakishvili et al.*, 2009]. The Cone Model parameters were calculated using the technique developed by *Xie et al.* [2004]. The WSA-ENLIL with Cone Model outperformed the empirical shock arrival model of *Gopalswamy et al.* [2005] as well as the 48 *hour* average CME propagation time to Earth for the majority of the 14 CMEs examined in the analysis [*Taktakishvili et al.*, 2009]. The 48 *hour* average propagation time was calculated by analyzing the POS propagation speeds of 320 CMEs, which produced an average velocity of 850 km/s corresponding to a 48 *hour* propagation time to Earth.

The dependence of the WSA-ENLIL with Cone Model predictions on the input CME velocity, density factor, and angular width were analyzed by *Taktakishvili et al.* [2010]. They found that the propagation time and minimum magnetopause standoff distance were highly dependent on the values of the input parameters. This analysis showed that uncertainty in the initial conditions could have a large effect on the model predictions.

In 2011, *Taktakishvili et al.* employed the WSA-ENLIL with Cone Model to analyze CMEs with particularly large geomagnetic storms. This analysis used both the

analytical Cone Model developed by *Xie et al.* [2004] and the automatic Coned Model developed by *Pulkkinen et al.* [2010] to determine the cone parameters. The median values of the cone parameter distributions from the Coned Model were used as the cone parameters for a single WSA-ENLIL run. 36 CMEs were analyzed with associated geomagnetic storms of Kp $\geq$ 8. The results showed a mean absolute propagation time forecast error of 6.9 hours for the analytical method, and a mean absolute propagation time forecast error of 11.2 hours for the automatic method. Both methods overestimated the deformation of the magnetospause. The analysis showed that the WSA-ENLIL with Cone Model combination could predict the arrival time and magnetospheric impact of CMEs with particularly large geomagnetic storms reasonably well.

Recently, both the WSA-ENLIL with analytic Cone Model and WSA-ENLIL with Coned Model version 1.2 were used to analyze the propagation of CMEs to Earth and Mars [*Falkenberg et al.*, 2011]. The analysis concluded that both the velocity and width were underestimated by Coned Model version 1.2. This analysis led to the creation of Coned Model version 1.3, which added a modification to the optimization routine to increase the velocity and width estimations to better match the observations and cone parameters predicted by the analytic Cone Model.

2.4 Ensemble Forecasting

According to *Sivillo et al.* [1997], an ensemble forecast is a collection of two or more forecasts which verify at the same time (each forecast could potentially be the correct forecast). The forecasts start with different initial conditions, within the accepted range of initial values, due to the uncertainty in the measurement of the conditions. The sampling of the ensemble is an application of Monte Carlo statistical methods. By analyzing the results of the ensemble, an average forecast can be calculated using

a weighted average. The average forecast was shown by *Leith* [1974] to produce more accurate forecasts than the conventional single forecast (in terms of the theoretical skill of Monte Carlo forecasts as a function of sample size). Ensemble forecasting has successfully been applied to a variety of weather phenomenon, including the calculation of tropical cyclone trajectories [*Goerss*, 2000].

The success of ensemble forecasting relies on the fact that there is an inherent uncertainty in the measurement of the physical parameters which compose the input parameters of a forecast. *Lorenz* [1963] showed that even if the formulas composing forecasting models are completely correct, there will still be a fundamental limit to the accuracy of a forecast due to the uncertainty in the measurement of the initial conditions. In fact, a small change in the initial conditions can have a quite large effect on the output of the model.

If only one model run is employed for a forecast and the input parameters are slightly off, then the error in the output could be relatively large. Running an ensemble of model runs allows for the uncertainty in initial conditions to be taken into account, and increases the likelihood of running the model with the correct initial conditions. In order for the ensemble to accurately represent the problem, a sample must be selected which accurately represents the distribution of the input parameters. This is key to effective ensemble forecasting.

Ensemble forecasting also allows for a dynamic (changes for each event) quantification of the forecast uncertainty based on uncertainty in the measurement of the initial conditions. This quantification of uncertainty will vary from event to event depending on the amount of uncertainty in the measurements for a specific event. A quantification of the forecast uncertainty would be a very useful addition to operational forecasts of CMEs because it would provide a confidence interval for the forecast, along with a range of possible forecasts.

Formally, ensemble forecasting can be described by a transition from a probability distribution of initial states, $p(\overline{v}_t|\overline{o}_t)$, given a set of observations, $\overline{o}_t$, to a probability distribution of future states, $p(\overline{v}_{t+\tau}|\overline{o}_t)$:

$$p(\overline{v}_{t+\tau}|\overline{o}_t) = \int r(\overline{v}_{t+\tau}|\overline{v}_t)p(\overline{v}_t|\overline{o}_t)d\overline{v}_t, \tag{23}$$

where $\overline{v}_t$ is the initial state, $\overline{v}_{t+\tau}$ is the future state, $r(\overline{v}_{t+\tau}|\overline{v}_t)$ is the transition probability associated with the forecasting model, and the integral is a multiple integral [*DelSole*, 2005]. For a deterministic model (a model which provides the same result if run multiple times with the same set of initial conditions), such as ENLIL, the transition probability can be described by a delta function:

$$p(\overline{v}_{t+\tau}|\overline{o}_t) = \int \delta(\overline{v}_{t+\tau}|\overline{v}_t)p(\overline{v}_t|\overline{o}_t)d\overline{v}_t. \tag{24}$$

For a stochastic model (a model with an inherent degree of randomness), the transition probability will not be a delta function and will depend on the characteristics of the model.

The distribution probability of future states forms the ensemble forecast distribution for a particular set of observations. The ensemble forecast distribution provides a great deal more information than a traditional single forecast. The ensemble forecast distribution can be statistically analyzed to obtain the mean or median value of a particular parameter of interest, along with the associated uncertainty of the value. The range of the ensemble forecast distribution provides the range of possible outcomes for a given set of observations.

III. Methodology

This Chapter discusses the methodology used for the ensemble forecasting of CMEs using the WSA-ENLIL with Coned Model. The core analysis is described as well as the additional analyses completed to analyze performance of the older version of the Coned Model and to test the robustness of the ensemble forecasting technique. The use of the various models are discussed, as well as the analysis of the model results. The procedure used for determining the actual propagation times and maximum K_p indices is also discussed. A more detailed procedure for running the models required for the ensemble forecast is described in Appendix A.

3.1 Core Analysis

For the core analysis, an ensemble forecast was calculated for 15 CMEs using the WSA-ENLIL version 2.7 with Coned Model version 1.3. For each CME, the Coned Model was used to sample 100 sets of initial conditions from the probability distribution of initial states based on a set of observations derived from LASCO C3 images of the CME eruption. The 100 sets of initial conditions were then used as input WSA-ENLIL to obtain the probability distributions of future states, which were used as the ensemble forecast distributions.

Two parameters were analyzed from the ensemble forecast distribution: the propagation time of the CME to the L_1 Lagrangian point, and the maximum K_p index due to the CME impact on the Earth's magnetosphere. For this analysis, the resolution of the computational grid used by ENLIL placed the L_1 Lagrangian point and Earth in the same sector, so the computed propagation time to Earth was the same as the computed propagation time to the L_1 Lagrangian point.

The ensemble forecasting process could be summarized by

$$LASCO\ C3\ Images \rightarrow \overline{o}_t \rightarrow Coned\ Model \rightarrow \tag{25}$$
$$p(\overline{v}_t|\overline{o}_t) \rightarrow WSA-ENLIL \rightarrow p(\overline{v}_{t+\tau}|\overline{o}_t),$$

where $\overline{o}_t$ describes the set of observations, $p(\overline{v}_t|\overline{o}_t)$ describes the probability distribution of initial states, and $p(\overline{v}_{t+\tau}|\overline{o}_t)$ describes the probability distribution of future states (see Section 2.4 for details). A diagram of the transition of an initial state to a future state, with the mapping performed by WSA-ENLIL, is displayed in Figure 9.

Eight of the CMEs were selected from the *Taktakishvili et al.* [2011] analysis, based on CMEs which caused particularly large geomagnetic storms. Using CMEs previously studied allowed for a comparison between studies. The other seven CMEs were selected based on having a maximum K_p of less than eight, and having no other halo-CMEs within plus or minus two days from the eruption day of the CME. The selected CMEs were required to have clear LASCO C3 images to run the Coned Model, and clear ACE data to determine the actual arrival time of the CME at the L_1 Lagrangian point. The CMEs were also selected to produce a large variety of eruption locations (associated solar flare locations) in order to analyze the performance of the model with CMEs initiated from different portions of the Sun. Only 15 CMEs were analyzed due to the 3-day computation time required for each ensemble forecast and the time-limit imposed on this analysis.

Coned Model version 1.3 was used to produce 100 sets of input parameters, for each CME, using the bootstrap approach. Each set of input parameters contained a value for the CME velocity, the cone angular width, and the latitude and longitude of the axis of propagation. A sample size of 100 was used for the initial conditions since the distribution of initial states, derived from the Coned Model, started to stabilize with sample sizes around 100 [*Pulkkinen*, 2011].

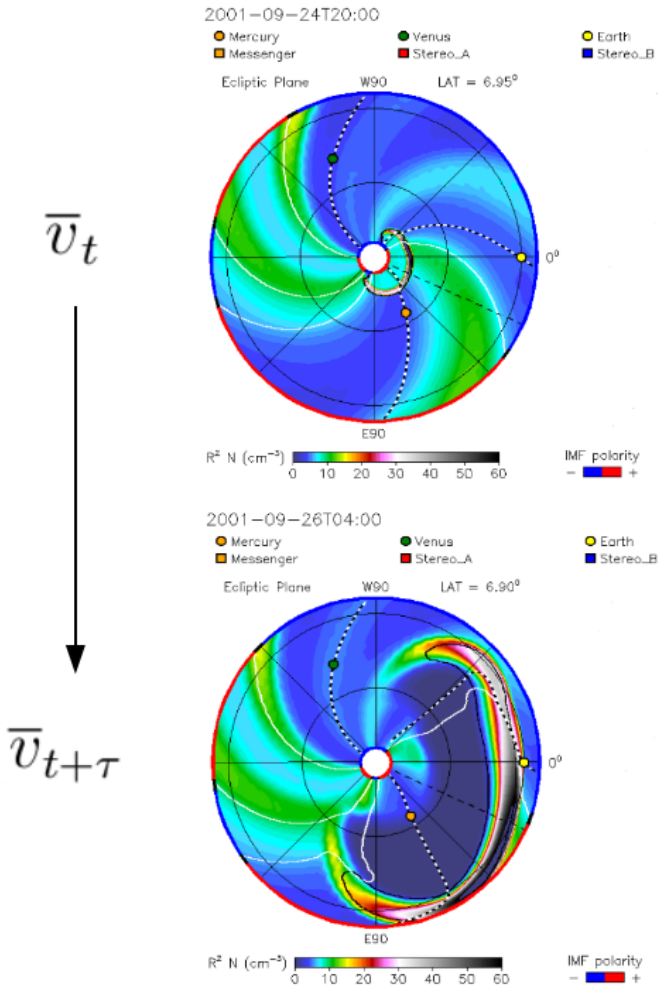

Figure 9. A diagram illustrating how WSA-ENLIL maps a CME with a particular initial state, $\overline{v}_t$, to a future state, $\overline{v}_{t+\tau}$, when the CME is at Earth. The future state can be analyzed to determine the propagation time to Earth, and the associated maximum K_p index.

The bootstrap approach randomly selected 300 points inside of the location of the CME mass in LASCO C3 images, and calculated the parameters based on those 300 points. This process was repeated to obtain the 100 sets of input parameters. All sets of input parameters were optimized solutions to Equations 10 to 19, and therefore accurate samples of the probability distribution of initial states.

The 100 sets of input parameters were then input to WSA-ENLIL to calculate the future states of the CMEs, at Earth. The other WSA-ENLIL parameters were held

constant while the ensemble forecasts were calculated, so that the only variation of the parameters for the ensemble was due to the variation derived from the Coned Model. Each set of input parameters, when input to WSA-ENLIL, provided a propagation time to Earth as well as a worst-case maximum K_p index.

The calculated propagation times were compared to the actual propagation times derived from ACE measurements. The ACE data, with a cadence of 4 *minutes*, was downloaded from NASA's OMNIweb database at `http://ftpbrowser.gsfc.nasa.gov/ace_merge.html`. The actual arrival times derived from ACE data were determined by a sharp increase in the magnetic field magnitude, solar wind speed, and solar wind particle density in the solar wind measurements. An example of the CME arrival time derived from ACE is displayed in Figure 10.

The arrival times were attempted to be determined with 10 minute precision from the ACE data. A few of the CMEs arrived at ACE during a solar proton event, which rendered some of the solar wind sensors unreliable. In these cases, the arrival time had to be determined from the remaining reliable ACE solar wind sensors. All of the actual arrival times calculated directly from ACE data were compared to the arrival times logged in the National Oceanic and Atmospheric Administration (NOAA) Space Weather Prediction Center's (SWPC) historical weekly reports (`http://www.swpc.noaa.gov/ftpmenu/warehouse.html`) to ensure consistency.

The calculated maximum K_p indices were compared to the actual ground-based maximum K_p values using integer resolution. The actual maximum K_p indices were found using NASA's OMNIWeb database (`http://omniweb.gsfc.nasa.gov/form/dx1.html`), and analyzing the actual K_p index in the hours following the CME arrival at Earth. The measured values for the propagation time, maximum K_p indices, and locations of the associated solar flares are displayed in Table 2. The associated solar flare locations were derived from the NOAA/SWPC historical solar events reports,

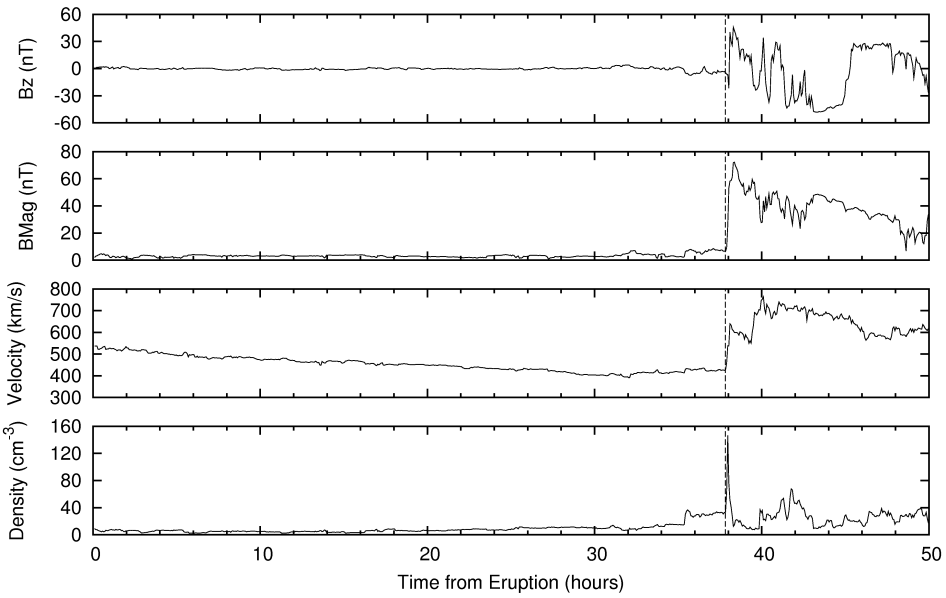

Figure 10. The arrival time of the 29 Mar 2001 CME, as derived from the solar wind data collected by ACE. The dashed vertical line represents the arrival time of the CME, and is characterized by a sudden increase in magnetic field magnitude, solar wind speed, and solar wind particle density. In this figure, Bz represents the z component of the magnetic field, and $BMag$ represents the magnitude of the magnetic field.

and were used to approximate the locations of the CME eruptions.

The ensembles were run on a dual core 2.93 GHz Intel machine, which required about 36 $hours$ to complete one ensemble. While 36 hours is too long for an operational forecast, if the ensemble was split and run in parallel on 10 similar machines (as it will be done at NASA/GSFC), the runs would be completed within 4 $hours$. A 4-$hour$ computation time provides enough lead-time for a useful operational forecast.

Table 2. The start date and times, actual propagation times as measured by ACE, maximum K_p indices as measured by ground based magnetometers, and the locations of the associated solar flares for the 15 CMEs analyzed. The CMEs are also labeled with an event number for easy reference.

event number	CME start date (YYYYMMDD)	CME start time (UT)	propagation time to ACE (HH:MM)	maximum K_p	associated solar flare location
1	19990503	06:06	56:50	3	N15E32
2	20000404	16:32	47:30	9	N16W66
3	20000714	10:54	27:20	9	N22W07
4	20010329	10:26	37:50	9	N20W19
5	20010410	5:30	33:50	8	S23W09
6	20010924	10:30	33:30	7	S16E23
7	20011009	11:30	52:45	6	S28E08
8	20011104	16:35	32:40	9	N06W18
9	20011117	05:30	60:00	4	S13E42
10	20031028	11:30	18:20	9	S16E08
11	20031029	20:54	19:50	9	S15W02
12	20040720	13:31	44:20	7	N10E35
13	20041106	02:06	39:40	9	N07E00
14	20041203	00:26	54:20	4	N09E03
15	20100403	10:34	45:15	8	S25E00

3.2 Model Input

The Coned Model required a series of LASCO C3 images of the CME eruption to calculate the ensemble of input parameters. This analysis used three images for each CME, with a temporal spread of at least one hour between the three images. The Coned Model also contains a threshold level for filtering the images to determine the location of the CME mass by analyzing the brightness of each pixel of the LASCO images. The brightest portions of the images correspond to the location of the CME plasma, which scatter a large amount of visible electromagnetic radiation.

In the Coned Model, the selected location of the CME mass depends on the threshold level value used to filter the images. The threshold level is the percentage of the normalized intensity used to select the CME mass from the images. The threshold level ranges from zero to one, with zero selecting everything in the images

and one selecting nothing. The default threshold level was set to 0.56, which was found to be the optimal level for most CMEs [*Pulkkinen*, 2011]. The threshold was altered for images where large outliers were produced using the default threshold level. A list of the time stamps of the LASCO C3 images used for Coned Model input as well as the threshold level used for filtering the images is available in Appendix A.

Table 3. A list of the input parameters for the WSA-ENLIL with Coned Model along with their default values.

Input Parameter	**Value**
Magnetogram Source	NSO-Kitt Peak
Number of Cone Clouds	1
Outer Radial Boundary	1.1 AU
Fast Stream Solar Wind Density	200 cm^{-3}
Fast Stream Solar Wind Temperature	0.8×10^6 K
Fast Stream Solar Wind Speed	625 km/s
Fast Stream Radial Magnetic Field	300 nT
Minimum Solar Wind Speed	225 km/s
Magnetic Field Scaling Factor	2.5 (for NSO-Kitt Peak)
Fraction of Alpha Particles to Protons	0.03
Cloud Start Date	Variable
Cloud Start Time	Variable
Latitude of Cloud Center	Variable
Longitude of Cloud Center	Variable
Radius of Cloud	Variable
Cloud Velocity	Variable
Density Enhancement Factor	4
Temperature Enhancement Factor	1
Elongation Factor	1
Shape of Cloud	Spherical
Resolution	160x30x90

While the CME velocity, angular width, and axis of propagation were varied, the other input parameters to WSA-ENLIL were held constant for the core analysis (Table 3). Magnetogram measurements were available from multiple source locations, but the core analysis used magnetograms measured by the Kitt Peak National Observatory for

all of the CMEs. The low resolution (160x30x90) option for the ENLIL computational grid was used for all CMEs due to the large computation time required for high resolution model runs.

3.3 Analysis of Model Output

The output from the WSA-ENLIL with Coned Model was analyzed to determine the propagation time to Earth and the maximum K_p index. The arrival time of the CME at Earth was selected to be the time at which the solar wind dynamic pressure had a sharp increase in magnitude. The solar wind dynamic pressure was described by

$$P_{dynamic} = \rho_m v^2 \approx n m_p v^2, \tag{26}$$

where ρ_m is the mass density, v is the plasma flow velocity, n is the particle density, and m_p is the mass of the proton. The sharp increase in magnitude was found numerically from the data by calculating the derivative of the solar wind dynamic pressure with respect to time. The rapid increase in the solar wind dynamic pressure was associated with a relatively large temporal derivative, which was used to indicate the arrival of the CME. The arrival time could also be considered to be the time at which the second derivative of the dynamic pressure with respect to time was a maximum. To ensure that the arrival times calculated by the first derivative were not falsely triggered, the arrival times calculated by the first derivative were compared to the arrival times calculated by the maximum second derivative, and they were found to be in good agreement. An example of the calculated arrival time is displayed in Figure 11.

The maximum K_p indices were found using the *Newell et al.* [2007] maximum K_p

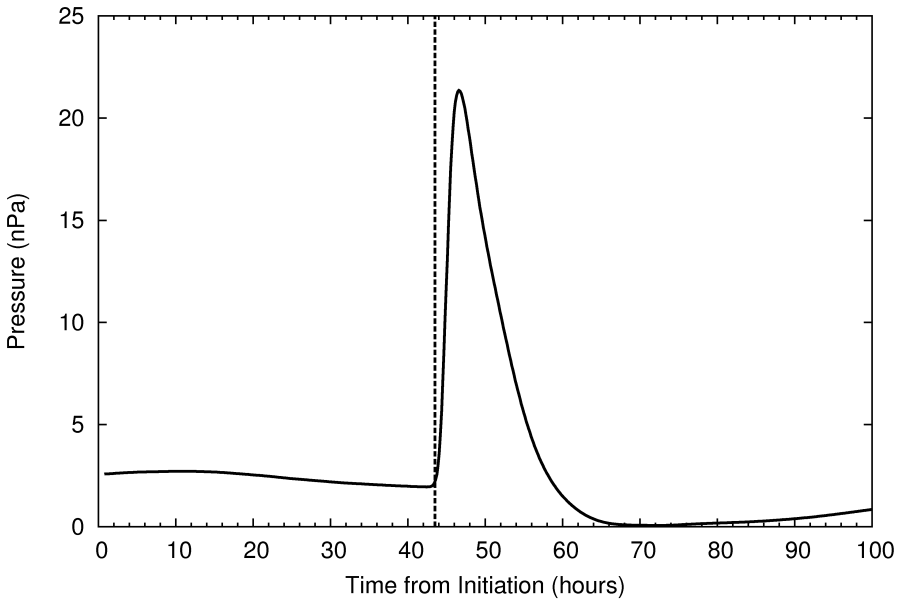

Figure 11. An example plot of the calculated arrival time for the 13 Dec 2006 CME at Earth using the WSA-ENLIL with Coned Model output. The dashed vertical line represents the arrival of the CME determined by the first derivative of the dynamic pressure.

formula (Equation 6) with the assumption that the magnetic field was completely southward ($\theta_c = \pi$), in order to calculate the worst-case scenario. The constant, one, was removed from the empirical formula due to previous analyses using the completely southward magnetic field assumption which found that the K_p index predictions were overestimated with the constant held in the formula [*Taktakishvili*, 2011]. The K_p index values computed using Equation 6 were rounded to the nearest integer. Also, the K_p index has a maximum value of nine, so any values calculated using the *Newell et al.* [2007] formula exceeding nine were limited to nine. An example of the calculated K_p index over time, from the WSA-ENLIL with Coned Model output, is displayed in Figure 12.

To analyze the ensemble distributions, a number of statistical measures were calculated for the propagation times, maximum K_p indices, and input parameters. The descriptive statistics calculated were the average, standard deviation, median, me-

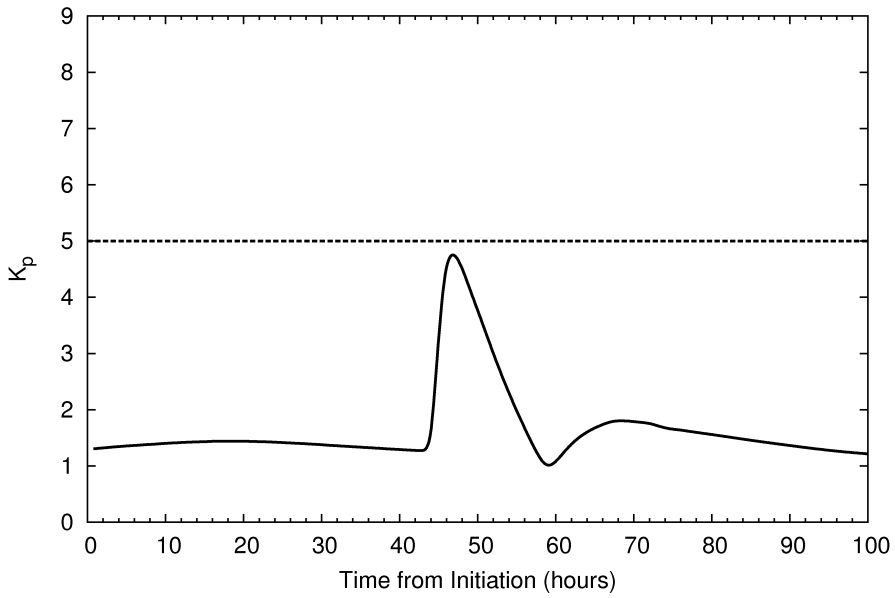

Figure 12. An example plot of the calculated K_p index for the 13 Dec 2006 CME using the WSA-ENLIL with Coned Model output. The dashed horizontal line represents the rounded maximum K_p value.

dian absolute deviation, range, minimum value, and maximum value. The forecast error was also calculated for the propagation time and the maximum K_p. The forecast error was obtained by comparing the average and median values of the ensemble forecast distributions to the actual values. The mean absolute error (MAE) was also calculated for the propagation time and the maximum K_p.

Three metrics were developed to quickly analyze the accuracy of the ensemble forecast. The first metric examined whether the actual propagation time or maximum K_p lay within the average of the ensemble forecast distribution plus or minus one standard deviation of the ensemble forecast distribution. The second metric examined whether the actual propagation time or maximum K_p lay within the median of the ensemble forecast distribution plus or minus one median absolute deviation of the ensemble forecast distribution. Both the average and median of the ensemble forecast distributions were used due to the fact that the ensemble forecast distributions were

not normal, so the average and median values were not equal. The third metric examined whether the actual propagation time or maximum K_p lay within the range of the ensemble forecast distribution.

The ensemble forecast was considered to be an accurate forecast if all three metrics were satisfied. If the actual values were outside of the average plus or minus one standard deviation and median plus or minus one median absolute deviation, but were within the range, then the forecast was not completely inaccurate. If the forecast did not satisfy any of the three metrics, then the forecast was considered to be inaccurate.

3.3.1 Relative Performance and Skill Score

The relative performance and skill score of a model analyze the performance of the model compared to a reference model. The relative performance of the WSA-ENLIL with Coned Model compared to a reference model, with respect to propagation time, can be described by

$$R = 1 - \frac{|\Delta t_{error}^{ENLIL}|}{|\Delta t_{error}^{reference}|}, \tag{27}$$

where R is the relative performance, Δt_{error}^{ENLIL} is the forecast error of the propagation time predicted by the WSA-ENLIL with Coned Model ensemble forecast, and $\Delta t_{error}^{reference}$ is the forecast error of the propagation time predicted by the reference model [*Taktakishvili et al.*, 2009]. A R value greater than zero indicates that the WSA-ENLIL with Coned Model outperformed the reference model, while a R value of less than zero indicates that the reference model outperformed the WSA-ENLIL with Coned Model. A R value of one indicates a perfect prediction by the WSA-ENLIL with Coned Model, while a R value of zero indicates the same error in both the WSA-ENLIL with Coned Model forecast and the reference model forecast.

The skill score is similar to the relative performance, except that it analyzes the

overall performance of a model compared to a reference model. The skill score can be described by

$$Skill\ Score = 1 - \frac{\left\langle |\Delta t_{error}^{ENLIL}| \right\rangle}{\left\langle |\Delta t_{error}^{reference}| \right\rangle}, \tag{28}$$

where $\langle ... \rangle$ indicates the mean value for all of the events analyzed [*Taktakishvili et al.*, 2009]. The skill score values follow the same guidelines as the relative performance values. A positive skill score indicates that overall, the WSA-ENLIL with Coned Model outperformed the reference model.

In this analysis, the propagation time predicted by the WSA-ENLIL with Coned Model was compared to six reference models. The forecast error of the ensemble forecast average was used as the error of the propagation time for the WSA-ENLIL with Coned Model. The six reference models were the Shock Time of Arrival (STOA) model, the Interplanetary Shock Propagation Model (ISPM), the propagation time based on the kinematic POS first-order speed estimation of the CME based on LASCO imagery, the propagation time based on the Coned Model average velocity, the propagation time based on the measured type II speed, and a "single-shot" best estimate using WSA-ENLIL. The maximum K_p was only compared to the single-shot best estimate due to the fact that this was the only other model which could be used to calculate the maximum K_p index.

STOA is a shock propagation model used to predict the shock arrival time, due to a CME, at Earth. STOA uses similarity theory to calculate the shock speed profile as a function of radial distance from the Sun (*Dryer* [1974], *Hilmer* [2001]). The input parameters required to run STOA are the event duration estimated from GOES X-ray levels, the event onset time, the peak-class of the X-ray event, the type II drift speed, the associated flare location, and the observer location. STOA was selected

as a reference model due to the fact that it is used by the Air Force Weather Agency (AFWA) to predict the arrival times of CMEs.

ISPM is another shock propagation model used to calculate the arrival time and strength of a shock due to a CME at Earth. The arrival time and strength of the shock are calculated from algebraic equations derived from a parametric study of interplanetary shocks based on MHD simulations (*Smith and Dryer* [1990], *Hilmer* [2001]). The input parameters required to run ISPM are the flare location, the event start time, the event duration, and the initial shock speed based on type II drift speeds. ISPM is also used by AFWA to predict the arrival time of CMEs.

The kinematic POS first-order speed estimation of the CME based on LASCO imagery is an estimation of the two-dimensional speed of a CME calculated by fitting the position versus time data of the leading edge of a CME to a linear velocity curve. This provides a rough estimate of the initial CME speed, and could be used to estimate the propagation time of the CME to Earth. The propagation time of a CME to Earth, assuming no accelerations of the CME, was calculated by dividing the distance to the Earth (which depended on the date of the CME) by the first-order speed. The kinematic POS first-order speed estimations based on LASCO imagery were found in NASA's CDAW catalog (`http://cdaw.gsfc.nasa.gov/CME_list/`).

The average of the ensemble velocity distribution, calculated by the Coned Model, could also be used as a rough estimation of the CME speed. This speed was used to calculate the propagation time to Earth by following the same procedure used to calculate the propagation time using the kinematic POS first-order speed estimations based on LASCO imagery. The average Coned Model velocity was calculated by taking the average of the 100 sets of input velocities for a particular CME.

The type II speed is the measurement of the movement of a large, dense plasma cloud in the solar corona. Type II meter wave bursts are the emissions of two distinct

frequency bands which are due to the fundamental and second harmonic of plasma oscillations from the shock formed by the plasma cloud moving through the corona [*Foukal*, 2004]. The shock formed by the moving plasma cloud produces radiation at frequencies starting around 300 MHz, and drifting to around 3 MHz. The frequency emitted is a function of height, so the drift in frequencies can be used to calculate the speed of the plasma cloud. The velocity of the shock wave could be used to estimate the radial velocity of a CME, and could be used to calculate the propagation time to Earth by assuming a constant velocity during the propagation. The type II speeds for the CMEs used in this analysis were obtained from the NOAA/SWPC event reports (`http://www.swpc.noaa.gov/ftpmenu/warehouse.html`).

The current technique used by NASA's Community Coordinated Modeling Center (CCMC) at Goddard Space Flight Center to predict the propagation time and impact of a CME is to estimate a single set of CME cone parameters using a triangulation technique based on STEREO and LASCO data, and then run the single set of parameters through WSA-ENLIL to calculate the propagation time and impact of the CME. If STEREO data is not available, then CCMC uses the Coned Model to determine a single set of cone parameters by calculating the median values of the parameters based on 100 possible sets of input parameters. The median values are then used to run a single-shot best estimate of the CME propagation time and impact. In order to compare the performance of the ensemble forecast against the currently employed technique at CCMC, the ensemble forecast was compared to the single-shot best estimate of the CMEs calculated using the median values of the cone parameters obtained from the Coned Model distributions. Only one of the CMEs in this analysis had STEREO data available (STEREO was launched in 2006), so the Coned Model was used for all of the CMEs to determine the single set of input parameters.

The skill score of the averages of the propagation time ensemble distributions ver-

sus the medians of the propagation time ensemble distributions was also calculated. This skill score was calculated to determine the most accurate statistic to use when describing the propagation time ensemble distributions. For the maximum K_p ensemble distributions, the rounded averages were the same as the medians, so a comparison of the averages and medians would provide no information.

3.4 Coned Model Version 1.2

Coned Model Version 1.3 introduced a modification to the optimization routine to increase the velocity and width estimates based on the results of an analysis of CME propagation times to Earth and Mars using the WSA-ENLIL with Coned Model Version 1.2 combination completed by *Falkenberg et al.* [2011]. The analysis found that the Coned Model Version 1.2 underestimated the velocity and width of the CMEs. To correct this underestimation, Coned Model Version 1.3 modified the optimization routine such that increased velocities and widths were selected.

From the core analysis, it was determined that the ensemble forecasts of the slower CMEs (actual propagation times greater than 46 $hours$), using Coned Model Version 1.3, predicted the arrival times of the CMEs much earlier than the actual arrival times. The ensemble forecasts were recalculated using Coned Model Version 1.2 to determine if the increase in the velocities and widths were the cause of the large propagation time errors observed in the slower CMEs. For completion, the ensemble forecasts for all 15 CMEs were recalculated using Coned Model Version 1.2.

The forecasts using the different Coned Model versions were compared to each other to determine the most accurate version of the Coned Model, overall. The forecasts were also analyzed to determine which version performs more accurately for a particular type of CME. An attempt was made at determining the most accurate version of the Coned Model to use based on the input parameter distributions of a

particular CME.

3.4.1 Generalized Linear Model

During this analysis, it was noticed that using the Coned Model Version 1.2 provided more accurate forecasts than using the Coned Model Version 1.3 for slower CMEs. In order to determine the best Coned Model version to use for an operational forecast of a particular CME, a generalized linear model (GLM) was employed.

A GLM is a form of linear regression, which allows for fitting to data following a probability other than a normal distribution [*Hill and Lewicki*, 2007]. For a set of data which has a yes/no format, such as the need to use Coned Model version 1.2 for a particular CME, a binomial distribution is the natural choice for the type of distribution. Link functions are used to map the linear function of predictors to the nonlinear probability (p $\in$ [0,1]) of an event occurring. The binomial distribution requires the logit link function to link the linear function of predictors to the binomial distribution (see *Spaulding* [2009] for more detail).

The GLM for a dataset following a binomial distribution, using a logit link function, follows

$$f(p) = \log\left(\frac{p}{1-p}\right) = \beta_0 + \beta_1 x_1 + \beta_2 x_2 + ... + \beta_k x_k \tag{29}$$

where $f(p)$ is the link function, p is the probability of the event of interest occurring, x_n is the n^{th} predictor, and β_n is the fit coefficient corresponding to predictor x_n [*Hill and Lewicki*, 2007]. The predictor coefficients are estimated by using maximum likelihood estimations. There are many methods available to produce maximum likelihood estimations, with the iterative re-weighted least squares method as a commonly employed technique.

The GLM was employed to determine if a particular CME forecast would be more

accurate using Coned Model version 1.2 instead of version 1.3, without using the actual propagation time as a predictor. The predictor set was varied to determine if any particular set of predictors provided created the most accurate GLM. The predictor sets used were: the cone parameters (velocity, angular width, latitude and longitude), non-cone parameters (LASCO first order POS velocity, type II speed, and flare location), and the combination of the cone parameters and non-cone parameters.

The GLM was built from the dataset by creating a binomial distribution of needing to use Coned Model version 1.2 from the 15 CMEs of this analysis. Each CME with a propagation time forecast error less than -10 *hours* was assigned a probability of needing to use Coned Model version 1.2 of one, while the remaining CMEs were assigned a probability of zero. The predictor coefficients were then calculated using MATLAB's glmfit() function with the logistic regression option.

The GLM, with the variety of predictor sets, was applied to the 15 CMEs studied in this analysis and four test CMEs which were not part of the 15 CMEs studied in this analysis. The four test CMEs were selected such that two of the CMEs had actual propagation times greater than 50 *hours* (slow CMEs), and the other two had actual propagation times less than 40 *hours* (fast CMEs).

The GLM relied on the parameters obtained for the 15 events studied in this analysis, which is a small number of data-points to build a statistical model. A study completed by *Peduzzi et al.* [1996] suggested that a logistic regression (used to find the fit coefficients for the GLM in this analysis), with less than 10 events per predictive variable, will have difficulty accurately estimating the regression coefficients. The GLM built using the 15 events was created as a framework for future analyses, where the number of events studied can be large enough to satisfy the 10 events per predictive variable.

3.5 Ensemble Forecasting Robustness

After the core analysis was completed, a number of WSA-ENLIL with Coned Model input parameters previously held constant were varied to test the robustness of the ensemble forecasting technique. The ensemble forecasts were compared to the ensemble forecasts using the default input parameters to examine the difference in the forecast due to changing one of the input parameters. Only one input parameter was changed at a time, to ensure that the parameter of interest was causing the change in the forecast. The input parameters varied were the ensemble size, the magnetogram source location, the images used in the Coned Model, and the magnetic field scaling factor.

To test the effects of varying the ensemble size on the ensemble forecast, the ensemble forecast for the 29 Mar 2001 CME was recalculated using ensemble sizes of 25, 50 and 75. The ensemble forecast statistics for the different ensemble sizes were compared to the ensemble forecast using 100 sets of input parameters.

The magnetograms used as input for the WSA model create the background solar wind and IMF structure for the simulation. The magnetograms will be different for the different source locations used to measure the magnetograms. Therefore, the background solar wind solution will change if different magnetograms are used for input to WSA. To analyze the effects of varying the magnetogram source on the ensemble forecast, a couple of runs were repeated using different magnetogram sources. The ensemble forecast for the 3 Apr 2010 CME was recalculated using GONG magnetograms instead of the default NSO-Kitt Peak magnetograms. The ensemble forecast for the 3 Dec 2004 CME was recalculated using magnetograms from Mt. Wilson instead of NSO-Kitt Peak. The ensemble forecasts obtained by varying the magnetogram source location were compared to the ensemble forecast using the NSO-Kitt Peak magnetograms to analyze the effects of varying the magnetogram source

location.

The distribution of initial states produced by the Coned Model required a set of three images to calculate the distribution. To analyze the effects of altering the three images used as input for the Coned Model on the ensemble forecast, the ensemble forecast for the 29 Mar 2001 CME was recalculated using a different set of images. Due to the fact that there are a limited number of LASCO images available for each CME, the image with the time-stamp 20010329124200 was used in both analyses. But, the other two images were different for the two sets of images. The two ensemble forecasts were compared to calculate the differences caused by varying the images used for Coned Model input.

A magnetic field scaling factor was recently added to ENLIL to scale the radial magnetic field derived from magnetograms to match the solar wind magnetic field measured near Earth. The magnetic field scaling factor depends on the solar cycle as well as the magnetogram source. For the NSO-Kitt Peak magnetograms, the magnetic field scaling factor should be set to 2.5. For GONG magnetograms, the scaling factor should be set to 4.0. To analyze the effects of varying the magnetic field scaling factor, a series of ensemble forecasts were recalculated using the NSO-Kitt Peak magnetograms and switching the magnetic field scaling factor from 2.5 to 4.0.

3.6 Flare Location as Propagation Axis

During this analysis, it was noticed that the Coned Model tended to push the propagation axis towards the Sun-Earth line, while the locations of the associated solar flares were widely spread. To test the effects of the propagation axis on the forecasts, the forecasts for 5 events were recalculated using the associated flare location as the propagation axis. The 5 events analyzed were events 1, 2, 4, 6, and 9,

which contained 3 events with actual propagation times greater than 46 $hours$ (slower CMEs), and 2 events with actual propagation times less than 40 $hours$ (faster CMEs). A single WSA-ENLIL run was completed using the flare location as the propagation axis, and the average velocity and width derived from the Coned Model as the CME velocity and width.

IV. Results

This chapter starts with the results of the core analysis, where the 15 CMEs were analyzed using 100 sets of input parameters derived from the Coned Model version 1.3, WSA with NSO-Kitt Peak magnetograms, and ENLIL with the magnetic field scaling factor set at 2.5. The results using Coned Model version 1.2 are presented, including a comparison of the results using both versions of the Coned Model. The propagation time error is analyzed next, with an attempt to determine the source of the large negative forecast errors from Coned Model version 1.3 including the use of a GLM. Finally, the model robustness is analyzed by calculating the forecast changes due to the variation of input parameters other than the cone parameters.

4.1 Core Analysis Results

4.1.1 Input Parameters

The distribution of initial states for the 15 CMEs, calculated by Coned Model version 1.3, are displayed in Tables 4 to 7. While the ensembles could be described by a number of statistical measures, this analysis focused mainly on the average, standard deviation, and range (Figure 13). The input parameter ensembles and filtered LASCO images from the Coned Model are displayed in Appendix B, for each of the 15 CMEs.

The Coned Model tended to push the propagation axes of the CMEs towards the Sun-Earth line, which may not have been an accurate representation of the actual propagation axes. STEREO data was only available for one of the events (event 15), so it was not possible to compare the predicted propagation axes to the actual propagation axes. The Coned Model predicted an average or median propagation axis with a latitude or longitude further on the limb than $\pm 10^{\circ}$ for only 4 of the 15

Table 4. Statistics for the input velocity distributions of the 15 CMEs derived from Coned Model version 1.3, with the average and standard deviation of the columns at the bottom of the table.

CME date (YYYYMMDD)	average (km/s)	standard deviation (km/s)	median (km/s)	median absolute deviation (km/s)	range (km/s)	min (km/s)	max (km/s)
19990503	1691.04	322.10	1709.00	205.00	1615.00	937.00	2552.00
20000404	1789.09	351.13	1779.00	256.50	1783.00	1109.00	2892.00
20000714	1796.84	298.45	1762.00	180.00	1542.00	1059.00	2601.00
20010329	1444.26	304.88	1417.50	235.50	1408.00	848.00	2256.00
20010410	1755.87	345.31	1736.50	221.00	1596.00	1123.00	2719.00
20010924	2122.44	424.25	2061.50	325.50	1867.00	1432.00	3299.00
20011009	1355.10	281.89	1321.00	182.50	1612.00	540.00	2152.00
20011104	2008.58	415.48	2014.00	313.50	1835.00	1312.00	3147.00
20011117	1551.35	323.20	1510.50	229.50	1634.00	913.00	2547.00
20031028	2257.65	401.33	2236.00	273.00	1727.00	1570.00	3297.00
20031029	2030.53	428.01	1938.00	255.00	2033.00	1285.00	3318.00
20040720	1252.72	258.55	1233.00	125.00	1314.00	830.00	2144.00
20041106	1155.03	233.09	1119.00	139.00	1055.00	771.00	1826.00
20041203	1409.42	286.04	1355.00	135.00	1640.00	863.00	2503.00
20100403	985.76	179.85	975.00	133.00	864.00	669.00	1533.00
average	1640.38	323.57	1611.13	213.93	1568.33	1017.40	2585.73
std	374.09	72.69	370.90	64.71	306.18	289.33	545.41

CMEs (3 May 1999, , 10 Apr 2001, 24 Sep 2001, and 17 Nov 2001 CMEs). While the location of the associated solar flare is not necessarily an indicator of the source or direction of the CME propagation, 13 of the 15 CMEs associated solar flare locations were located elsewhere on the disk than $\pm 10^{\circ}$ for either latitude or longitude.

The correlation coefficient for the Coned Model location versus the solar flare location was calculated to be 0.70 with a p-value of 0.00 (Figure 14). The correlation coefficient (Pearson's) describes the degree of linear dependence between two data sets. A correlation coefficient with a magnitude greater than 0.5 is commonly interpreted as a strong correlation. The p-value describes the probability that the correlation occurred by "chance", and that randomly selected points would have the same relationship. A p-value of less than 0.05 is commonly accepted as the criterion for a statistically significant correlation, with a less than 5% probability that

Table 5. Statistics for the input angular half-width distribution of the 15 CMEs derived from Coned Model version 1.3, with the average and standard deviation of the columns at the bottom of the table.

CME date (YYYYMMDD)	average (deg)	standard deviation (deg)	median (deg)	median absolute deviation (deg)	range (deg)	min (deg)	max (deg)
19990503	53.37	8.27	53.00	6.00	40.00	36.00	76.00
20000404	57.42	9.32	57.00	7.00	46.00	36.00	82.00
20000714	61.18	8.51	61.00	5.50	46.00	42.00	88.00
20010329	53.80	10.33	52.00	6.00	49.00	33.00	82.00
20010410	57.05	9.45	57.50	6.50	45.00	38.00	83.00
20010924	71.04	11.23	71.00	9.50	42.00	48.00	90.00
20011009	52.13	8.64	52.00	6.00	50.00	31.00	81.00
20011104	65.74	10.96	64.50	8.50	45.00	45.00	90.00
20011117	51.92	9.28	52.50	6.50	44.00	33.00	77.00
20031028	71.83	9.40	72.00	7.00	38.00	51.00	89.00
20031029	64.97	10.11	66.00	6.00	45.00	42.00	87.00
20040720	48.35	8.13	48.00	6.00	40.00	32.00	72.00
20041106	47.22	8.12	47.00	5.00	37.00	30.00	67.00
20041203	47.99	8.41	48.00	5.50	48.00	28.00	76.00
20100403	44.84	6.78	45.00	5.00	35.00	27.00	62.00
average	56.59	9.13	56.43	6.40	43.33	36.80	80.13
std	8.64	1.19	8.71	1.23	4.50	7.35	8.49

the correlation occurred by "chance". While the correlation coefficient provides an estimate of the strength of linear dependence between two data sets, it does not completely characterize the relationship between the data sets. Caution must be taken when using the correlation coefficient alone to describe a relationship between data sets, because the correlation coefficient can be skewed by nonlinear relationships and outlier data points.

A statistically significant strong correlation existed between the Coned Model location and the solar flare location. While there was a positive correlation between the locations, the Coned Model locations were all located near the Sun-Earth line while the flare locations were more spread. This indicated that while the Coned Model latitudes and longitudes increased when the solar flare latitude and longitudes increased, the amount of increase for the Coned Model was significantly less. The correlation

Table 6. Statistics for the input latitude distribution of the 15 CMEs derived from Coned Model version 1.3, with the average and standard deviation of the columns at the bottom of the table.

CME date (YYYYMMDD)	average (deg)	standard deviation (deg)	median (deg)	median absolute deviation (deg)	range (deg)	min (deg)	max (deg)
19990503	6.41	2.12	6.00	1.00	14.00	4.00	18.00
20000404	0.96	0.40	1.00	0.00	2.00	0.00	2.00
20000714	2.46	0.72	2.00	1.00	3.00	1.00	4.00
20010329	-0.07	0.26	0.00	0.00	1.00	-1.00	0.00
20010410	-10.27	2.13	-10.00	1.00	11.00	-17.00	-6.00
20010924	-4.68	1.25	-5.00	1.00	5.00	-8.00	-3.00
20011009	-8.71	1.75	-9.00	1.00	10.00	-15.00	-5.00
20011104	-1.46	0.54	-1.00	0.00	2.00	-3.00	-1.00
20011117	6.41	1.39	6.00	1.00	6.00	3.00	9.00
20031028	0.38	0.53	0.00	0.00	2.00	0.00	2.00
20031029	-3.53	0.94	-4.00	1.00	4.00	-6.00	-2.00
20040720	0.04	0.20	0.00	0.00	1.00	0.00	1.00
20041106	2.88	1.06	3.00	1.00	6.00	0.00	6.00
20041203	6.61	1.46	6.00	1.00	8.00	3.00	11.00
20100403	-2.19	0.84	-2.00	0.50	4.00	-5.00	-1.00
average	-0.32	1.04	-0.47	0.63	5.27	-2.93	2.33
std	5.09	0.63	4.97	0.48	3.94	6.30	6.44

coefficient for the Coned Model average latitudes versus the solar flare latitudes was calculated to be 0.63 with a p-value of 0.01 (Figure 15), and the correlation coefficient for the Coned Model average longitudes versus the solar flare longitudes was calculated to be 0.73 with a p-value of 0.00 (Figure 16).

To compare the velocity distributions calculated by the Coned Model against other measurements of the CME velocities, the average of the velocity distributions were compared to the LASCO first-order POS velocities as well as the type II radio sweep velocities of the CMEs (Table 8). Not all of the CMEs had type II radio sweep measurements, so the Coned Model velocity distributions of the these CMEs could not be compared to the type II radio sweep velocities.

The correlation coefficient for the Coned Model average velocities versus the LASCO first-order POS velocities was calculated to be 0.90 with a p-value of 0.00

Table 7. Statistics for the input longitude distribution of the 15 CMEs derived from Coned Model version 1.3, with the average and standard deviation of the columns at the bottom of the table.

CME date (YYYYMMDD)	average (deg)	standard deviation (deg)	median (deg)	median absolute deviation (deg)	range (deg)	min (deg)	max (deg)
19990503	-13.65	4.64	-13.00	2.00	35.00	-43.00	-8.00
20000404	8.43	2.06	8.00	1.00	8.00	5.00	13.00
20000714	3.94	0.97	4.00	1.00	5.00	2.00	7.00
20010329	0.03	0.17	0.00	0.00	1.00	0.00	1.00
20010410	3.28	0.91	3.00	1.00	4.00	2.00	6.00
20010924	-17.16	3.79	-17.00	3.00	14.00	-25.00	-11.00
20011009	3.16	0.72	3.00	0.00	4.00	2.00	6.00
20011104	5.82	1.40	6.00	1.00	6.00	3.00	9.00
20011117	-10.91	2.31	-11.00	2.00	11.00	-17.00	-6.00
20031028	0.18	0.44	0.00	0.00	2.00	0.00	2.00
20031029	2.65	0.67	3.00	1.00	3.00	1.00	4.00
20040720	0.00	0.00	0.00	0.00	0.00	0.00	0.00
20041106	-1.09	0.45	-1.00	0.00	2.00	-2.00	0.00
20041203	-2.40	0.64	-2.00	0.00	3.00	-4.00	-1.00
20100403	1.82	0.72	2.00	0.00	4.00	0.00	4.00
average	-1.06	1.33	-1.00	0.80	6.80	-5.07	1.73
std	7.28	1.34	7.15	0.94	8.65	13.22	6.46

(Figure 17). The average velocities from the Coned Model tended to be faster than the LASCO first-order POS velocities. This makes sense due to the fact that the POS velocity estimate only accounts for the projected POS velocity (projected onto two-dimensions), while the Coned Model velocity is the three-dimensional velocity. The three-dimensional velocity should always be greater than or equal to the projected POS velocity.

Only events 5, 6 and 10 (10 April 2001, 24 Sept 2001, and 28 Oct 2003 CMEs) had Coned Model average velocities less than the LASCO first order POS velocities. The Coned Model median velocity for event 11 (29 Oct 2003 CME) was less than the LASCO first-order POS velocity, but the Coned Model average was not. The average difference between Coned Model average and the LASCO first-order POS velocities was 156 km/s, which indicates that the Coned Model average velocity followed the

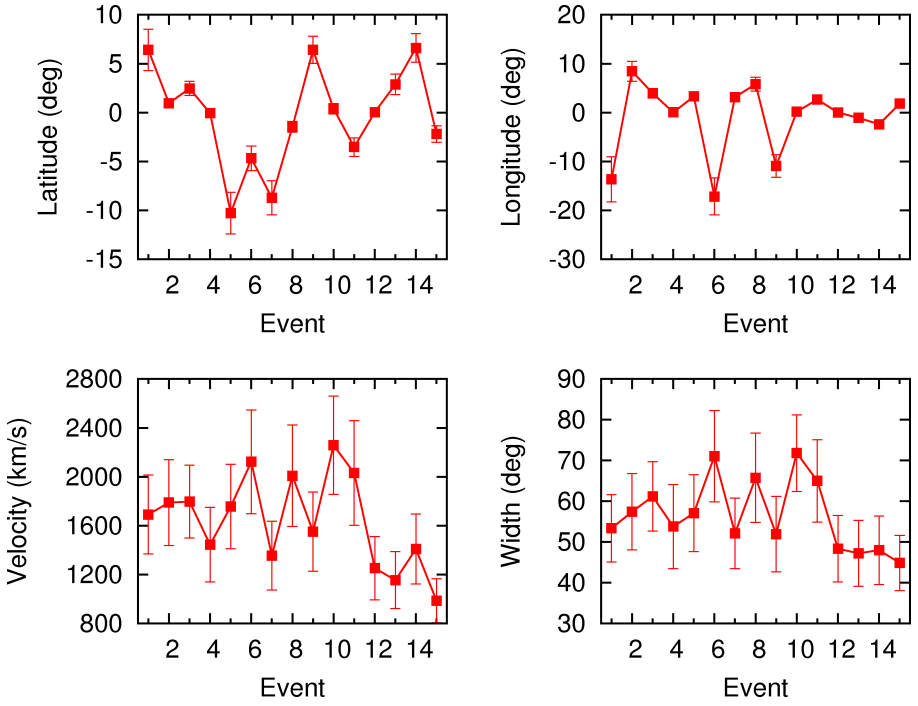

Figure 13. The average and standard deviation of the input parameter distributions, derived from Coned Model version 1.3, for each event.

same general trend as the LASCO first-order POS velocity but was shifted up by around 156 km/s.

All of the Coned Model average velocities except one (event 5) were much greater than the type II speeds. The average difference between the Coned Model average velocities and the type II radio sweep velocities was calculated to be 714 km/s. The correlation coefficient for the Coned Model average velocities versus the type II radio sweep speeds was calculated to be 0.55 with a p-value of 0.08, which indicated that there was not a statistically significant correlation (Figure 18).

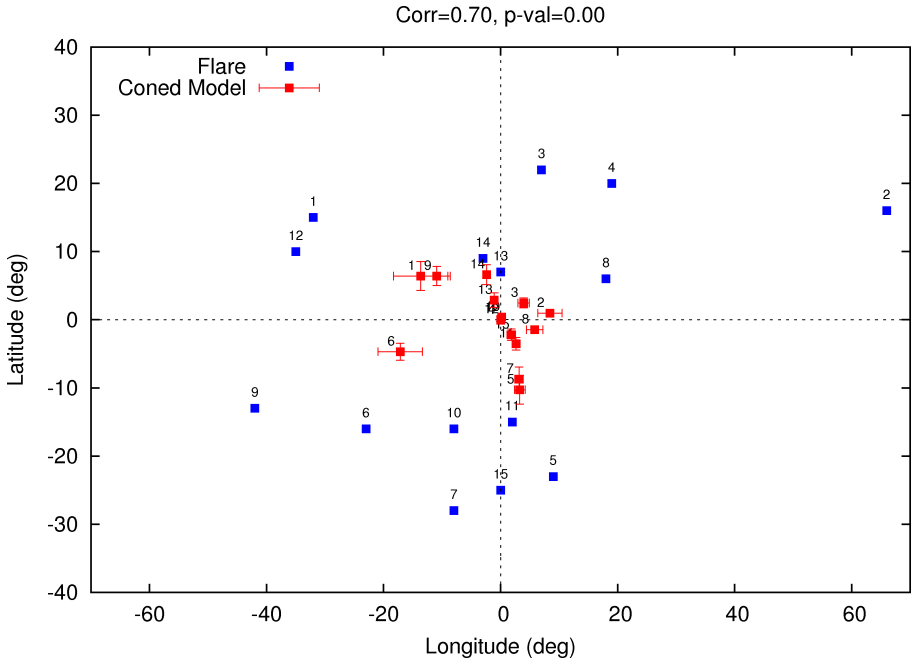

Figure 14. The Coned Model average longitudes and latitudes along with the solar flare latitudes and longitudes, with the event numbers as the labels and the standard deviations of the ensembles as the error bars.

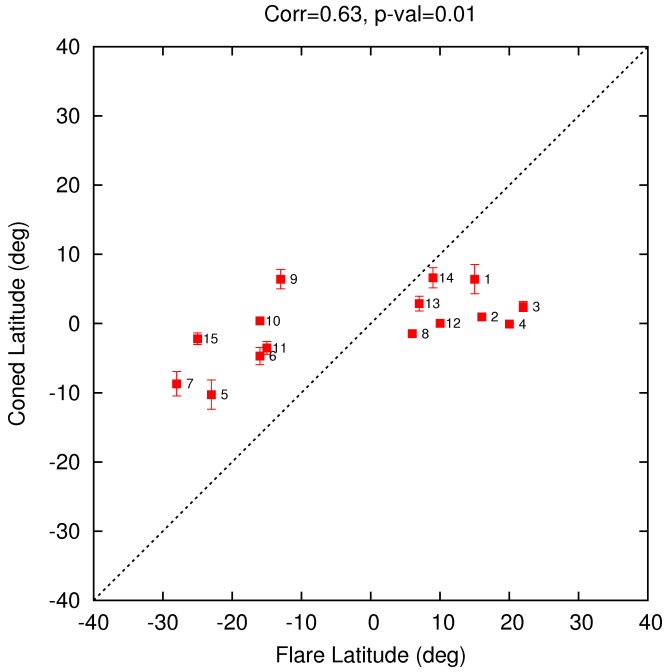

Figure 15. The Coned Model average latitudes versus the solar flare latitudes, with the event numbers as the labels and the standard deviations of the ensembles as the error bars.

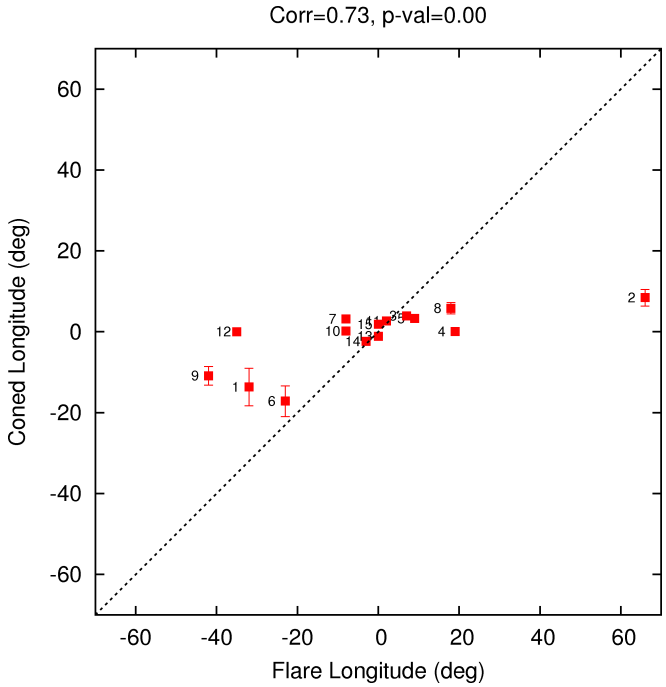

Figure 16. The Coned Model average longitudes versus the solar flare longitudes, with the event numbers as the labels and the standard deviations of the ensembles as the error bars.

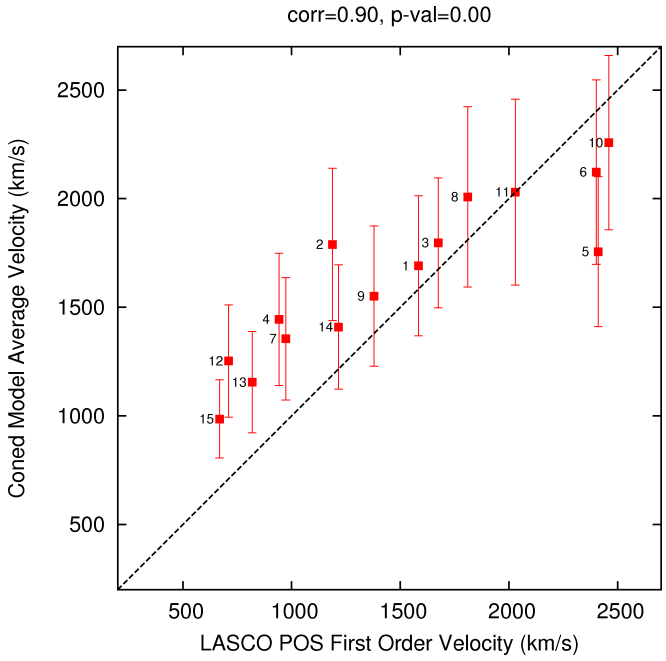

Figure 17. The Coned Model average velocities versus the LASCO first-order POS velocities, with the event number as the label and the standard deviations of the ensembles as the error bars.

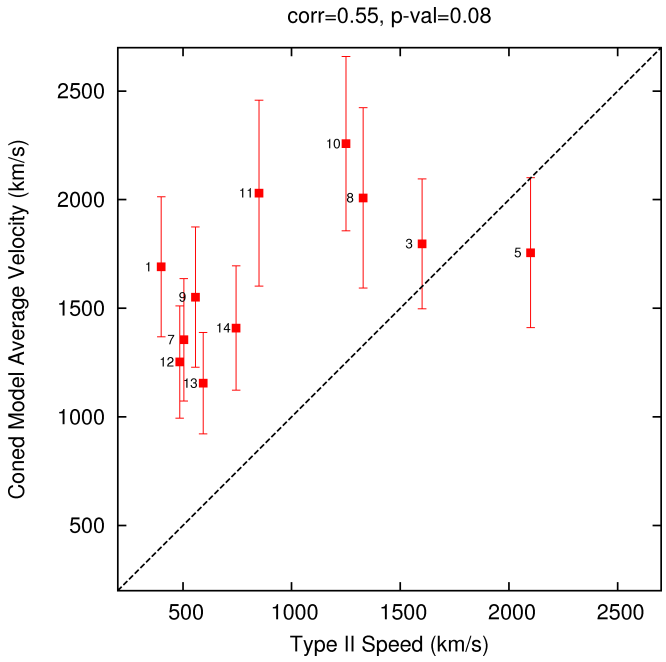

Figure 18. The Coned Model average velocities versus the type II speeds, with the event number as the label and the standard deviations of the ensembles as the error bars.

Table 8. Comparison of the velocity distributions of the output of the Coned Model, the first-order velocity derived from LASCO POS imagery, and the type II speeds of the 15 CMEs.

CME date (YYMMDD)	Coned Model average (km/s)	Coned Model median (km/s)	LASCO POS first order velocity (km/s)	type II radio sweep velocity (km/s)
19990503	1691.04	1709.00	1584.00	400.00
20000404	1789.09	1779.00	1188.00	–
20000714	1796.84	1762.00	1674.00	1600.00
20010329	1444.26	1417.50	941.80	–
20010410	1755.87	1736.50	2411.00	2100.00
20010924	2122.44	2061.5	2402.00	–
20011009	1355.10	1321.00	973.00	504.00
20011104	2008.58	2014.00	1810.00	1329.00
20011117	1551.35	1510.50	1379.00	557.00
20031028	2257.65	2236.00	2459.00	1250.00
20031029	2030.53	1938.00	2029.10	850.00
20040720	1252.72	1233.00	710.00	485.00
20041106	1155.03	1119.00	818.30	593.00
20041203	1409.42	1355.00	1216.00	745.00
20100403	985.76	975.00	668.00	–

4.1.2 Propagation Time

The ensemble forecasts predicted 5 of the 15 propagation times with accuracy such that the actual propagation time was within the average plus or minus one standard deviation (Figure 19). All 5 of these CMEs had actual propagation times between 30 and 46 hours. Only 2 of the 7 CMEs with actual propagation times between 30 and 46 hours were not accurate enough to predict the actual propagation time within the average plus or minus one standard deviation. The propagation time distributions, for each of the 15 CMEs, are displayed in Appendix B.

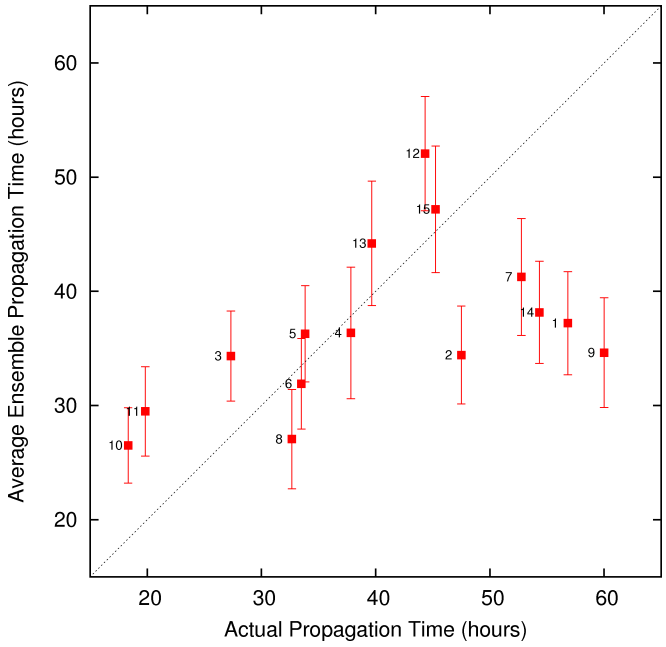

Figure 19. The averages and standard deviations of the propagation time ensembles versus the actual propagation times.

The propagation time for 8 of the 15 ensemble forecasts fell within of the range of the ensemble distribution (Figure 20). Of the 8 forecasts, 7 were for CMEs with actual propagation times between 30 and 46 hours, and the remaining forecast was for a CME with an actual propagation time of around 53 hours. All 7 of the CMEs analyzed with

actual propagation times between 30 and 46 hours were accurate enough to predict the actual propagation time inside of the range of the ensemble.

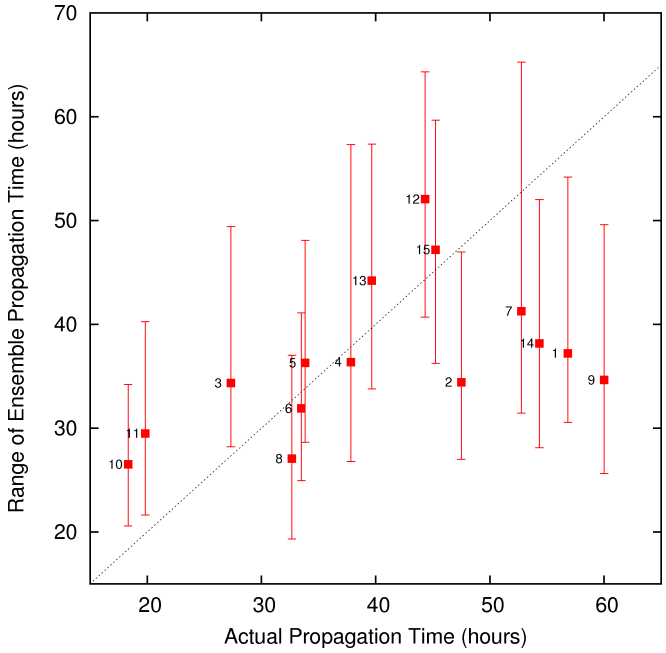

Figure 20. The ranges of the ensemble propagation times versus the actual propagation times.

The average of the ensemble averages, for the 15 CMEs, was calculated to be 36.7 *hours* with a standard deviation of 7.1 *hours* (Table 9). The average of the actual propagation times was calculated to be 40.3 *hours* with a standard deviation of 12.9 *hours*. The standard deviation of actual propagation times was almost twice the standard deviation of the ensemble averages, which indicates that the WSA-ENLIL with Coned Model tended to predict a tight range of propagation times centered around 37 *hours*. This was also indicated from the fact that the minimum and maximum ensemble averages were 26.5 *hours* and 52.1 *hours*, respectively, while the minimum and maximum actual propagation times were 18.3 *hours* and 60.0 *hours*, respectively.

The average of the ensemble standard deviations was calculated to be 4.6 *hours*,

Table 9. The propagation time ensemble statistics for the 15 CMEs, with the averages and standard deviations of the columns at the bottom of the table.

CME date (YYYYMMDD)	actual (hours)	average (hours)	standard deviation (hours)	median (hours)	median absolute deviation (hours)	range (hours)	min (hours)	max (hours)
19990503	56.83	37.21	4.52	36.14	2.23	23.65	30.55	54.20
20000404	47.50	34.42	4.29	33.71	2.76	19.98	27.00	46.98
20000714	27.33	34.34	3.94	33.87	2.33	21.23	28.20	49.43
20010329	37.83	36.36	5.76	35.93	3.65	30.52	26.80	57.32
20010410	33.83	36.29	4.21	35.51	2.79	19.47	28.63	48.10
20010924	33.50	31.90	3.96	31.57	3.17	16.17	24.93	41.10
20011009	52.75	41.26	5.12	40.72	3.13	33.82	31.45	65.27
20011104	32.67	27.06	4.34	26.04	3.19	17.70	19.32	37.02
20011117	60.00	34.63	4.80	34.04	3.75	23.97	25.63	49.60
20031028	18.33	26.51	3.30	26.01	2.37	13.65	20.57	34.22
20031029	19.83	29.49	3.91	29.47	2.56	18.63	21.62	40.25
20040720	44.33	52.06	5.00	51.43	2.89	23.65	40.68	64.33
20041106	39.67	44.20	5.44	43.93	3.66	23.60	33.77	57.37
20041203	54.33	38.16	4.48	37.98	2.48	23.92	28.10	52.02
20100403	45.25	47.18	5.54	46.64	4.50	23.43	36.23	59.67
average	40.27	36.74	4.57	36.20	3.03	22.23	28.23	50.46
std	12.90	7.13	0.69	7.15	0.64	5.17	5.79	9.50

with a standard deviation of 0.7 *hours*. This was an important quantification of the propagation time uncertainty due to the fact that it was based on measurements collected for the particular CME of interest. Another measure of the propagation time uncertainty, derived from LASCO imagery, was the range of the ensembles. The average of the ensemble ranges was calculated to be 22.2 *hours*, with a standard deviation of 5.2 *hours*. While the range was too large of an uncertainty to be useful for operational forecasts, it was an important metric to analyze the overall performance of the ensemble forecasting technique applied to CMEs.

The propagation time forecast errors were also analyzed (Table 10, Figure 21). For this analysis, the forecast error for the propagation time was defined as the ensemble average minus the actual propagation time. A negative forecast error indicated a forecast in which the CME arrived earlier than the actual CME arrival. A positive forecast error indicated a forecast in which the CME arrived after the actual CME arrival.

The ensemble forecasts for CMEs with actual propagation times greater than 46

hours and less than 27 *hours* were inaccurate. As viewed in Figure 21, the absolute forecast errors for events with actual propagation times less than 46 *hours* were less than 10 *hours*, while the absolute forecast errors for events with actual propagation times greater than 46 *hours* were all greater than 10 *hours*. The forecasts for the 8 events with actual propagation times between 27 *hours* and 46 *hours* were the most accurate of the 15 forecasts, with all the absolute forecast errors less than 8 *hours*. The forecast errors for the two fast CMEs, events 10 and 11 (28 and 29 Oct 2003 CMEs), were around 9 *hours*. This indicated that for extremely fast CMEs, with actual propagation times less than 20 *hours*, the ensemble forecast overestimated the propagation time (underestimated the CME velocity).

Table 10. The propagation time forecast errors and performance metrics for the 15 CMEs. The absolute mean and absolute standard deviations of the columns are at the bottom of the table. In this table, *avg* stands for average, *med* stands for median, *std* stands for standard deviation, and *mad* stands for median absolute deviation.

CME date (YYYYMMDD)	avg-actual (hours)	actual inside avg±1 std?	med-actual (hours)	actual inside med±1 mad?	actual inside range?	mean absolute error (hours)	location of associated solar flare
19990503	-19.63	no	-20.69	no	no	19.63	N15E32
20000404	-13.08	no	-13.79	no	no	13.08	N16W66
20000714	7.01	no	6.54	no	no	7.01	N22W07
20010329	-1.47	yes	-1.90	yes	yes	4.70	N20W19
20010410	2.46	yes	1.68	yes	yes	3.70	S23W09
20010924	-1.60	yes	-1.93	yes	yes	3.70	S16E23
20011009	-11.49	no	-12.03	no	yes	11.78	S28E08
20011104	-5.60	no	-6.62	no	yes	6.10	N06W18
20011117	-25.37	no	-25.96	no	no	25.37	S13E42
20031028	8.18	no	7.68	no	no	8.18	S16E08
20031029	9.66	no	9.64	no	no	9.66	S15W02
20040720	7.73	no	7.09	no	yes	7.95	N10E35
20041106	4.54	yes	4.27	no	yes	5.67	N07E00
20041203	-16.17	no	-16.35	no	no	16.17	N09E03
20100403	1.93	yes	1.39	yes	yes	4.70	S25E00
abs mean	9.06		9.17			9.83	
abs std	7.06		7.38			6.35	

The absolute forecast errors, for the slow CMEs with actual propagation times over 46 *hours*, were all greater than 10 *hours*. This indicated that the ensemble forecasts greatly underestimated the propagation times of the slower CMEs. For the

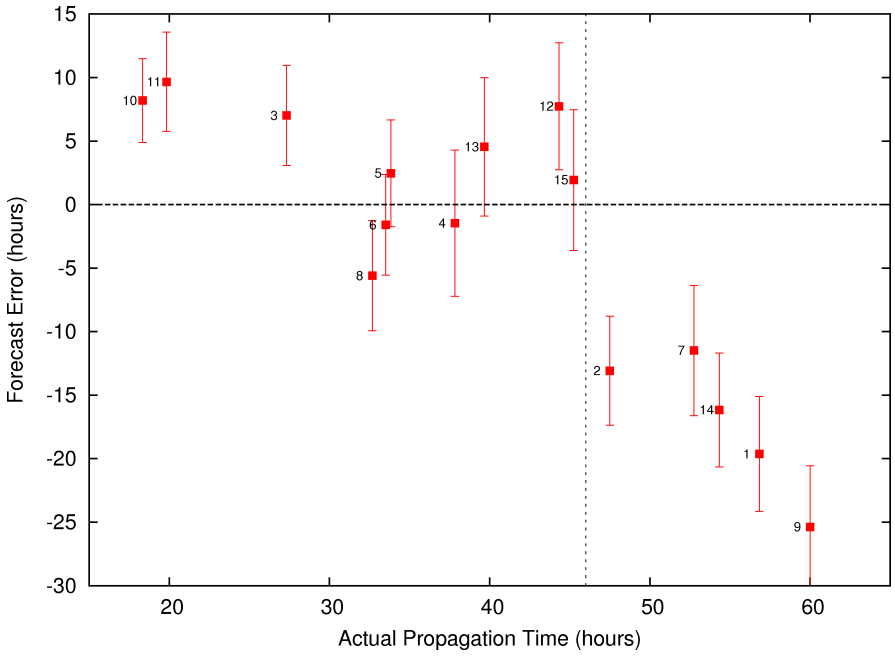

Figure 21. The propagation time forecast error versus the actual propagation time, with the error bars as one standard deviation and the labels as the event number. The dashed vertical line represents the 46 hours point which separated the slower CMEs with absolute forecast errors greater than 10 hours from the CMEs with absolute forecast errors under 10 hours.

events with actual propagation times greater than 50 *hours*, the absolute forecast error increased as the actual propagation time increased. The slowest event (event 9), had an actual propagation time of 60.0 *hours* and a forecast error of -25 *hours*.

The large forecasting errors for the slower CMEs were most likely due to the combination of velocity overestimations and misrepresentations of the propagation axis orientations. The Coned Model tended to push the propagation axes towards the Sun-Earth line, which most likely was not an accurate representation for all of the actual propagation axes. The optimization routine used by the Coned Model to calculate the cone parameters forced the CME velocity to have an inverse relationship to the magnitude of the propagation axis angles (latitude/longitude) and the angular width. This relationship is apparent from Figure 22, where cone parameters and propagation times for each of the 100 sets of parameters composing the ensemble

are displayed separately, for event 1 (3 May 1999 CME). The sets of cone parameters with the largest magnitude in propagation axis angles also have the slowest velocities, and therefore the longest propagation times. This indicated that if the Coned Model would force solutions with larger propagation axis angles for the slower events, then it would also force slower velocities. The combination of less direct propagation paths to Earth as well as decreases in the velocities would help to raise the propagation time forecasts for the slower events.

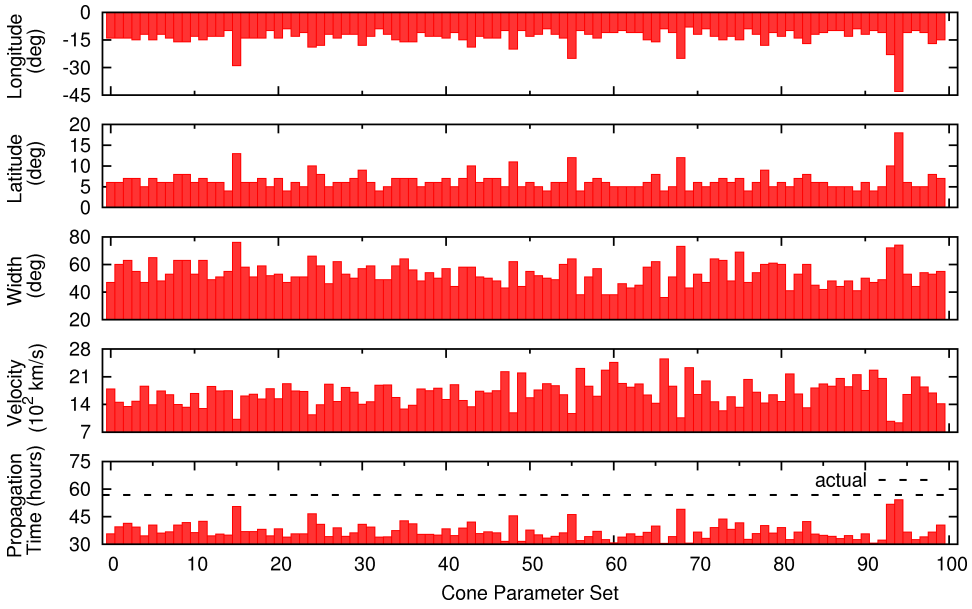

Figure 22. The cone parameters and propagation time forecasts for each of the 100 sets of parameters composing the ensemble for event 1 (3 May 1999 CME). The inverse relationship between the magnitude of the propagation axis angles (latitude/longitude) and the velocity is apparent.

The mean absolute forecast error, for the 15 CMEs, was calculated to be 9.1 *hours* with a standard deviation of 7.1 *hours*. This mean absolute forecast error was greater than the mean absolute error of 6.9 *hours* found by *Taktakishvili et al.* [2011] using single ENLIL runs with the analytical Cone Model, but was less than the 11.2 *hour* mean absolute error found by *Taktakishvili et al.* [2011] using single ENLIL runs with

the median values of the cone parameters derived from the Coned Model (automatic Cone Model). It is worthwhile to note that the events analyzed by this analysis were not the same as the events analyzed by the *Taktakishvili et al.* [2011] analysis, so the errors are not directly comparable.

The large standard deviation in the absolute forecast error indicated that there was a large range of forecast errors. The largest absolute forecast errors were due to the slower CMEs with actual propagation times greater than 46 $hours$. The mean absolute forecast error with the five slower CMEs removed from the set was 5.0 $hours$, with a standard deviation of 3.1 $hours$. If the large forecast errors for the slower CMEs could somehow be reduced (by model improvements), then the ensemble forecasting technique using the WSA-ENLIL with Coned Model would be more accurate than the single runs using WSA-ENLIL with the analytical Cone Model.

An attempt to reduce the magnitude of the large forecasting errors from the slower CMEs was completed by rerunning the ensemble forecasts using Coned Model version 1.2. Coned Model version 1.2 was known to produce slower velocity estimates than version 1.3, so the events were rerun with the older version of the Coned Model to increase the propagation times and decrease the forecast errors. These results will be discussed in Section 4.2.

4.1.3 Maximum K_p

The ensemble forecast tended to overestimate the magnitude of the impact of the CME by forecasting a maximum K_p of 9 for all 15 CMEs in the analysis (Table 11). The forecast overestimated all of the maximum K_p predictions less than 9, and was not able to predict the lower maximum K_p values since the computation assumed the IMF was completely southward. Only 7 of the 15 CMEs had an actual maximum K_p of 9. The actual maximum K_p for 3 of the CMEs were less than 5, in which case the

ensemble forecasts were extremely overestimated. The ensemble forecasts for 10 of the 15 CMEs had accuracy such that the actual maximum K_p was within the range of the ensemble (Figure 23). Only 3 of the 8 CMEs with actual maximum K_p indices of less than 9 had ensemble forecasts which contained the actual maximum K_p inside of the range of the ensemble. The K_p distributions, for each of the 15 CMEs, are displayed in Appendix B.

Table 11. The maximum K_p index ensemble statistics for the 15 CMEs, with the average and standard deviation of the columns at the bottom of the table.

CME date (YYYYMMDD)	actual	average	standard deviation	median	median absolute deviation	range	min	max
19990503	3	9	0	9	0	0	9	9
20000404	9	9	0	9	0	0	9	9
20000714	9	9	0	9	0	0	9	9
20010329	9	8.98	0.20	9	0	2	7	9
20010410	8	9	0	9	0	0	9	9
20010924	7	9	0	9	0	0	9	9
20011009	6	8.95	0.40	9	0	4	5	9
20011104	9	9	0	9	0	0	9	9
20011117	4	9	0	9	0	0	9	9
20031028	9	9	0	9	0	0	9	9
20031029	9	9	0	9	0	0	9	9
20040720	7	8.76	0.44	9	0	2	7	9
20041106	9	9	0	9	0	0	9	9
20041203	4	9	0	9	0	0	9	9
20100403	8	8.79	0.57	9	0	3	6	9
average	7.33	8.97	0.11	9.00	0.00	0.74	8.26	9.00
std	2.13	0.08	0.20	0.00	0.00	1.34	1.34	0.00

The forecast error for the maximum K_p was defined as the ensemble median minus the actual maximum K_p. The median was used instead of the average due to the fact that the rounded average was the median, for all of the maximum K_p distributions in this analysis. The mean absolute forecast error, for all 15 events, was calculated to be 1.66 with a standard deviation of 2.13 (Table 12). The mean absolute forecast error for the 7 events with actual maximum K_p indices equal to 9 was 0.00, and the mean absolute forecast error for the 8 events with actual maximum K_p indices less than 9 was 3.13.

The average of the ensemble standard deviations was calculated to be 0.11 with

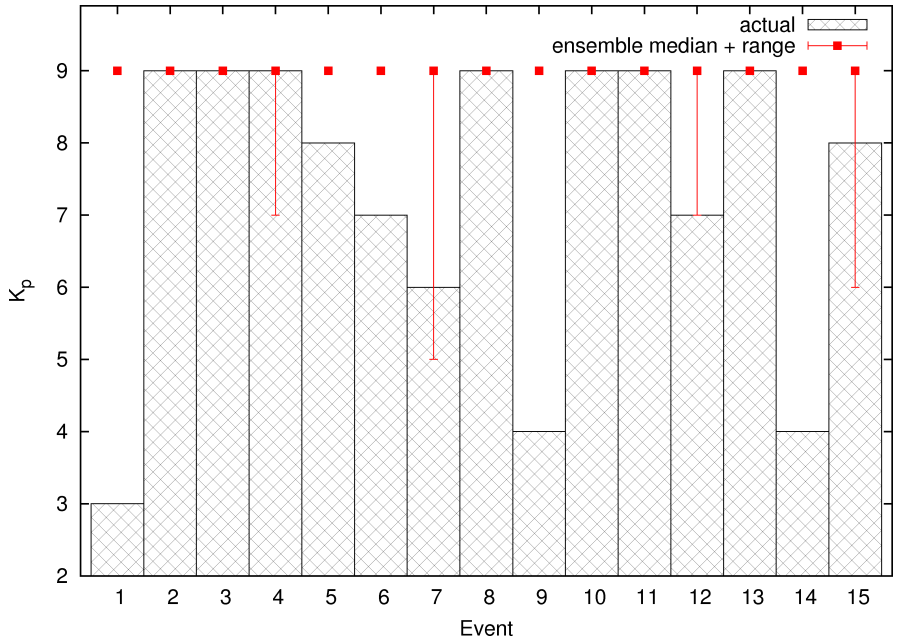

Figure 23. The median and range of the ensemble maximum K_p index forecast along with the actual maximum K_p index per event for the 15 CMEs.

a standard deviation of 0.20. The ensemble standard deviation was zero for all but 4 events, which was due to the overestimation of the maximum K_p values and the fact that any maximum K_p calculation over 9 were rounded down to 9. The average of the ensemble ranges was calculated to be 0.74 with a standard deviation of 1.34. Similar to the ensemble standard deviations, only 4 of the events had nonzero ranges due to the overestimation of the maximum K_p values. This provided a quantification of the uncertainty in the maximum K_p calculations, but due to the overestimation of the maximum K_p values, only 4 events have nonzero uncertainties.

The maximum K_p is displayed with the propagation time, per event, in Figure 24. The events with the largest propagation time errors also have the largest maximum K_p errors. This was due to overestimations of the CME velocities for these particular events, which forecast the arrival time too early, and the maximum K_p too large.

Table 12. The maximum K_p forecast errors and performance metrics for the 15 CMEs, with the absolute mean and absolute standard deviation of the columns at the bottom of the table. In this table, *avg* stands for average, *med* stands for median, *std* stands for standard deviation, and *mad* stands for median absolute deviation.

CME date (YYYYMMDD)	avg-actual	actual inside avg±1 std?	med-actual	actual inside med±1 mad?	actual inside range?	mean absolute error	location of associated solar flare
19990503	6	no	6	no	no	6	N15E32
20000404	0	yes	0	yes	yes	0	N16W66
20000714	0	yes	0	yes	yes	0	N22W07
20010329	-0.02	yes	0	yes	yes	0.02	N20W19
20010410	1	no	1	no	no	1	S23W09
20010924	2	no	2	no	no	2	S16E23
20011009	2.95	no	3	no	yes	2.970467	S28E08
20011104	0	yes	0	yes	yes	0	N06W18
20011117	5	no	5	no	no	5	S13E42
20031028	0	yes	0	yes	yes	0	S16E08
20031029	0	yes	0	yes	yes	0	S15W02
20040720	1.76	no	2	no	yes	1.76	N10E35
20041106	0	yes	0	yes	yes	0	N07E00
20041203	5	no	5	no	no	5	N09E03
20100403	0.79	no	1	no	yes	0.90	S25E00
abs mean	1.63		1.67			1.64	
abs std	2.13		2.13			2.12	

4.1.3.1 Magnetic Field Clock-angle

All of the previous maximum K_p calculations assumed that the magnetic field was completely southward such that the clock-angle, θ_c, was equal to π. This provided the worst case scenario for the impact of a CME, but it overestimated the maximum K_p for CMEs with actual maximum K_p indices less than 9. Since no magnetic field orientation information was available from ENLIL, one method of accounting for the variable clock-angle was to use the expected value of the $\sin^{8/3}(\theta_c/2)$ term in the *Newell et al.* [2007] maximum K_p formula, assuming that the clock-angle was randomly oriented with a uniform distribution.

For a randomly oriented clock-angle with a uniform distribution, the expected value of the clock-angle term is

$$\left\langle \sin^{8/3}\left(\frac{\theta_c}{2}\right)\right\rangle = \frac{1}{2\pi}\int_0^{2\pi} \sin^{8/3}\left(\frac{\theta_c}{2}\right) d\theta_c = \frac{5\sqrt{\pi}}{4\,\Gamma\left(\frac{1}{6}\right)\Gamma\left(\frac{4}{3}\right)} \approx 0.45. \qquad (30)$$

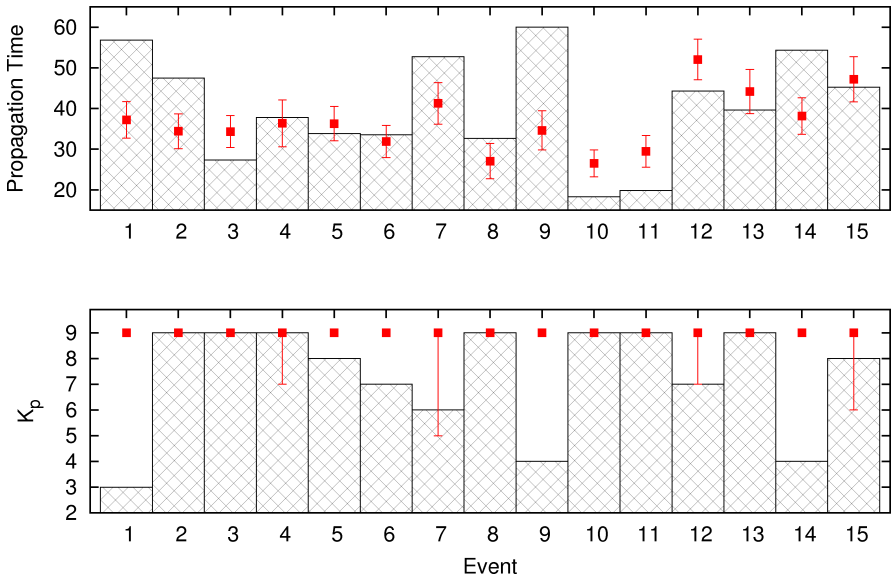

Figure 24. The median and range of the maximum K_p along with the average and standard deviation of the propagation time per event for the 15 CMEs. The ensemble forecasts and uncertainties are the red points with red error bars, and the bars are the actual values.

This scaling factor of 0.45 could be used to calculate the maximum K_p, and would provide a lower bound for a range of possible maximum K_p values when computed along with the completely southward IMF assumption. The *Newell et al.* [2007] maximum K_p formula, using the expected value for the clock-angle term, may be described by

$$K_p = 0.0002947\, v^{4/3} B_T^{2/3} sin^{8/3}(\theta_c/2) + 1 \approx 0.0002947\, v^{4/3} B_T^{2/3}(0.45) + 1. \qquad (31)$$

Using the expected value for the clock-angle term, the ensemble forecasts no longer predicted a maximum K_p of 9 for all of the events (Table 13 and Figure 25). The forecasts for 9 of the 15 events had accuracy such that the actual maximum K_p lay within the range of the ensemble (Table 14). The forecasts for 4 of the 8 CMEs with an actual maximum K_p less than 9 had the actual maximum K_p within the range of the ensemble, which was slightly better than the 3 of 8 for the completely southward IMF

forecasts. But, the forecasts using the expected value for the clock-angle term tended to underestimate the maximum K_p indices for the events with actual maximum K_p indices of 9, with accurate forecasts for 5 of the 7 events.

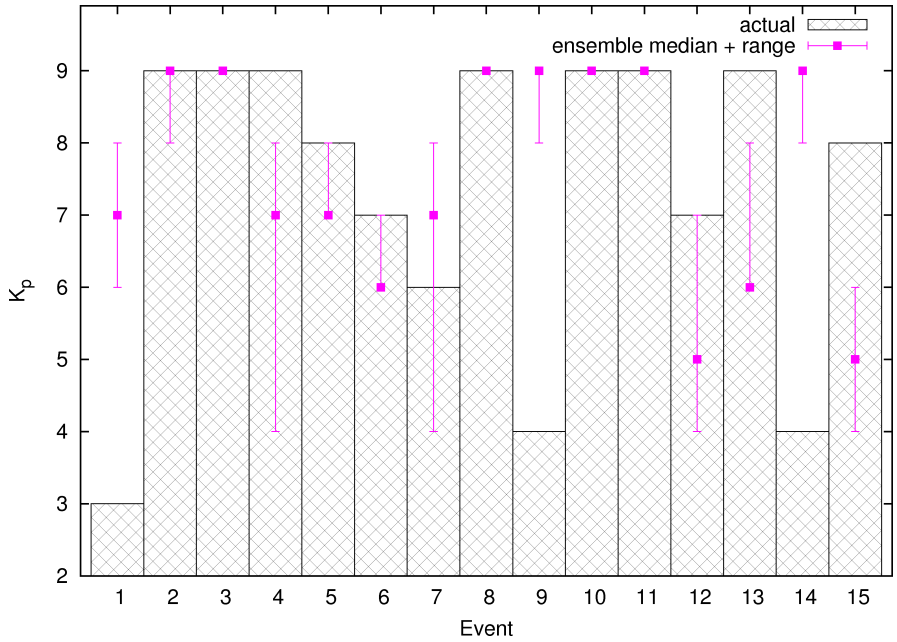

Figure 25. The median and range of the maximum K_p ensemble using the expected value of the clock-angle term in the *Newell et al.* [2007] formula along with the actual maximum K_p index, per event, for the 15 CMEs.

The average of the ensemble standard deviations, using the expected value for the clock-angle term, was calculated to be 0.29 with a standard deviation of 0.25. The ensemble standard deviation was zero for 4 of the events. The average of the ensemble range was calculated to be 1.47 with a standard deviation of 1.36. Similar to the ensemble standard deviations, 4 of the events had ranges of zero. The uncertainty quantification using the expected value for the clock-angle term was more useful than the uncertainty quantification assuming the magnetic field was completely southward due to the fact that only 4 of the events had zero standard deviations and ranges compared to 11 events when the IMF was assumed to be completely southward.

Table 13. The maximum K_p index ensemble statistics for the 15 CMEs using the expected value for the clock-angle term in the *Newell et al.* [2007] formula. The averages and standard deviations of the columns are displayed at the bottom of the table.

CME date (YYYYMMDD)	actual	average	standard deviation	median	median absolute deviation	range	min	max
19990503	3	7.07	0.29	7	0	2	6	8
20000404	9	8.94	0.24	9	0	1	8	9
20000714	9	9	0	9	0	0	9	9
20010329	9	6.95	0.44	7	0	4	4	8
20010410	8	7.11	0.31	7	0	1	7	8
20010924	7	6.30	0.46	6	0	1	6	7
20011009	6	7.21	0.59	7	0	4	4	8
20011104	9	9	0	9	0	0	9	9
20011117	4	8.99	0.10	9	0	1	8	9
20031028	9	9	0	9	0	0	9	9
20031029	9	9	0	9	0	0	9	9
20040720	7	5.51	0.78	5	0	3	4	7
20041106	9	6.50	0.52	6	0	2	6	8
20041203	4	8.98	0.14	9	0	1	8	9
20100403	8	5.10	0.52	5	0	2	4	6
average	7.33	7.64	0.29	7.53	0.00	1.47	6.73	8.20
std	2.13	1.42	0.25	1.55	0.00	1.36	2.02	0.94

The mean absolute forecast error for the maximum K_p ensembles using the expected value of the clock-angle term was calculated to be 1.80, compared to 1.67 for the maximum K_p ensembles assuming the IMF was completely southward. The calculated skill score for the expected value of the clock-angle term maximum K_p forecast versus the completely southward IMF maximum K_p forecast was -0.08. This implied that using the expected value of the clock-angle term created slightly less accurate forecasts for the 15 CMEs in this analysis.

The mean absolute forecast error for the events with actual maximum K_p indices of 9 was 0.71, which was greater than the mean absolute forecast error of 0.00 for the completely southward IMF forecasts. The mean absolute forecast error for the events with actual maximum K_p indices less than 9 was 2.75, which was less than the mean absolute forecast error of 3.13 for the completely southward IMF forecasts. This indicated that the forecasts completed using the expected value for the clock-angle term were less accurate than the forecasts completed using a completely southward IMF for the events with actual maximum K_p indices of 9, but were more accurate for

Table 14. The maximum K_p forecast errors and performance metrics for the 15 CMEs using the expected value of the clock-angle term in the *Newell et al.* [2007] formula. The absolute mean and absolute standard deviation of the columns are displayed at the bottom of the table. In this table, *avg* stands for average, *med* stands for median, *std* stands for standard deviation, and *mad* stands for median absolute deviation.

CME date (YYYYMMDD)	avg-actual	actual inside avg±1 std?	med-actual	actual inside med±1 mad?	actual inside range?	mean absolute error	location of associated solar flare
19990503	4.07	no	4	no	no	4.07	N15E32
20000404	-0.06	yes	0	yes	yes	0.06	N16W66
20000714	0	yes	0	yes	yes	0	N22W07
20010329	-2.05	no	-2	no	no	2.05	N20W19
20010410	-0.89	no	-1	no	yes	0.89	S23W09
20010924	-0.70	no	-1	no	yes	0.7	S16E23
20011009	1.21	no	1	no	yes	1.25	S28E08
20011104	0	yes	0	yes	yes	0	N06W18
20011117	4.99	no	5	no	no	4.99	S13E42
20031028	0	yes	0	yes	yes	0	S16E08
20031029	0	yes	0	yes	yes	0	S15W02
20040720	-1.49	no	-2	no	yes	1.49	N10E35
20041106	-2.50	no	-3	no	no	2.5	N07E00
20041203	4.98	no	5	no	no	4.98	N09E03
20100403	-2.90	no	-3	no	no	2.90	S25E00
abs mean	1.72		1.80			1.73	
abs std	1.80		1.82			1.80	

the events with actual maximum K_p indices less than 9.

The maximum K_p forecasts for 8 of the 15 events were lowered by using the expected value for the clock-angle term (Figure 26). The forecasts were underestimated for 6 of the events using the expected value for the clock-angle term. Only 4 of the events were overestimated (events 1, 7, 9 and 14), which were all the slower events with the overestimated velocities from the Coned Model version 1.3. The overestimation of the velocities became apparent in the overestimation of the maximum K_p indices for these events.

Even though 6 of the events were underestimated, the general trend of the forecast maximum K_p indices followed the general trend of the actual maximum K_p indices, except for events 1, 9 and 14, which were greatly overestimated by the ensemble forecast. The low actual maximum K_p indices for events 1, 9, and 14 were due to the fact that the orientation of the actual CMEs magnetic field was not conducive to producing large geomagnetic storms (see Section 4.2.2 for more detail).

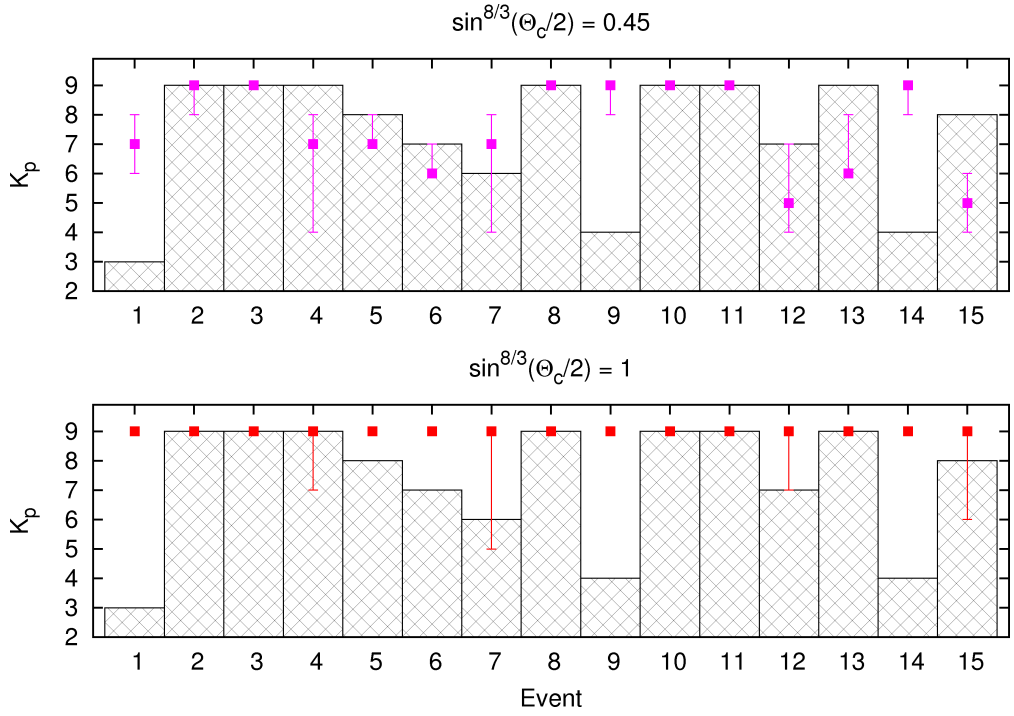

Figure 26. The median and range of the maximum K_p, per event, using both the expected value for the clock-angle term in the *Newell et al.* [2007] formula and assuming the magnetic field is completely southward. The points with error bars are from the ensemble forecasts, and the bars are the actual maximum K_p indices.

Overall, the maximum K_p index forecasts using the expected value for the clock-angle term provided an alternative method for forecasting the maximum K_p index which provided less-conservative estimates. The combination of forecasts assuming the magnetic field is completely southward along with using the expected value for the clock-angle term would provide a worst-case and a less-conservative forecast, which could provide a useful range for an operational forecast.

4.1.4 Relative Performance and Skill Score

The ensemble forecast using the WSA-ENLIL with Coned Model outperformed all of the reference models with respect to predicting the propagation time. The ensemble forecast had a positive skill score when compared to the propagation times

derived from the LASCO first-order POS velocity, the Coned Model average velocity, the type II speed, STOA, ISPM, and the ENLIL single-shot estimates (Table 15).

Table 15. The model skill score of the propagation time ensemble forecasts versus the propagation times derived from the LASCO first-order POS velocity,the Coned Model average velocity, the type II speed, STOA, ISPM, and the ENLIL single-shot estimates.

ensemble average vs ensemble median	ensemble average vs LASCO POS first-order velocity	ensemble average vs Coned Model average velocity	ensemble average vs type II velocity	ensemble average vs STOA	ensemble average vs ISPM	ensemble average vs ENLIL single shot
0.01	0.32	0.35	0.46	0.46	0.60	0.01

Four of the events did not have type II data available, so they were not included in the skill score calculations. Both STOA and ISPM required type II speeds as input, so the four events without type II data were not included in the calculation of the skill scores. One additional event, event 12 (20 July 2004 CME), was also not included in the skill score calculations due to the fact that both STOA and ISPM predicted that the shock would decay before it reached Earth. The ensemble forecast performed more accurately than two of the models currently used by AFWA to predict CME arrival times.

The ensemble forecasts performed essentially the same as the ENLIL single-shot estimates, which agreed with the fact that the ENLIL single-shot forecasts were composed of the median values of the cone parameters and should provide a similar forecast to the average of the ensemble forecast. The ENLIL single-shot predictions for the maximum K_p index were exactly the same as the median values for the ensemble forecast. The main difference between the ensemble forecasts and the ENLIL single-shot predictions was the fact that the ensemble provided a means to quantify the uncertainty of the forecast while the single-shot did not.

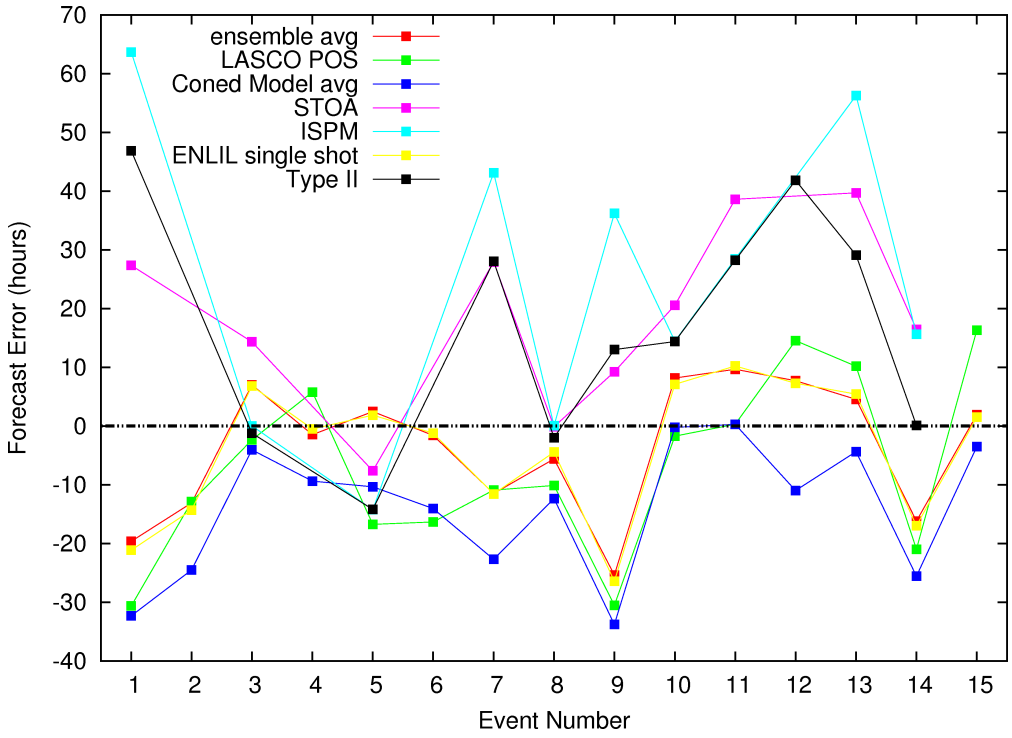

Figure 27. The propagation time forecast error of the ensemble and the reference models for the 15 CMEs. The forecast error was defined as the model prediction minus the actual propagation time.

For the propagation time, the forecasts using the median of the ensembles and the average of the ensembles were essentially the same. For the maximum K_p, the rounded average of the ensemble forecast was the same as the median of the ensemble forecast for all of the CMEs. This indicated that either the average or median could be used to describe the ensemble distributions, with no loss in accuracy.

While the skill scores show that the overall performance of the ensemble forecasts were more accurate than the reference models, the propagation time forecasts were not more accurate for every CME analyzed (Table 16 and Figure 27). The majority of events had at least one reference model out-perform the ensemble forecast for the particular event. The ENLIL single-shot forecast error and ensemble forecast error were almost equal for all of the 15 CMEs.

Table 16. The actual propagation times along with the predicted propagation times from the ensemble average, LASCO first-order POS velocity, the Coned Model average velocity, the type II speed, STOA, ISPM, and the ENLIL single-shot. The bold values were the most accurate forecast for each event.

CME date (YYMMDD)	actual (hours)	ensemble average (hours)	LASCO POS first order velocity (hours)	Coned Model average velocity (hours)	type II velocity (hours)	STOA (hours)	ISPM (hours)	ENLIL single shot (hours)
19990503	56.83	**37.21**	26.18	24.53	103.69	84.18	120.52	35.70
20000404	47.50	34.42	**34.63**	22.99	–	–	–	33.21
20000714	27.33	34.34	24.98	23.27	26.14	41.68	**27.37**	34.13
20010329	37.83	**36.36**	43.64	28.46	–	–	–	37.33
20010410	33.83	36.29	17.10	23.48	19.63	26.20	19.58	**35.68**
20010924	33.50	31.90	17.18	19.44	–	–	–	**32.28**
20011009	52.75	41.26	**41.86**	30.05	80.81	80.70	95.88	41.20
20011104	32.67	27.06	22.54	20.31	30.70	32.55	**32.72**	28.25
20011117	60.00	34.63	29.50	26.22	73.03	**69.23**	96.20	33.58
20031028	18.33	26.51	16.63	**18.11**	32.71	38.92	32.78	25.45
20031029	19.83	29.49	20.14	**20.13**	48.08	58.47	48.30	30.05
20040720	44.33	52.06	58.87	33.37	86.19	MHD-Decay	MHD-Decay	**51.63**
20041106	39.67	44.20	49.84	**35.31**	68.78	79.38	95.93	45.10
20041203	54.33	38.16	33.35	28.77	**54.44**	70.82	69.97	37.37
20100403	45.25	47.18	61.58	41.73	–	–	–	**46.75**

4.2 Coned Model Version 1.2

Overall, the propagation time ensemble forecast using Coned Model version 1.2 was less accurate than Coned Model version 1.3, while the maximum K_p ensemble forecast using Coned Model version 1.2 was slightly more accurate than Coned Model version 1.3. The input parameter distributions, derived from Coned Model version 1.2, are displayed in Appendix C.

4.2.1 Propagation Time

The propagation time ensemble forecasts using Coned Model version 1.2 tended to be inaccurate due to overestimations of the propagation times (Tables 17 and 18). The propagation time ensemble forecasts for 4 of the 15 events were predicted with accuracy such that the actual propagation time lay within the average plus or minus one standard deviation, and 7 of the 15 ensemble ranges contained the actual

propagation time (Figures 28 and 29). Coned Model version 1.2 overestimated the propagation times for CMEs with actual propagation times less than 46 *hours*. For CMEs with actual propagation times over 46 *hours*, the forecasts were mostly accurate. The actual propagation time was within 3 out of 5 average ensemble forecasts plus or minus one standard deviation for the events with actual propagation times greater than 46 *hours*. All 5 of the ensemble ranges, for the events actual propagation times over 46 *hours*, contained the actual propagation times. This indicated that Coned Model version 1.2 accurately predicted the CME velocities for the slower events.

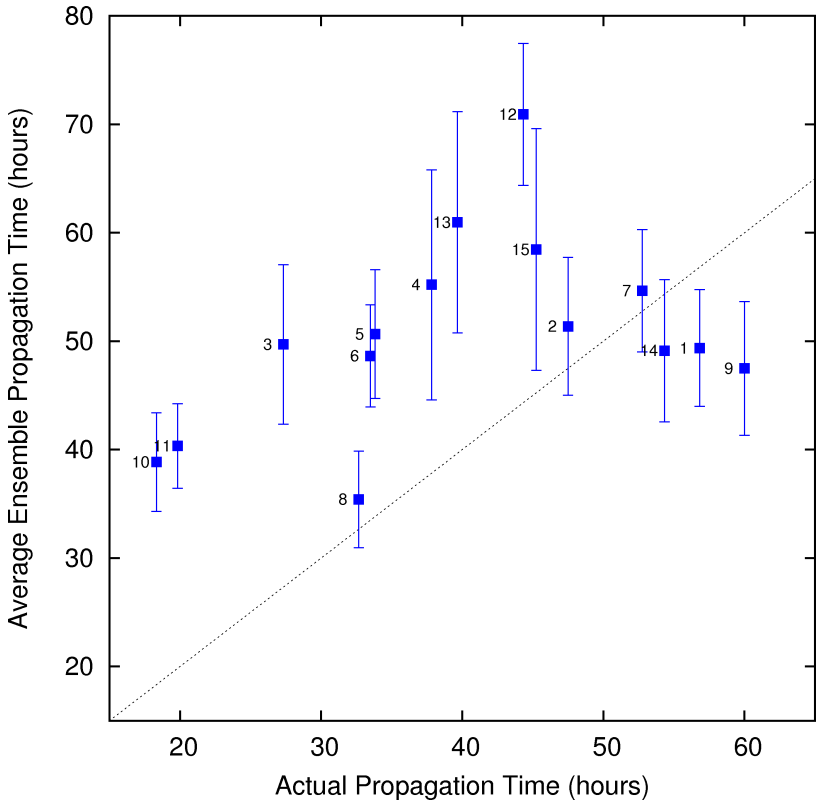

Figure 28. The propagation time ensemble averages and standard deviations versus the actual propagation times, for the 15 CMEs, using Coned Model version 1.2.

For the 10 CMEs with actual propagation times less than 46 *hours*, 1 had the

actual propagation time within the average plus or minus one standard deviation, and 2 had the actual propagation time inside the ensemble range. This indicated that Coned Model version 1.2 underestimated the CME velocities for the events with actual propagation times less than 46 *hours*, which agreed with the *Falkenberg et al.* [2011] analysis.

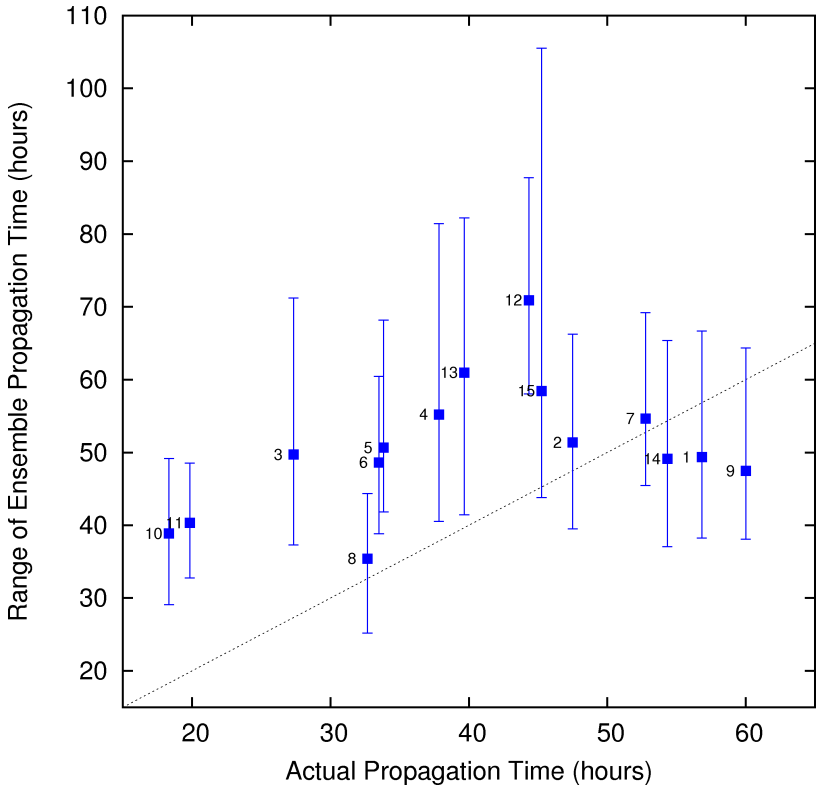

Figure 29. The ranges of the ensemble propagation times versus the actual propagation times, for the 15 CMEs, using Coned Model version 1.2.

The forecast error was positive for all events except for 3 (Figure 30). The 3 events with negative forecast errors all had propagation times greater than 54 *hours*. Of the 10 events with actual propagation times less than 46 *hours*, 9 had forecast errors greater than 10 *hours*, with 5 of the events having forecast errors greater than 20 *hours*. This supports the conclusions of the *Falkenberg et al.* [2011] analysis, which

Table 17. The propagation time ensemble statistics for the 15 CMEs, using Coned Model version 1.2. The average and standard deviation of the columns are displayed at the bottom of the table.

CME date (YYYYMMDD)	actual (hours)	average (hours)	standard deviation (hours)	median (hours)	median absolute deviation (hours)	range (hours)	min (hours)	max (hours)
19990503	56.83	49.36	5.39	48.47	3.01	28.45	38.23	66.68
20000404	47.50	51.37	6.35	50.97	4.50	26.73	39.52	66.25
20000714	27.33	49.70	7.35	49.34	5.58	33.95	37.28	71.23
20010329	37.83	55.20	10.61	53.24	7.32	40.87	40.53	81.40
20010410	33.83	50.65	5.94	49.49	3.08	26.35	41.82	68.17
20010924	33.50	48.64	4.70	47.93	2.89	21.63	38.83	60.47
20011009	52.75	54.64	5.64	53.58	3.68	23.73	45.45	69.18
20011104	32.67	35.41	4.44	34.92	2.92	19.15	25.18	44.33
20011117	60.00	47.48	6.16	46.76	4.00	26.25	38.10	64.35
20031028	18.33	38.85	4.56	38.63	3.75	20.07	29.08	49.15
20031029	19.83	40.33	3.90	40.36	2.99	15.77	32.75	48.52
20040720	44.33	70.91	6.54	70.23	4.86	29.68	58.03	87.72
20041106	39.67	60.96	10.20	59.80	7.62	40.77	41.43	82.20
20041203	54.33	49.12	6.55	47.87	4.26	28.32	37.07	65.38
20100403	45.25	58.45	11.14	57.37	6.76	61.70	43.80	105.50
average	40.27	50.74	6.63	49.93	4.48	29.56	39.14	68.70
std	12.90	8.91	2.28	8.68	1.63	11.41	7.46	15.94

found that Coned Model version 1.2 tended to underestimate the velocities of the CMEs. But, Coned Model version 1.2 tended to correctly predict the CME velocities of the events with actual propagation times greater than 46 *hours* (slower CMEs).

The mean absolute forecast error, for the 15 CMEs, was calculated to be 13.8 *hours* with a standard deviation of 8.0 *hours*. This mean absolute forecast error was greater than the mean absolute error of 6.9 *hours* found by *Taktakishvili et al.* [2011] using single ENLIL runs with the analytical Cone Model, and the 11.2 *hours* mean absolute error found by *Taktakishvili et al.* [2011] using single ENLIL runs with the Coned Model (automatic Cone Model). It must be noted that these errors are not directly comparable due to the fact that they were not analyzing the same set of events. Relative to the 9.1 *hour* mean absolute forecast error produced by Coned Model version 1.3, the 13.8 *hour* mean absolute forecast error was significantly greater.

Table 18. The propagation time forecast errors and performance metrics for the 15 CMEs, using Coned Model version 1.2. The absolute mean and absolute standard deviation of the columns are displayed at the bottom of the table. In this table, *avg* stands for average, *med* stands for median, *std* stands for standard deviation, and *mad* stands for median absolute deviation.

CME date (YYYYMMDD)	avg-actual (hours)	actual inside avg±1 std?	med-actual (hours)	actual inside med±1 mad?	actual inside range?	mean absolute error (hours)	location of associated solar flare
19990503	-7.47	no	-8.37	no	yes	8.07	N15E32
20000404	3.87	yes	3.47	yes	yes	5.68	N16W66
20000714	22.37	no	22.01	no	no	22.37	N22W07
20010329	17.37	no	15.41	no	no	17.37	N20W19
20010410	16.82	no	15.66	no	no	16.82	S23W09
20010924	15.14	no	14.43	no	no	15.14	S16E23
20011009	1.89	yes	0.83	yes	yes	4.62	S28E08
20011104	2.75	yes	2.26	yes	yes	4.20	N06W18
20011117	-12.52	no	-13.24	no	yes	12.71	S13E42
20031028	20.52	no	20.30	no	no	20.52	S16E08
20031029	20.49	no	20.53	no	no	20.49	S15W02
20040720	26.58	no	25.90	no	no	26.58	N10E35
20041106	21.30	no	20.14	no	no	21.30	N07E00
20041203	-5.21	yes	-6.46	no	yes	7.41	N09E03
20100403	13.20	no	12.12	no	yes	13.25	S25E00
abs mean	13.83		13.41			14.44	
abs std	7.95		7.75			7.16	

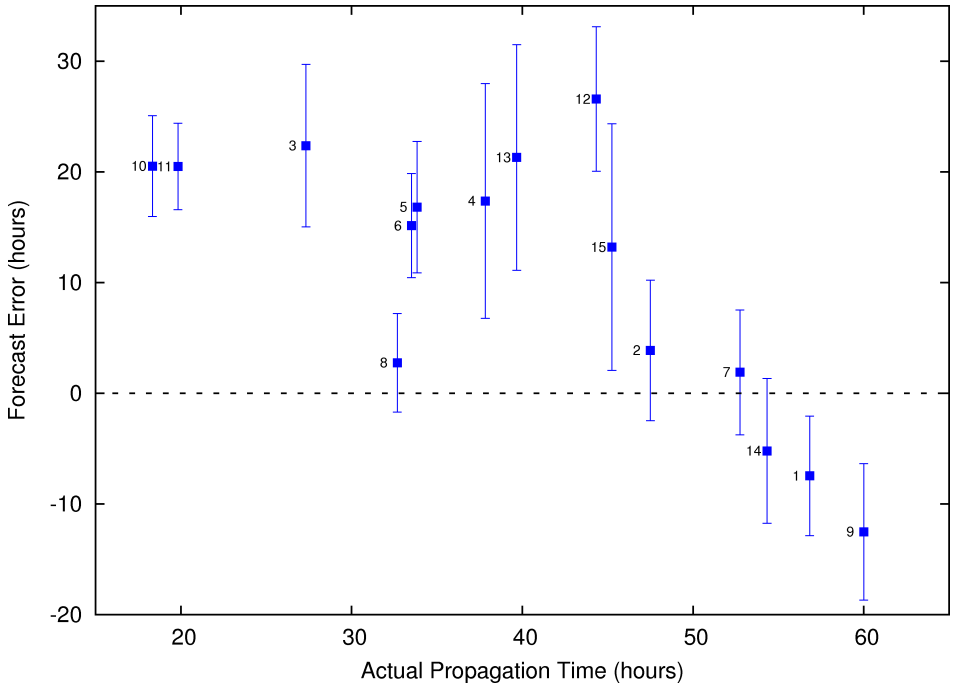

Figure 30. The propagation time forecast error versus the actual propagation time, using Coned Model version 1.2, with the standard deviations as the error bars and the event numbers as the labels.

4.2.2 Maximum K_p

As a whole, the maximum K_p estimates using Coned Model version 1.2 were slightly overestimated (Tables 19 and 20). The maximum K_p was overestimated for 4 events, underestimated for 4 events, and forecast perfectly for 7 events. The magnitude of the positive forecast errors (overestimations) were larger than the magnitude of the negative forecast errors.

Table 19. The maximum K_p index ensemble statistics for the 15 CMEs, using Coned Model version 1.2. The average and standard deviation of the columns are displayed at the bottom of the table.

CME date (YYYYMMDD)	actual	average	standard deviation	median	median absolute deviation	range	min	max
19990503	3	8.91	0.20	9	0	1	8	9
20000404	9	8.95	0.22	9	0	1	8	9
20000714	9	8.98	0.20	9	0	2	7	9
20010329	9	7.11	1.35	8	1	6	3	9
20010410	8	8.29	0.56	8	0	2	7	9
20010924	7	6.91	0.29	7	0	1	6	7
20011009	6	6.61	0.55	7	0	2	5	7
20011104	9	9	0	9	0	0	9	9
20011117	4	8.97	0.15	9	0	1	8	9
20031028	9	9	0	9	0	0	9	9
20031029	9	9	0	9	0	0	9	9
20040720	7	5.13	0.49	5	0	2	4	6
20041106	9	6.50	1.33	7	1	5	4	9
20041203	4	8.90	0.36	9	0	2	7	9
20100403	8	5.25	1.13	6	0	4	3	7
average	7.33	7.83	0.45	8.00	0.13	1.96	6.44	8.40
std	2.13	1.44	0.46	1.31	0.35	1.78	2.15	1.06

The ensemble forecasts for 10 of the 15 CMEs contained the actual maximum K_p inside of the range of the ensemble (Figure 31). The mean absolute forecast error, for the 15 events, was calculated to be 1.60 with a standard deviation of 2.10. The mean absolute forecast error for the events with actual maximum K_p indices of 9 was 0.43 with a standard deviation of 0.79, while the mean absolute forecast error for the events with actual maximum K_p indices less than 9 was 2.63 with a standard deviation of 2.39. This indicated that the majority of the error was for the events with actual maximum K_p indices less than 9.

Table 20. The maximum K_p forecast errors and performance metrics for the 15 CMEs, using Coned Model version 1.2. The absolute mean and absolute standard deviation of the columns are displayed at the bottom of the table. In this table, *avg* stands for average, *med* stands for median, *std* stands for standard deviation, and *mad* stands for median absolute deviation.

CME date (YYYYMMDD)	avg-actual	actual inside avg±1 std?	med-actual	actual inside med±1 mad?	actual inside range?	mean absolute error	location of associated solar flare
19990503	5.91	no	6	no	no	5.91	N15E32
20000404	-0.05	yes	0	yes	yes	0.05	N16W66
20000714	-0.02	yes	0	yes	yes	0.02	N22W07
20010329	-1.89	no	-1	yes	yes	1.89	N20W19
20010410	0.29	yes	0	yes	yes	0.44	S23W09
20010924	-0.09	yes	0	yes	yes	0.24	S16E23
20011009	0.61	no	1	no	yes	0.67	S28E08
20011104	0	yes	0	yes	yes	0	N06W18
20011117	4.97	no	5	no	no	4.97	S13E42
20031028	0	yes	0	yes	yes	0	S16E08
20031029	0	yes	0	yes	yes	0	S15W02
20040720	-1.87	no	-2	no	no	1.90	N10E35
20041106	-2.50	no	-2	no	yes	2.51	N07E00
20041203	4.90	no	5	no	no	4.90	N09E03
20100403	-2.75	no	-2	no	no	2.77	S25E00
abs mean	1.72		1.60			0.50	
abs std	2.08		2.10			2.70	

The maximum K_p was significantly overestimated for events 1, 9 and 14, even though the propagation time forecasts were only slightly underestimated (velocities were slightly overestimated). But, even with appropriate velocities, the maximum K_p forecasts were overestimated (Figure 32). For these events, the maximum K_p overestimation was most likely due to the fact that the magnetic polarity of the CME was not conducive to producing large geomagnetic storms (small southward component of the magnetic field).

To support this theory, the CME's magnetic field orientation at the L_1 Lagrangian point was analyzed using ACE data. The magnetic field components and magnitude, the maximum K_p calculation from the *Newell et al.* [2007] maximum K_p formula assuming the magnetic field was completely southward, the maximum K_p calculation from the *Newell et al.* [2007] maximum K_p formula taking the clock-angle into account, and the actual maximum K_p are all displayed in Figures 33 to 35 for events 1, 9, and 14 (3 May 1999, 17 Nov 2001, and 3 Dec 2004 CMEs), respectively.

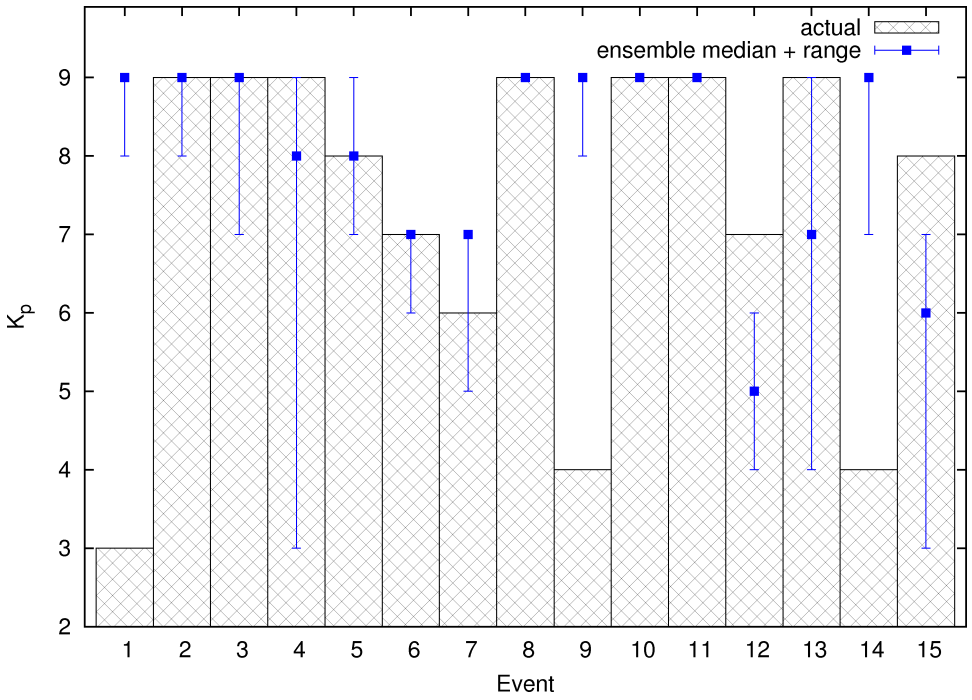

Figure 31. The median and range of the ensemble maximum K_p index along with the actual maximum K_p, per event, using Coned Model version 1.2.

The importance of the magnetic field orientation is obvious from Figures 33 to 35. For event 9, the maximum K_p calculated from ACE data was 8 for the completely southward magnetic field assumption, and was 4 when the clock-angle was taken into account. For event 14, the maximum K_p calculated from ACE data was 9 for the completely southward magnetic field assumption, and was 5 when the clock-angle was taken into account. This highlights the importance of the orientation of the magnetic field on the impact of a CME on the magnetosphere, where the maximum K_p estimates taking the clock-angle into account were around 1/2 of the completely southward magnetic field estimates. The worst-case maximum K_p forecasts were similar to the ACE data calculations with the assumption that the magnetic field was completely southward.

For event 1, the maximum K_p calculated from ACE data was 5 for the completely southward assumption, and was 3 when the clock-angle was taken into account. Since

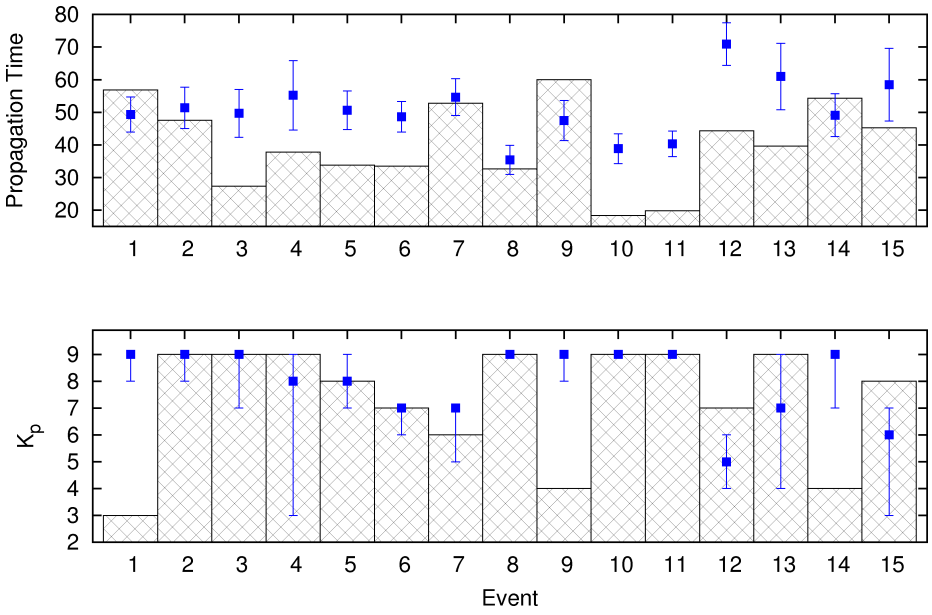

Figure 32. The propagation time and maximum K_p forecasts per event using Coned Model version 1.2. In this figure, the points and error bars are the ensemble forecasts and standard deviations, and the bars are the actual values.

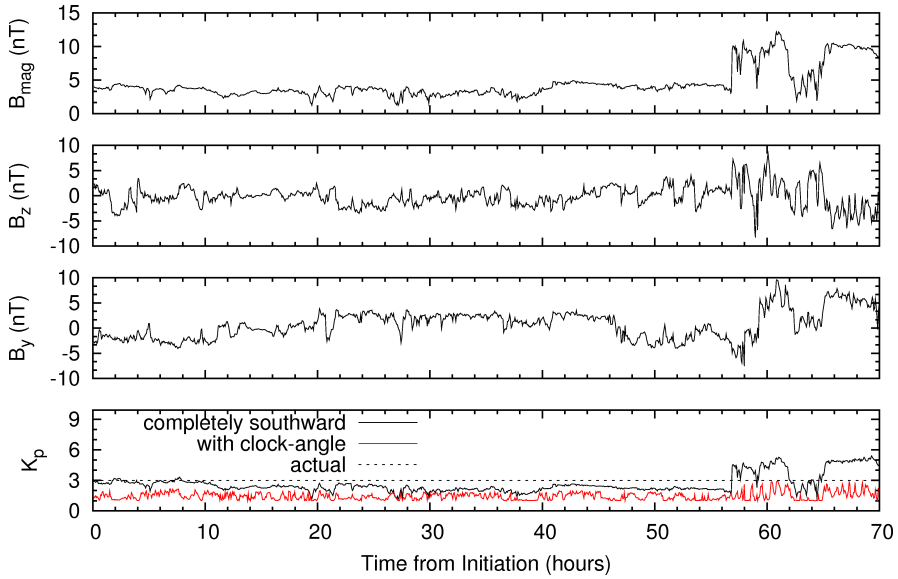

Figure 33. The magnetic field magnitude and components, y component of the magnetic field, z component of the magnetic field, maximum K_p calculation from the *Newell et al.* [2007] maximum K_p formula assuming the magnetic field was completely southward, maximum K_p calculation from the *Newell et al.* [2007] maximum K_p formula taking the clock-angle into account, and the actual maximum K_p for event 1 (3 May 1999 CME) derived from ACE data.

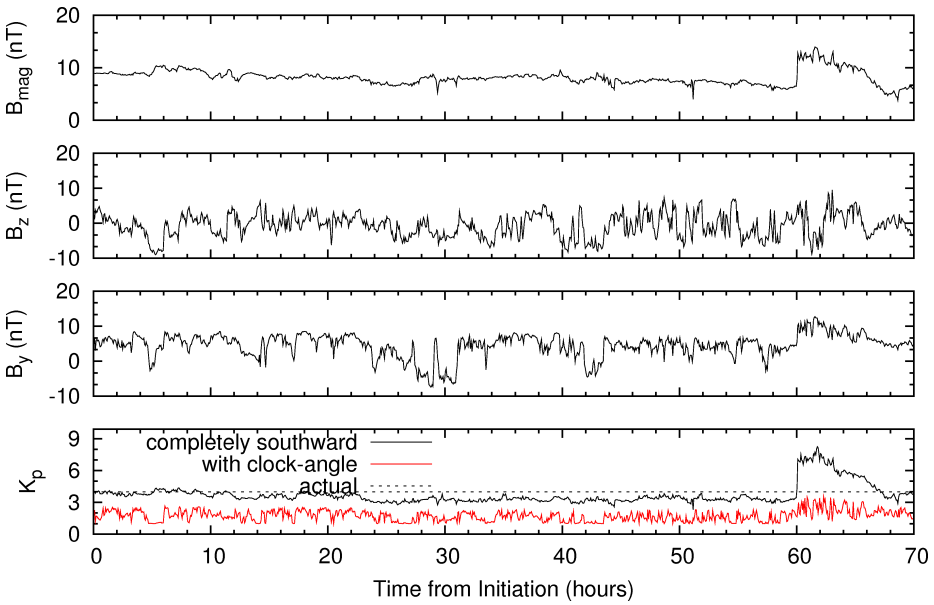

Figure 34. The magnetic field magnitude, y component of the magnetic field, z component of the magnetic field, maximum K_p calculation from the *Newell et al.* [2007] maximum K_p formula assuming the magnetic field was completely southward, maximum K_p calculation from the *Newell et al.* [2007] maximum K_p formula taking the clock-angle into account, and the actual maximum K_p for event 9 (17 Nov 2001 CME) derived from ACE data.

the CME velocity was only slightly overestimated by the ensemble forecast, the magnetic field magnitude predicted by the ensemble forecast must have also been overestimated to produce a maximum K_p forecast of 9. This was the case, where the maximum magnetic field magnitude from ACE was around 12 nT while the maximum magnetic field magnitude from the ensemble forecasting was around 18 nT. This overestimation of the magnetic field magnitude, combined with the slight overestimation of the velocity, produced an overestimated maximum K_p forecast.

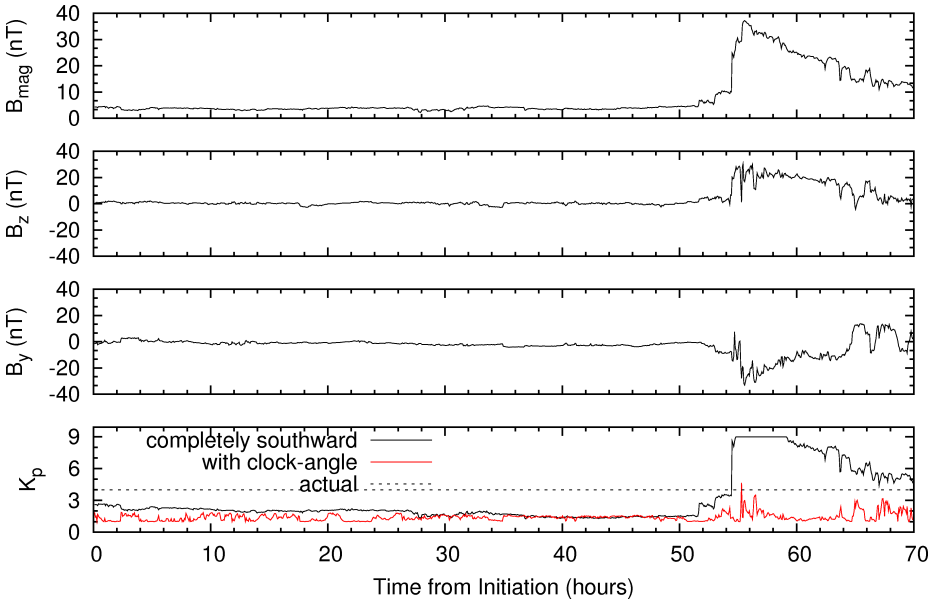

Figure 35. The magnetic field magnitude, y component of the magnetic field, z component of the magnetic field, maximum K_p calculation from the *Newell et al.* [2007] maximum K_p formula assuming the magnetic field was completely southward, maximum K_p calculation from the *Newell et al.* [2007] maximum K_p formula taking the clock-angle into account, and the actual maximum K_p for event 14 (3 Dec 2004 CME) derived from ACE data.

4.2.3 Comparison of Coned Model Versions

The latitude and longitude ensembles were very similar for both versions of the Coned Model (Figure 36). The velocities from Coned Model version 1.3 were around 500 km/s greater than the velocities from Coned Model version 1.2, and the angular widths from version 1.3 were around 20° greater than the widths from version 1.2. The increase in the velocity and width estimations, due to the modification of the optimization routine added to Coned Model version 1.3, were apparent from this analysis.

The propagation time mean absolute forecast error, for all 15 CMEs, was 13.8 *hours* for Coned Model version 1.2, and was 9.1 *hours* for Coned Model version 1.3. This produced a skill score of 0.35 for Coned Model version 1.3 versus version 1.2, which indicated that version 1.3 was more accurate overall. Coned Model version 1.2

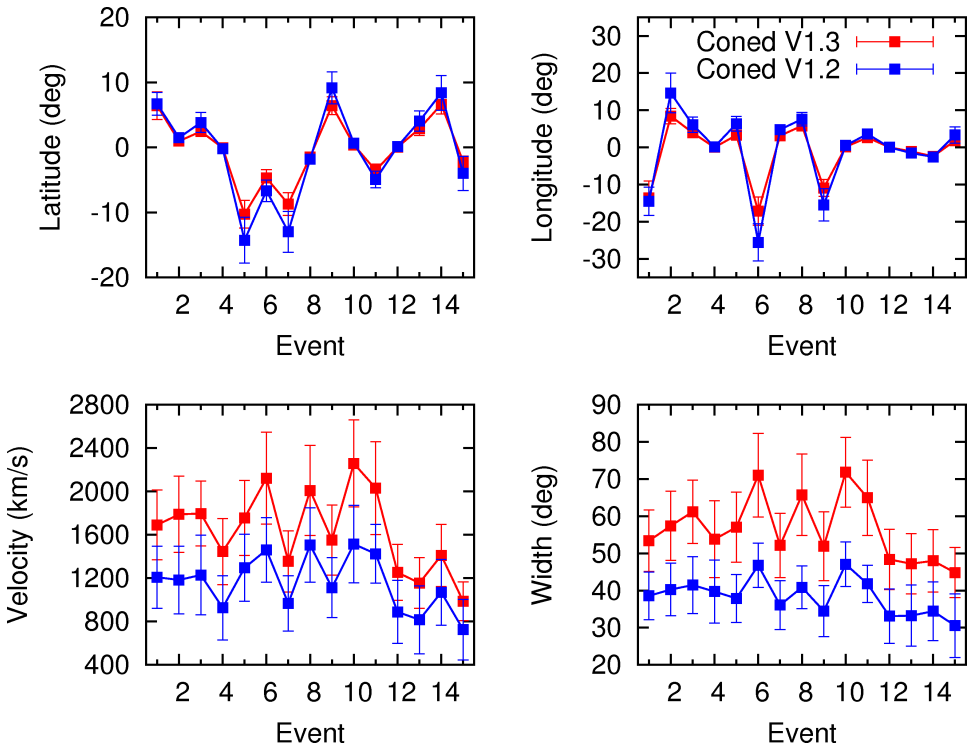

Figure 36. The averages and standard deviations of the input parameter distributions for the 15 CMEs, using Coned Model versions 1.2 and 1.3.

was more accurate for the slower CMEs with actual propagation times greater than 46 *hours*, while Coned Model version 1.3 was more accurate for faster CMEs with actual propagation times less than 46 *hours* (Figures 37 and 38). This was due to the fact that Coned Model version 1.3 was created to produce greater velocities than Coned Model version 1.2.

For the events with actual propagation times less than 46 *hours*, the skill score for Coned Model version 1.3 versus Coned Model version 1.2 was 0.72. This indicated that version 1.3 was much more accurate than version 1.2 for the faster CMEs with actual propagation times less than 46 *hours*. For these events, the mean absolute forecast error for version 1.2 was 17.7 *hours* with a standard deviation of 6.5 *hours*, and the mean absolute forecast error for version 1.3 was 5.0 *hours* with a standard deviation of 3.0 *hours*.

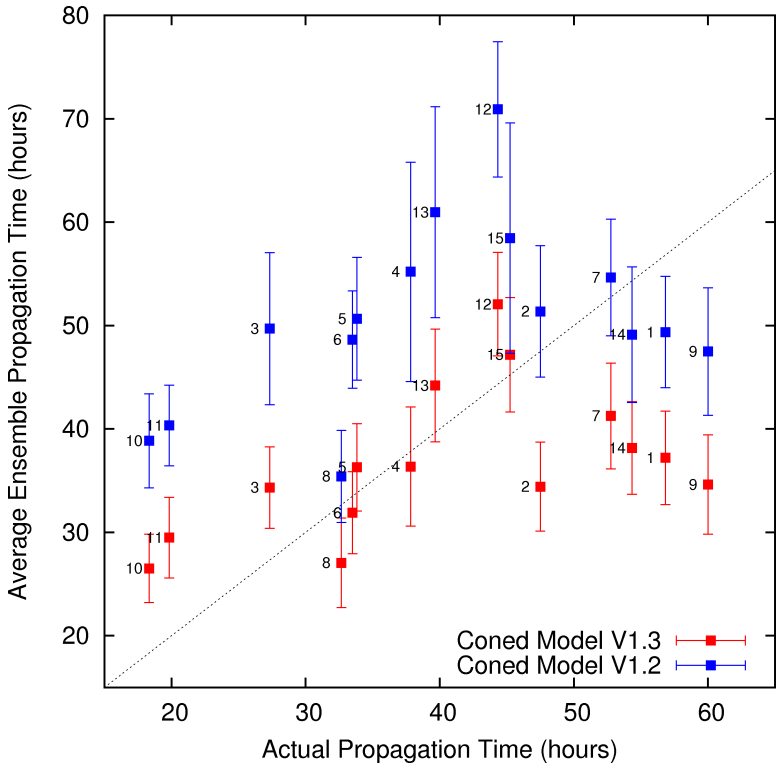

Figure 37. The average ensemble propagation time versus the actual propagation time for the 15 CMEs, using Coned Model versions 1.2 and 1.3. In this figure, the error bars are the standard deviations, and the labels are the event numbers.

For the events with actual propagation times greater than 46 *hours*, the skill score for Coned Model version 1.3 versus Coned Model version 1.2 was -1.77, which indicated that version 1.2 was much more accurate for the slower CMEs with actual propagation times greater than 46 *hours*. For these events, the mean absolute forecast error for version 1.2 was 6.2 *hours* with a standard deviation of 4.1 *hours*, and the mean absolute forecast error for version 1.3 was 17.1 *hours* with a standard deviation of 5.6 *hours*.

The maximum K_p mean absolute forecast error, for all 15 events, was 1.66 for Coned Model version 1.3, and was 1.60 for Coned Model version 1.2. This produced a skill score of -0.04 for version 1.3 versus version 1.2, which indicated that version 1.2 was slightly more accurate, overall (Figure 39). The magnetic field estimations

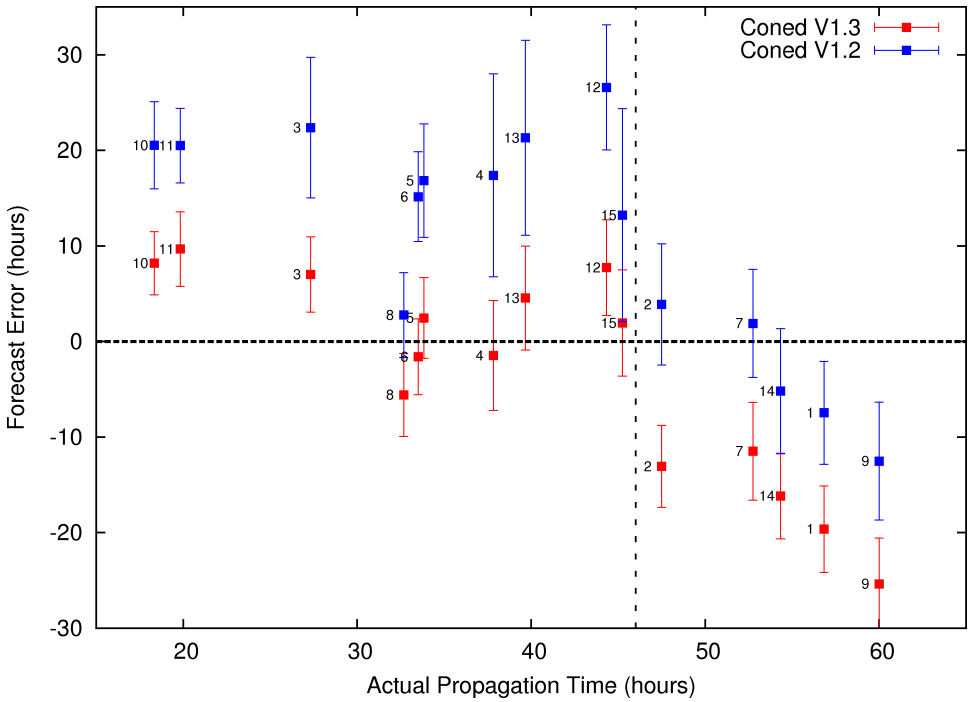

Figure 38. The propagation time forecast error versus the actual propagation time for the 15 CMEs, using Coned Model versions 1.2 and 1.3. The dashed vertical line represents the 46 *hours* point where Coned Model version 1.2 becomes more accurate than Coned Model version 1.3. The error bars are the standard deviations, and the labels are the event numbers.

were similar for both versions of the Coned Model, so the decreased maximum K_p estimates for version 1.2 were due to the decreased velocity estimations.

For the events with actual maximum K_p indices of 9, the mean absolute forecast error for version 1.2 was 0.43 with a standard deviation of 0.79, and was zero for version 1.3. This indicated that Coned Model version 1.3 was more accurate than version 1.2 in forecasting the maximum K_p indices for events with actual maximum K_p indices of 9. For the events with actual maximum K_p indices less than 9, the mean absolute forecast error for version 1.2 was 2.63 with a standard deviation of 2.39, and for version 1.3 was 3.13 with a standard deviation of 1.96. This provided a skill score of 0.16 for version 1.2 versus version 1.3, which indicated that version 1.2 provided more accurate forecasts for events with actual maximum K_p indices less than 9.

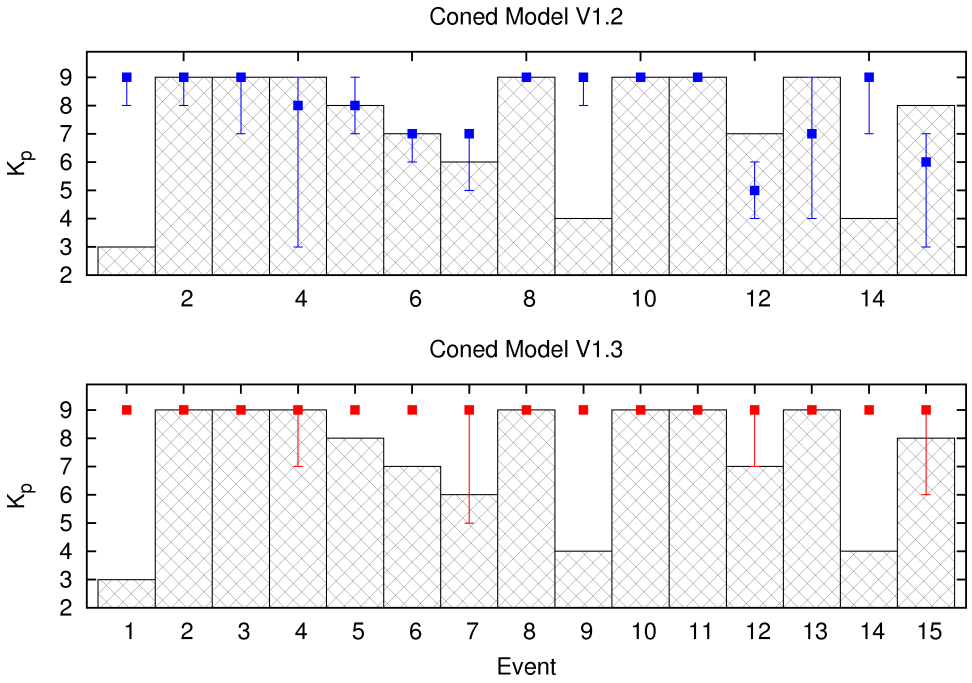

Figure 39. The medians and ranges of the maximum K_p index ensembles along with the actual maximum K_p indices, per event, using Coned Model versions 1.2 and 1.3. The blue and red points and error bars represent the medians and ranges of the ensemble forecasts, while the bars represent the actual values.

4.3 Propagation Time Error Analysis

In an attempt to find the CMEs with large negative forecast errors (slower CMEs with forecast errors less than -10 *hours*) from Coned Model version 1.3, based only on the information available at the time of the CME eruption (including flare location, LASCO POS velocity, type II speeds, and the Coned Model parameters derived from LASCO images), the forecast error was plotted against the different parameters to see if any patterns developed. No apparent pattern was obvious from the associated flare location (Figure 40). The flare locations were spread over all of the quadrants except the South-West quadrant, which was due to the events selected for this study.

There was no apparent pattern based on the Coned Model average latitude and longitude (Figure 41). Three of the five CMEs with large negative forecast errors

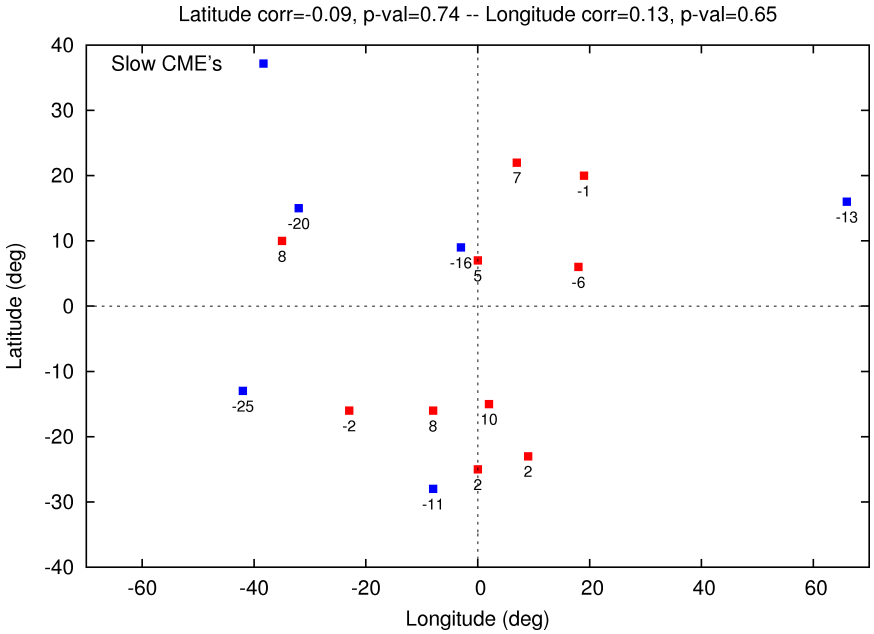

Figure 40. The associated solar flare latitude and longitude of the 15 CMEs with the forecast errors as the labels. The blue points are the slower CMEs with forecast errors less than -10 *hours*.

were located in the North-East quadrant. The other two CMEs with large negative forecast errors were located in the North-West and South-West quadrants.

No pattern was apparent from the Coned Model average angular width (Figure 42). The five events with large negative forecast errors were all found between 45° and 60°, but there were also a number of other events found in that same region that did not have large negative forecast errors.

No clear pattern was apparent from the Coned Model average velocity (Figure 43). The five events with large negative forecast errors were all found between 1300 km/s and 1800 km/s, but a couple of events without large negative errors were also found in this region.

A pattern was apparent from the LASCO POS first-order velocity, with the five events with the large negative forecast errors as the only events located between 950 km/s to 1600 km/s (Figure 44). While this pattern works for the 15 events in

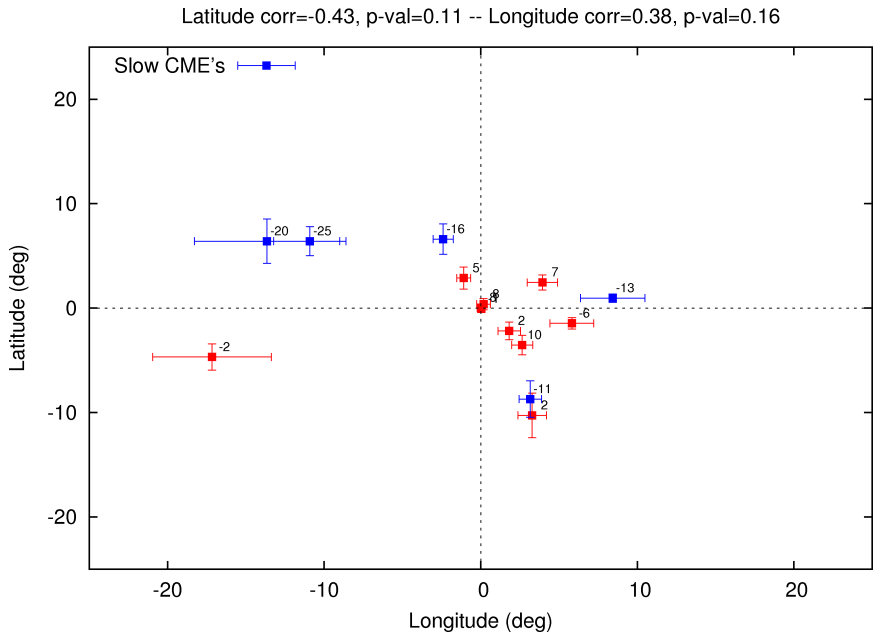

Figure 41. The Coned Model average latitude and longitude of the 15 CMEs with the forecast errors as the labels. The blue points are the slower CMEs with forecast errors less than -10 *hours*. The error bars are the standard deviations of the ensembles.

this analysis, it does not hold true for all CMEs. This became apparent with the application of the generalized linear model to the four test CMEs (see Section 4.3.1 for more detail). If more events were analyzed, this pattern would disappear.

Not all of the events had type II data available, so only four of the five events with large negative errors are displayed in Figure 45. The four events with large negative forecast errors all had type II speed of less than 800 km/s. A couple of other events were also found in this region, which indicated that no clear pattern was available from the type II speed.

While no clear pattern was available from the input parameters by themselves, a generalized linear model (GLM) was employed to determine if some combination of the parameters could be used to locate the events with large negative forecast errors based solely on information available at the time of the CME eruption (before the CME arrived at Earth).

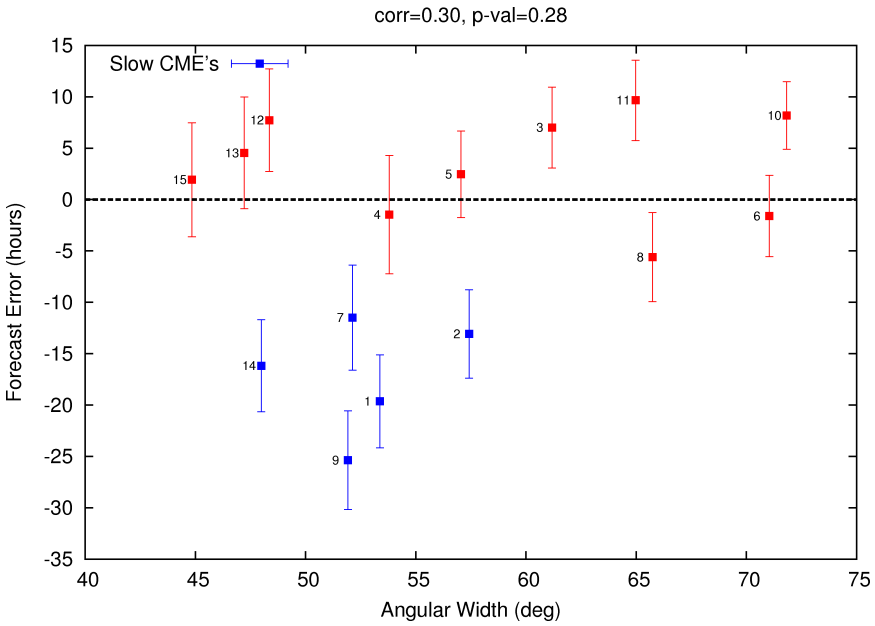

Figure 42. The propagation time forecast error versus the Coned Model average angular width, with the event numbers as the labels. The blue points are the slower CMEs with forecast errors less than -10 *hours*. The error bars are the standard deviations of the ensembles.

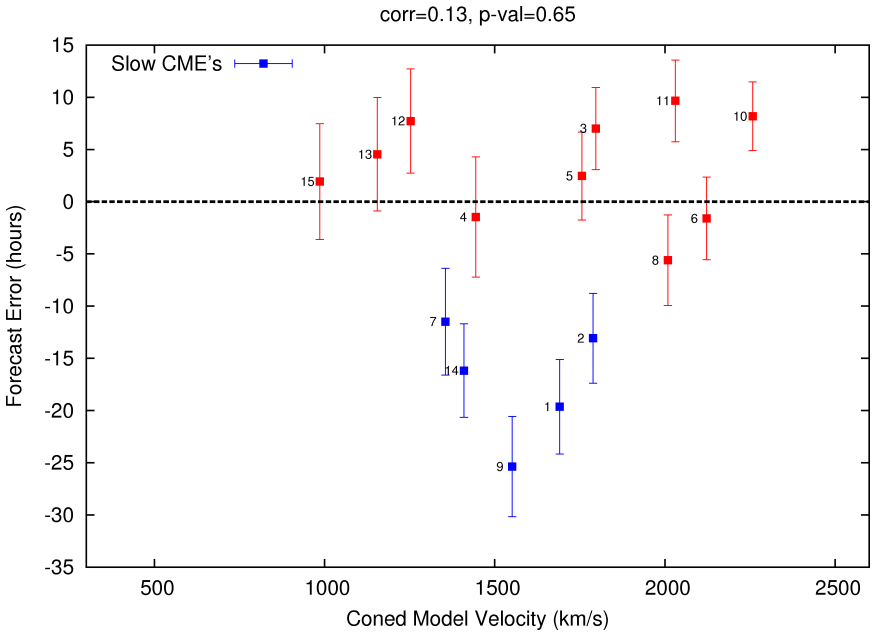

Figure 43. The propagation time forecast error versus the Coned Model average velocity, with the event numbers as the labels. The blue points are the slower CMEs with forecast errors less than -10 *hours*. The error bars are the standard deviations of the ensembles.

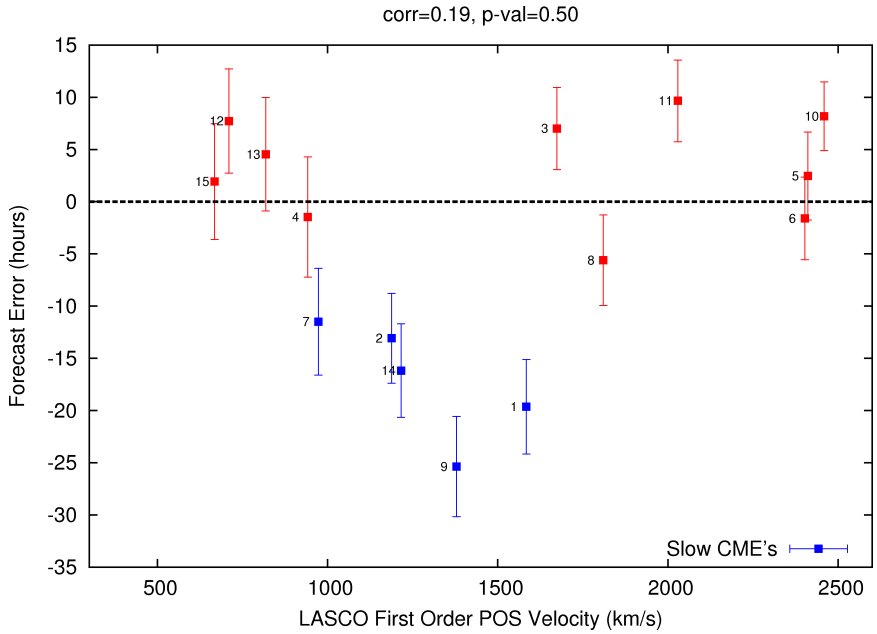

Figure 44. The propagation time forecast error versus the LASCO POS first order velocity, with the event numbers as the labels. The blue points are the slower CMEs with forecast errors less than -10 *hours*. The error bars are the standard deviations of the ensembles.

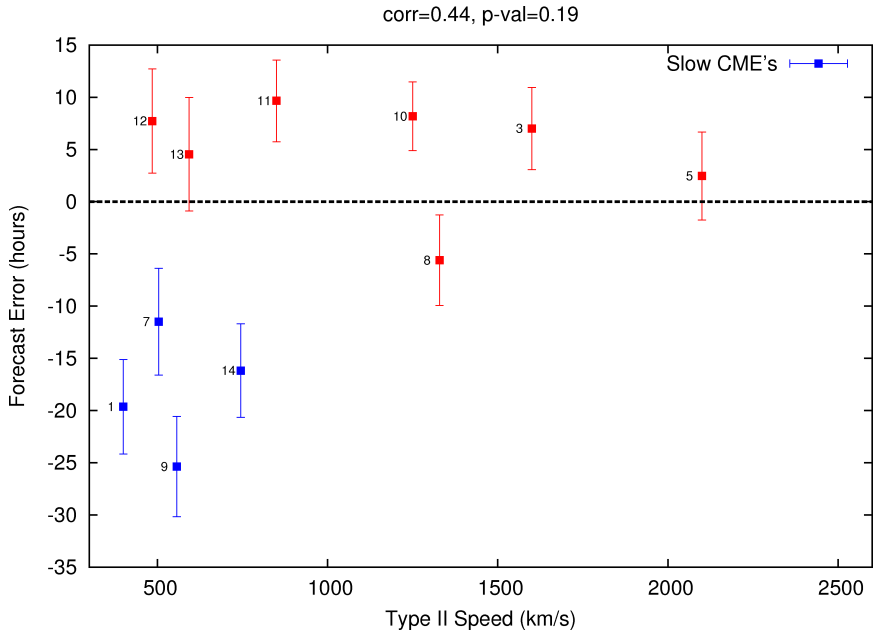

Figure 45. The propagation time forecast error versus the type II speed, with the event numbers as the labels. The blue points are the slower CMEs with forecast errors less than -10 *hours*. The error bars are the standard deviations of the ensembles.

4.3.1 Generalized Linear Model

The GLM was created and employed with a variety of predictor sets. For each set of predictors, a different set of predictor coefficients was calculated by logistic regression. A perfect GLM model would predict a probability of Coned Model version 1.2 providing a more accurate forecast than Coned Model version 1.3 (the need to use version 1.2) as one for all CMEs with a forecast error less than -10 $hours$, and zero for all other CMEs.

For the predictor set of only the cone parameters, the GLM was calculated to be

$$\log\left(\frac{p}{1-p}\right) \approx 23.77 + 0.01ConedLat + 0.02ConedLong \\ +0.02ConedV - 0.98ConedW \tag{32}$$

where $ConedLat$ is the average of the Coned Model version 1.3 latitude ensemble in deg, $ConedLong$ is the average of the Coned Model version 1.3 longitude ensemble in deg, $ConedV$ is the average of the Coned Model version 1.3 velocity ensemble in km/s, and $ConedW$ is the average of the Coned Model version 1.3 angular width ensemble in deg. Of the 5 CMEs with forecast errors less than -10 $hours$, 4 had a probability over 0.5, which indicated that Coned Model version 1.2 should be used. Of the 10 CMEs with forecast errors greater than -10 $hours$, only 1 had a probability greater than 0.5. Therefore, the GLM using only the Coned Model parameters as the predictor set, when applied to the 15 CMEs used to create the GLM, predicted 13 of the 15 events correctly (Table 21).

For the predictor set composed of the non-cone parameters (flare location, kinematic LASCO first order POS velocity, and type II speed), the GLM was calculated

Table 21. Results for the Generalized Linear Model applied to the 15 CMEs of this analysis, using a binomial distribution and logit link function with the Coned Model parameters as the predictor set.

forecast error (hours)	CME date (YYYYMMDD)	probability of V1.2 more accurate than V1.3
-24.77	20011117	0.8054
-19.72	19990503	0.9266
-16.17	20041203	0.9430
-13.08	20000404	0.6713
-11.49	20011009	0.0877
-2.91	20011104	0.0304
-1.60	20010924	0.0009
-0.23	20010329	0.0922
1.82	20100403	0.1215
2.46	20010410	0.5593
4.86	20041106	0.2364
6.93	20000714	0.0522
7.73	20040720	0.3812
8.48	20031028	0.0073
10.21	20031029	0.0846

to be

$$\log\left(\frac{p}{1-p}\right) \approx 3.24 - 0.05FlareLat - 0.32FlareLong \\ -0.01LASCOV + 0.01TypeII \tag{33}$$

where $FlareLat$ is the associated solar flare latitude in deg, $FlareLong$ is the associated flare longitude in deg, $LASCOV$ is the kinematic first-order velocity derived from LASCO imagery in km/s, and $TypeII$ is the type II speed in km/s. The GLM predicted the need to use Coned Model version 1.2 correctly for 3 of the 5 events with large negative errors. One of the 5 events with large negative forecast errors was unable to be predicted due to the fact that it was missing type II data. The GLM also predicted that 1 of the 10 events with forecast errors greater than -10 $hours$ should

use Coned Model version 1.2, which was incorrect. This predictor set predicted 9 of the 11 events with type II data available correctly (Table 22). The 4 events with missing type II data highlight the difficulty of using a GLM, which cannot make a prediction if data for one of the parameters is missing.

Table 22. Results for the Generalized Linear Model applied to the 15 CMEs of this analysis, using a binomial distribution and logit link function with the non-cone parameters (flare location, LASCO POS first order velocity, and type II speed) as the predictor set. The entries with the dashed lines indicate the events which had no type II data available.

forecast error (hours)	CME date (YYYYMMDD)	probability of V1.2 more accurate than V1.3
-24.77	20011117	1.0000
-19.63	19990503	0.9458
-16.17	20041203	0.2807
-13.08	20000404	–
-11.49	20011009	0.9510
-2.91	20011104	0.0002
-1.60	20010924	–
-1.47	20010329	–
1.93	20100403	–
2.46	20010410	0.0286
4.86	20041106	0.5843
7.01	20000714	0.0583
7.73	20040720	0.1390
8.48	20031028	0.0112
10.20	20031029	0.0009

For the predictor set as the combination of cone parameters and non-cone param-

eters, the GLM was calculated to be

$$\log\left(\frac{p}{1-p}\right) \approx 993.31 - 7.53ConedLat + 18.53ConedLong \\ +1.27ConedV - 48.94ConedW + 1.06SolarLat \\ -7.42SolarLong - 0.25LASCOV + 0.01TypeII. \tag{34}$$

For the events with type II data available, the GLM predictions were perfect when applied to the 15 CMEs of this analysis (Table 23).

Table 23. Results for the Generalized Linear Model applied to the 15 CMEs of this analysis, using a binomial distribution and logit link function with a combination of the cone parameters and non-cone parameters as the predictor set. The entries with the dashed lines indicate the events which had no type II data available.

forecast error (hours)	**CME date (YYYYMMDD)**	**probability of V1.2 more accurate than V1.3**
-24.77	20011117	1.0000
-19.72	19990503	1.0000
-16.17	20041203	1.0000
-13.08	20000404	–
-11.49	20011009	1.0000
-2.91	20011104	0.0000
-1.60	20010924	–
-0.30	20010329	–
1.93	20100403	–
2.46	20010410	0.0000
4.86	20041106	0.0000
6.93	20000714	0.0000
7.73	20040720	0.0000
8.48	20031028	0.0000
10.20	20031029	0.0000

The GLM did not perform well when applied to the 4 test CMEs (Table 24). Based on the comparison of the ensemble forecast results using both versions of the Coned

Model, it was assumed that the CMEs with actual propagation times greater than 50 *hours* should use Coned Model version 1.2 while the CMEs with actual propagation times less than 40 *hours* should use Coned Model version 1.3. With this assumption in place, the GLM with the variety of predictor sets, could not predict the correct version of the Coned Model to use for all of the test CMEs.

Table 24. Probabilities that Coned Model version 1.2 would provide a more accurate forecast than Coned Model version 1.3, using a generalized linear model with a variety of predictor sets, applied to 4 test CMEs with a variety of actual propagation times.

test CME date (YYYYMMDD)	actual propagation time (hours)	probability of V1.2 more accurate than V1.3 with the cone parameters as predictors	probability of V1.2 more accurate than V1.3 with the non-cone parameters as predictors	probability of V1.2 more accurate than V1.3 with all parameters as predictors	assumed actual probability
20020824	57	0.71	0.00	0.00	1.00
20020816	53	0.03	1.00	0.00	1.00
20040725	31	0.33	0.00	0.00	0.00
20061213	35	1.00	0.00	1.00	0.00

The GLM using the cone parameters as the predictor set predicted 2 out of the 4 test events correctly. The GLM using the non-cone parameters as the predictor set predicted 3 of the 4 test events correctly. The GLM using the combination of cone parameters and non-cone parameters as the predictor set predicted 1 of the 4 test events correctly. While the predictor set of the combination of the cone parameters and non-cone parameters performed perfectly for the 15 CMEs of this analysis (with type II data available), it performed very poorly when applied to the test CMEs. Out of the 3 predictor sets, the set with the input parameters not derived from the Coned Model (non-cone parameters) performed the best when applied to CMEs outside of the CMEs used to form the GLM.

Overall, the GLM could not perfectly predict the correct version of the Coned Model to use when applied to CMEs outside of the 15 CMEs used to create the

GLM, and should not be used as an operational tool to determine which version of the Coned Model to use. The poor performance of the GLM most likely stems from the fact that only 15 data points were used to create the GLM, which is a very small number of points to build a statistical model. The GLM may become more accurate if enough data points are collected to meet the 10 events per predictive variable suggested by *Peduzzi et al.* [1996], assuming that a meaningful relationship between the input variables and the forecast error using Coned Model version 1.3 exists in the first place.

4.4 Model Robustness

4.4.1 Varying the Magnetic Field Scaling Factor

The magnetic field scaling factor adjusts the magnitude of the radial magnetic field near Earth. A change of magnetic field magnitude by a factor of $2.5/4.0 \approx 0.63$ would be expected for a change of the magnetic field scaling factor from 4.0 to 2.5. The maximum K_p formula developed by *Newell et al.* [2007] contains a factor of $B_t^{2/3}$, so a change in the magnetic field magnitude by a factor of 2.5/4.0 should produce a change in the maximum K_p index by a factor of $(2.5/4.0)^{2/3} \approx 0.73$.

Overall, changing the magnetic field scaling factor from 4.0 to 2.5 had a small effect on the ensemble forecasts, but it did change the minimum maximum K_p index predicted for 3 of the 11 events analyzed. The maximum change in the propagation time forecast was calculated to be 1.2 *hours*, for event 4 (Figure 46). This was a change of 3.4% with respect to the propagation time forecast using a magnetic field scaling factor of 2.5. The maximum change in the propagation time standard deviation was 0.2 *hours*, for event 13. This was a 3.5% change with respect to the standard deviation for event 13 using a magnetic field scaling factor of 2.5. The maximum change in the propagation time range was 5.0 *hours*, for event 4. This was

a noticeable change of 16.5% with respect to the range for event 4 using a magnetic field scaling factor of 2.5.

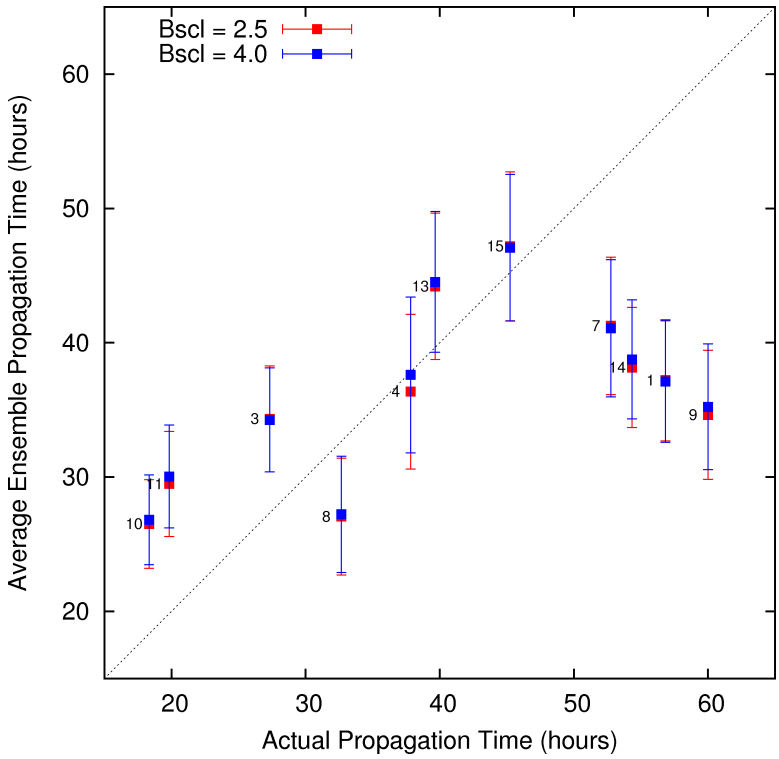

Figure 46. The averages and standard deviations of the propagation time ensembles versus the actual propagation times for the magnetic field scaling factor set at 2.5 and 4.0. The labels are the event numbers, and the error bars are the standard deviations.

With respect to the maximum K_p index ensembles, changing the scaling factor from 4.0 to 2.5 had no effect on the median values of the ensembles, but did change the minimum values for 3 of the ensembles (Figure 47). Both sets of forecasts predict a maximum K_p of 9 for all events, but the minimum values for events 4, 7, and 15 were lower using the magnetic field scaling factor of 2.5 than using 4.0. This was due to the lowering in the maximum K_p estimates from the lowering in the magnetic field magnitude estimates. The minimum value for event 15 went from 8 for the magnetic field scaling factor of 4.0 to 6 for the magnetic field scaling factor of 2.5, which was

lower by a ratio of 0.77. This was close to the expected lowering ratio of 0.73.

The maximum change in the range of predicted maximum K_p indices was 2, for both events 4 and 15. This was a 100% change for event 4, with respect to the range calculated using the magnetic field scaling factor of 2.5. 3 events had non-zero uncertainties using the magnetic field scaling factor of 2.5, while only 2 events had non-zero uncertainties using the magnetic field scaling factor of 4.0.

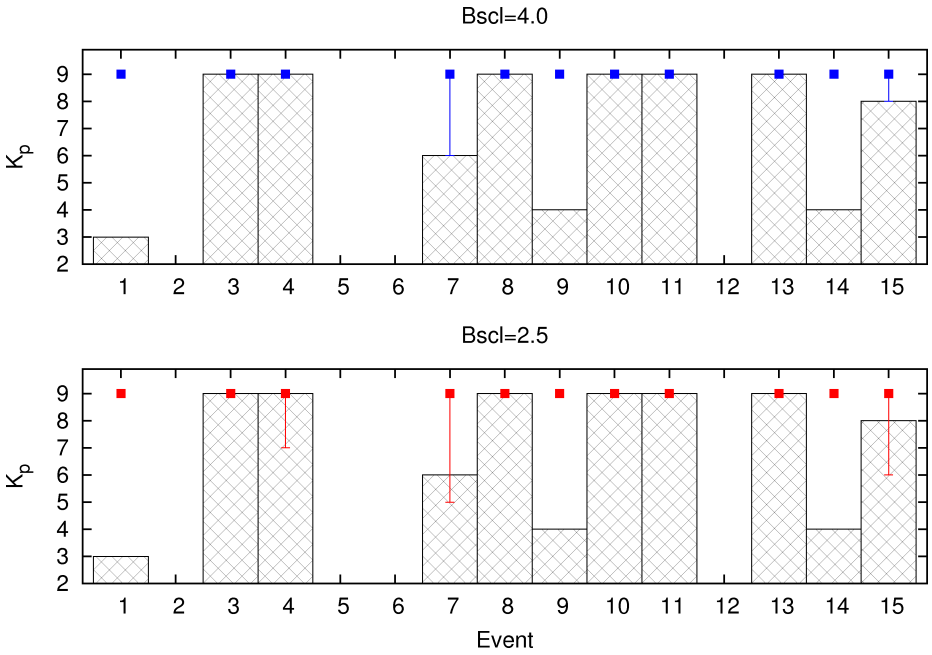

Figure 47. The medians and ranges of the maximum K_p index ensembles along with the actual maximum K_p, per event, for the magnetic field scaling factor set at 2.5 and 4.0. The points with errobars are the ensemble forecasts and the bars are the actual values.

The velocity, magnetic field, and calculated maximum K_p for the 3 Apr 2010 CME (event 15) using the 2nd set of input parameters are displayed in Figure 48, for both magnetic field scaling factors. Changing the magnetic field factor from 4.0 to 2.5 changed the magnetic field magnitude from 13.2 nT to 9.2 nT, which was a ratio of change of approximately 0.70. This was close to the expected ratio of 0.63. The

velocity experienced a negligible change for the change in the magnetic field scaling factor, which was expected. The un-rounded maximum K_p changed from 8.8 to 7.0 when the magnetic scaling factor was changed from 4.0 to 2.5. The ratio of change for the maximum K_p was approximately 0.80, which was close to the expected ratio of 0.73.

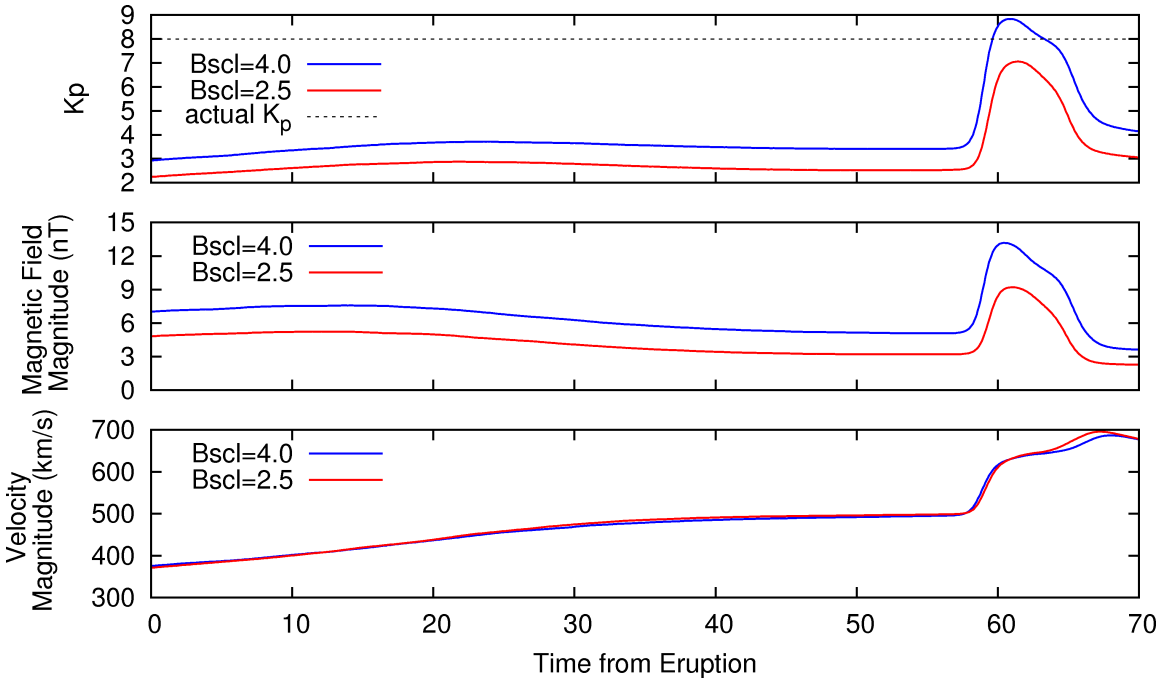

Figure 48. The velocity, magnetic field, and calculated maximum K_p for the 3 Apr 2010 CME, at Earth, using magnetic scaling factors of 4.0 and 2.5. The velocity and magnetic field were the results from ENLIL for the 2nd set of input parameters for this event.

4.4.2 Varying Ensemble Size

The ensemble size was varied to analyze the effect of the ensemble size on the ensemble forecast, and to test the robustness of the ensemble forecast using the WSA-ENLIL with Coned Model. The 29 Oct 2001 CME (event 4) was used as the test case due to the fact that the propagation time forecast was the most accurate of the 15

CMEs. The magnetic field scaling factor was held at 4.0 while the ensemble size was varied. Overall, varying the ensemble size did not have a large effect on the ensemble forecasts.

The maximum change in the average velocity, due to varying the ensemble size, was 62.8 km/s (Figure 49). This was a 4% change relative to the average velocity of 1444.3 km/s for the ensemble size of 100. The maximum change in the standard deviation was 53.1 km/s, which was a relative change of 17% with respect to the standard deviation of 304.9 km/s for the ensemble size of 100. The maximum change in the range of the velocity was 411.0 km/s, which was a 29% shift from the velocity range of 1408.0 km/s for the ensemble size of 100. While the average velocity experienced a relatively small change, the uncertainty of the velocity ensemble (standard deviation and range) experienced a significant change for the different ensemble sizes.

The maximum change in the average width was 2.6°, which was a relative change of 5% compared to the average width of 53.8° for the ensemble size of 100. The maximum change in the standard deviation was 2.8°, which was a relative change of 27% relative to the standard deviation of 10.3° for the ensemble size of 100. The maximum change in the range of the width was 17.0°, which was a relative change of 35% with respect to the range of 49.0° for the ensemble size of 100. Similar to the velocity distributions, the average angular width experienced a small change with the different ensemble sizes while the uncertainties experienced significant changes.

While the latitude and longitude ensembles experienced large relative changes since the initial values for the ensemble size of 100 were close to zero, the absolute changes were small. The average latitude changed from $-0.1°$ with an ensemble size of 100 to 0.0° for the smaller ensemble sizes. The standard deviation of the latitude ensembles were all 0.0°. The latitude range was 1.0° for all ensemble sizes except for 25, which had a range of 0.0°. The average longitude was 0.0° for all ensemble sizes,

and the standard deviation and range values were the same as the latitude values.

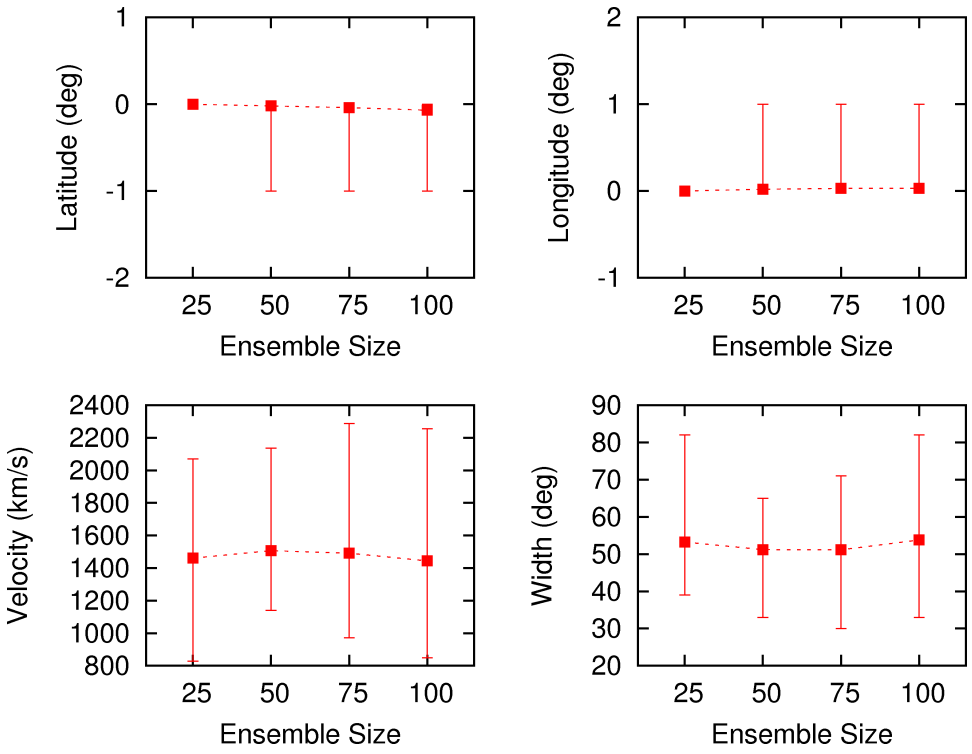

Figure 49. The averages and ranges of the input parameter distributions versus the ensemble size for the 29 Mar 2001 CME.

The average propagation time varied from 37.6 *hours* for the ensemble size of 100 to 35.9 *hours* for the ensemble size of 50 (Figure 50). This change of 1.7 *hours* in the average propagation time was a relatively small change of 4% compared to the 37.6 *hours* predicted for the ensemble size of 100. The standard deviation of the propagation time ensemble varied from 3.9 *hours* for the ensemble size of 50 to 6.0 *hours* for the ensemble size of 25. This was a relatively large change of 36% relative to the standard deviation of 5.8 *hours* for the ensemble size of 100. The range of propagation time ensembles varied from 26.4 *hours* for the ensemble size of 25 to 13.8 *hours* for the ensemble size of 50. This was a relatively large change of 49% relative to the range of 25.5 *hours* for the ensemble size of 100. Similar to

the input parameter distributions, the average propagation time did not experience a large change with the different ensemble sizes, but the uncertainties experienced significant changes.

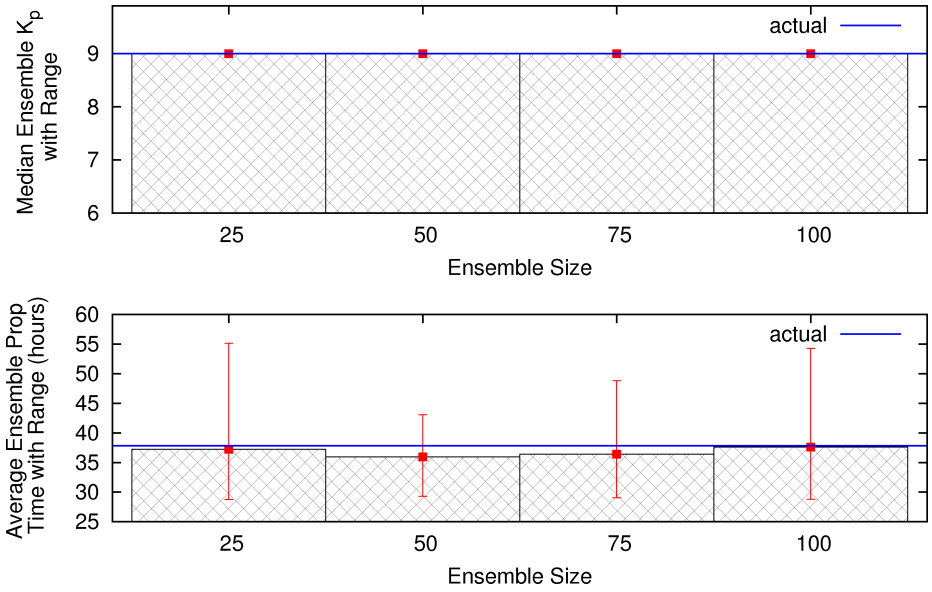

Figure 50. The average and range of propagation times along with the median and range of maximum K_p indices versus the ensemble size for the 29 Mar 2001 CME. The bars and error bars represent the ensemble forecasts and ranges, while the blue horizontal line represents the actual values.

The maximum K_p statistics were the same for all ensemble sizes (Figure 50). This CME caused an actual maximum K_p of 9, and all of the ensemble sizes predicted the correct maximum K_p value.

While the variation of the ensemble size did not affect the accuracy of the predictions by much, it did affect the range of the input parameters and the propagation time. Due to the fact that the bootstrap approach used by the Coned Model randomly selects 300 points to determine the cone parameters, a smaller ensemble size may not properly sample the entire input distribution. The larger the ensemble size, the more the sampling is likely to sample the tails of the distributions, which may not

be sampled by smaller sample sizes. This was apparent in the change of the range of the input parameters and propagation times when changing the ensemble size. Even though the ensemble size of 25 had a range similar to the range of the ensemble size of 100, the ensemble size of 50 had almost half the range of the ensemble size of 100. This indicated that the ensemble size of 50 did not sample the tails of the input distribution, and indicated that a larger ensemble size should be used to ensure the sampling of the input distribution tails. Therefore, the ensemble size of 100 should be used, if possible, to ensure the correct sampling of the tails of the input distributions.

4.4.3 Varying the Magnetogram Source

For the two CMEs analyzed with different magnetogram sources, the propagation time differences were relatively small and the medians of the maximum K_p ensembles did not change at all (Figure 51). The 3 Dec 2004 CME magnetogram source was varied from NSO to Mt Wilson. The 4 Apr 2010 CME magnetogram source was varied from NSO to GONG due to the fact that the Mt Wilson magnetogram data was unreliable for this Carrington rotation. All of the model runs used a magnetic scaling factor of 4.0, unless stated otherwise.

For the 3 Dec 2004 CME, the average ensemble propagation time changed by 0.52 *hours*, which was a negligible change of 1.3% relative to the average ensemble propagation time of 38.76 *hours* using the NSO magnetograms. The standard deviation of the propagation time only changed by 0.02 *hours*, which was a negligible change of 0.4%. The range also experienced a negligible change of 0.13 *hours*, which was a 0.6% change from the range using the NSO magnetograms. The maximum K_p predictions were exactly the same for the both of the magnetogram sources. The change of magnetogram sources from NSO to Mt Wilson had very little effect on the forecast.

For the 3 Apr 2010 CME, the average ensemble propagation time changed by 1.58

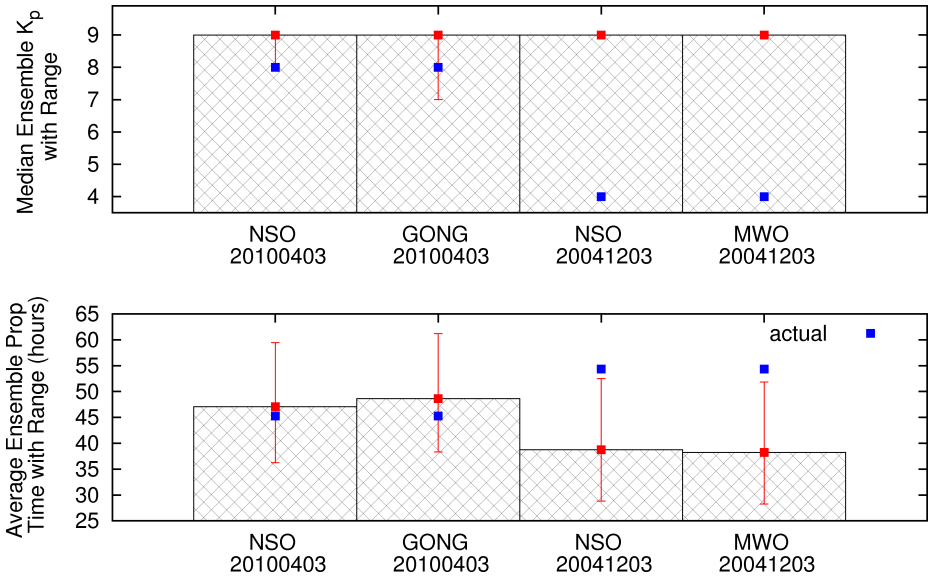

Figure 51. The propagation time and maximum K_p index ensemble forecasts for the 3 April 2010 CME using the NSO and GONG magnetograms, and the 3 Dec 2004 CME using the NSO and Mt Wilson magnetograms. The blue points represent the actual values, while the bars with red points and errobars represent the ensemble forecasts and ranges.

hours, which was a small change of 3.4% relative to the average ensemble propagation time of 47.07 *hours* using the NSO magnetograms. The change in standard deviation and range of propagations times were 0.06 and 0.30 *hours*, respectively, which were both negligible changes of 1.2% and 1.3%, respectively. While the medians of the maximum K_p ensembles were the same using both magnetogram sources, the minimum predicted value went from 8 using the NSO magnetograms to 7 using the GONG magnetograms. This change in the maximum K_p forecast was due to the fact that the different magnetogram sources require different magnetic field scaling factors to correctly scale the magnetic field values to the appropriate levels near Earth. The GONG magnetograms require a magnetic field scaling factor of 4.0, while the NSO magnetograms require magnetic field scaling factors of 2.5. With the magnetic field scaling factor set at 4.0 while using the NSO magnetograms, the magnetic field estimates near Earth were too large, and the maximum K_p forecasts were

overestimated.

Using the correct magnetic scaling factor for the different magnetograms (2.5 for NSO and Mt Wilson, and 4.0 for GONG), the relative changes in the forecasts were slightly less than holding the magnetic scaling factor at 4.0 for all of the magnetograms (Figure 52). The propagation times changed by 3.1% for the 3 Apr 2010 CME, and 0.2% for the 3 Dec 2004 CME. The maximum K_p index forecasts did not change between the different magnetograms, but the minimum value for 3 Apr 2010 was lowered to 6 when using the correct magnetic field scaling factor.

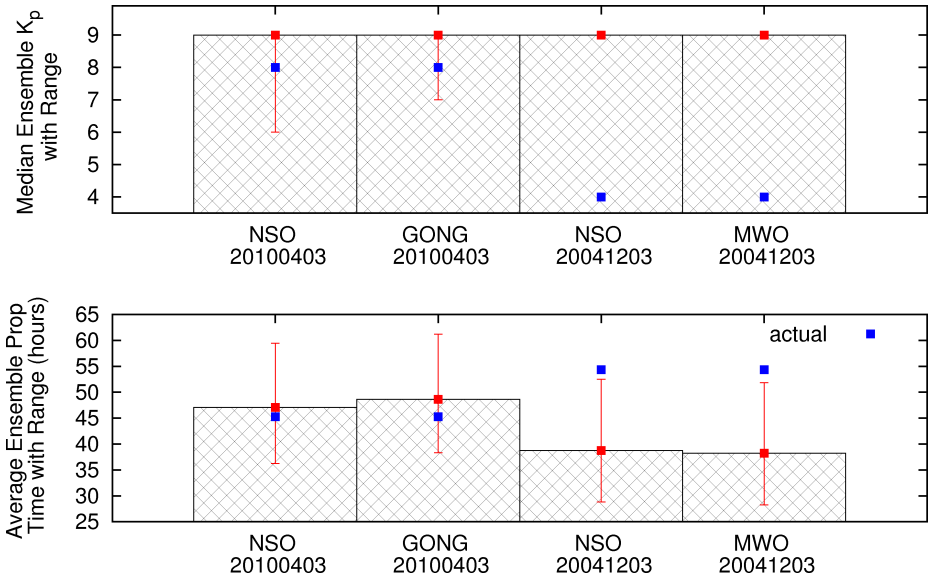

Figure 52. The propagation time and maximum K_p index ensemble forecasts for the 3 April 2010 CME using the NSO and GONG magnetograms, and the 3 Dec 2004 CME using the NSO and Mt Wilson magnetograms. The blue points represent the actual values, while the bars with red points and errobars represent the ensemble forecasts and ranges. In this figure, the Mt Wilson and NSO magnetograms used a magnetic field scaling factor of 2.5 while the GONG magnetograms used a magnetic field scaling factor of 4.0.

Overall, varying the magnetogram source location had a relatively small effect on the ensemble forecast. While the changes in the forecast were small, the change from NSO to GONG appeared to have a slightly larger effect on the forecast than

the change from NSO to Mt Wilson. This indicated that one would obtain similar forecasts using any of the magnetogram sources, and that the ensemble forecast using the WSA-ENLIL with Coned Model is robust with respect to the magnetogram source location.

4.4.4 Varying LASCO Images

Varying the LASCO images used for the Coned Model for the 29 Mar 2001 CME had a relatively small effect on the ensemble forecast. The images used as input for the Coned Model slightly changed the input parameter distributions (Figure 53). The time stamps used for image set one were 20010329114200, 20010329121800, and 20010329124200, while the time stamps used for image set two were 20010329124200, 20010329134200, and 20010329141800. The magnetic field scaling factor was held at 4.0 for the model runs varying the LASCO images used as input to the Coned Model.

The average velocity changed by 56.63 km/s from varying the image set. This was a relatively small change of around 3.9% compared to the average velocity of 1444.26 km/s for the original set of images. The standard deviation of the velocity changed by 3.52 km/s, which was a small change of 1.2% from the standard deviation of 308.40 km/s for the original set of images. The range of velocities changed by 178.00 km/s, which was a noticeable change of 12.6% from the range of 1408.00 km/s for the original set of images.

The average width experienced a negligible change of 0.09° from varying the image set. This was a change of 0.2% from the average width of 53.80° for the original image set. The standard deviation changed by 0.15°, which was a negligible change of 1.5%. The range of widths increased by 5.00° from the range of 49.00° for the original image set, which was a noticeable change of 10.2%.

The average latitude changed by 0.15° from varying the image set. While this was

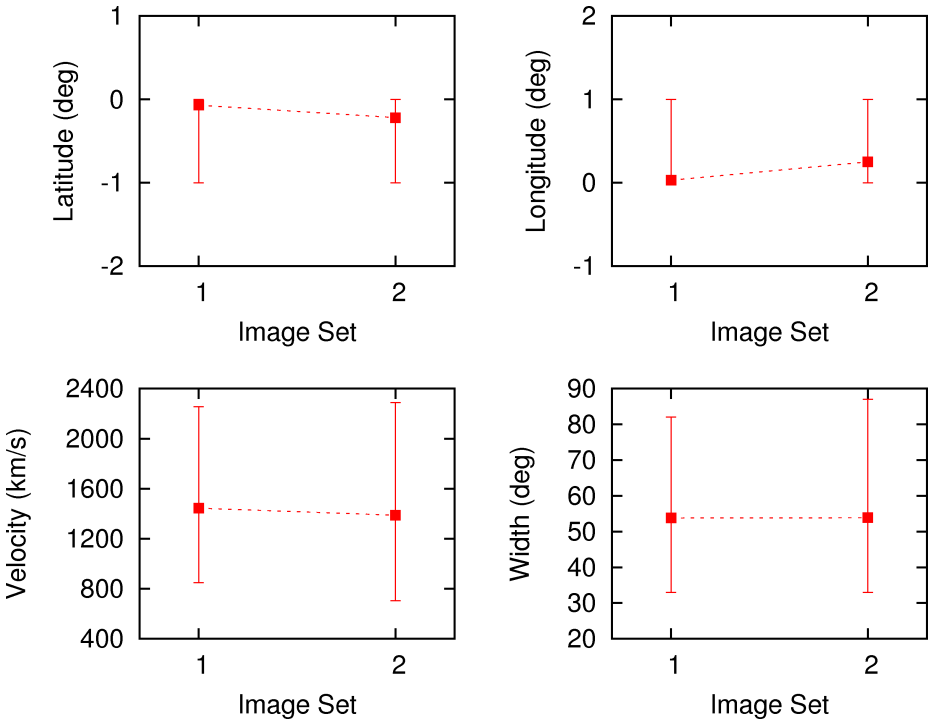

Figure 53. The averages and ranges of the input parameter distributions for the 29 Mar 2001 CME using two different image sets as input for the Coned Model.

a relatively large change from the average latitude of -0.07°, due to the fact that the original average latitude is close to zero, it was a small absolute change of less than one degree. The standard deviation of the latitude changed by 0.16°, which was a small absolute change from 0.26° for the original image set. The range of latitudes did not change while varying the image set.

The average longitude changed by 0.22° from varying the image set. This was also a relatively large change compared to the original average latitude of 0.03°, but it was a small absolute change of less than one degree. The standard deviation changed by 0.26°, which was a small absolute change from 0.17° for the original set of images. The range of longitudes did not change while varying the image set.

Varying the images used for input to the Coned Model had a relatively small effect on the ensemble propagation time (Figure 54). The average propagation time changed

by 1.09 *hours* from varying the image set, which was a relatively small change of 2.9% compared to the average propagation time of 37.6 *hours* for the original set of images. The standard deviation changed from 5.80 *hours* for image set one to 5.95 *hours* for image set two. This was a small change of 2.6%, relative to image set one. The range experienced a noticeable change of 29.0% while varying the image set. The range changed from 25.5 *hours* for the original set of images to 32.9 *hours* for the second set of images. This noticeable change in the range of propagation times was due to the fact that the velocity and width distributions experienced noticeable changes in the ranges.

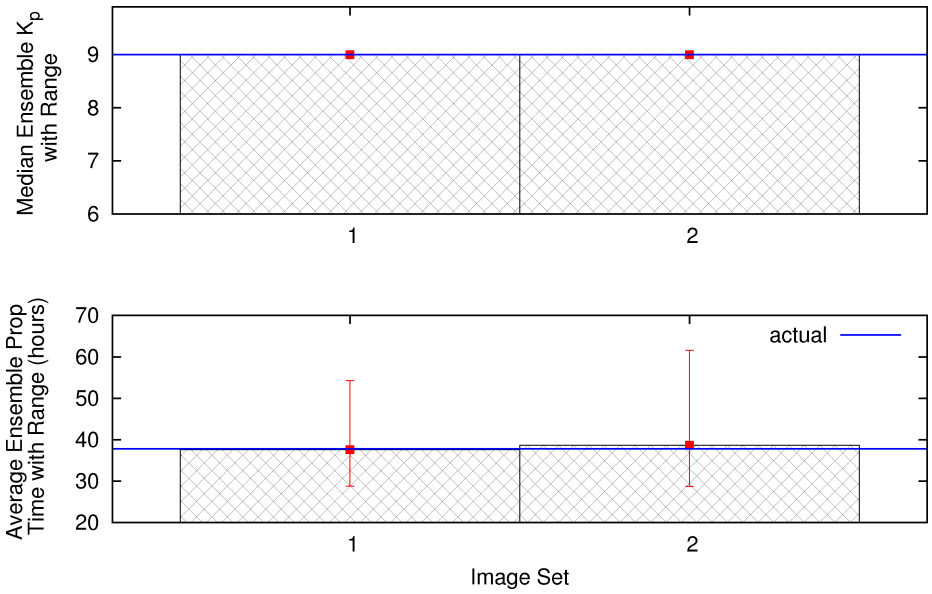

Figure 54. The averages and ranges of the forecast ensembles for the 29 Mar 2001 CME using the two image sets as input for the Coned Model. The blue horizontal line represents the actual values, while the bars with the red points and error bars represent the ensemble forecasts and ranges.

Varying the image sets did not affect the ensemble forecast of the maximum K_p index (Figure 54). Both sets of images forecast the maximum K_p perfectly.

4.5 Flare Location As Propagation Axis

Using the flare location as the propagation axis caused a slight increase in the propagation time forecasts and no change in the maximum K_p index forecasts for 4 of the 5 events analyzed. The event with the associated solar flare location furthest on the solar limb (event 2 with a flare location of N16W66) did not hit Earth when the flare location was used as the propagation axis. The other 4 events displayed a slight change in the propagation times, but the change was small enough that the new propagation times lay within the ensemble averages plus or minus one standard deviation (Table 25 and Figure 55).

Table 25. The propagation time and maximum K_p index forecasts using the associated solar flare location as the propagation axis and the averages of the velocity and width ensembles as the velocities and widths.

event number	ensemble average propagation axis	solar flare location	actual propagation time (hours)	average ensemble propagation time (hours)	propagation time using flare as axis (hours)	actual maximum K_p	median ensemble maximum K_p	maximum K_p using flare as axis
1	N06E14	N15E32	56.83	37.21	37.62	3	9	9
2	N01W08	N16W66	47.50	34.42	missed Earth	9	9	missed Earth
4	N00W00	N20W19	37.83	36.36	37.73	9	9	9
6	S05E17	S16E23	33.50	31.90	32.22	7	9	9
9	N06E11	S13E42	60.00	34.63	36.97	4	9	9

The propagation time forecasts experienced slight increases for 4 of the events, which were all increases in accuracy due to the fact that all 4 of the propagation times were underestimated by the ensemble. The maximum change in the propagation time was 2.3 *hours* for event 9, and the minimum change was 0.3 *hours* for event 6. This indicated that moderate changes in the propagation axes, by themselves, did not have large effects on the propagation times. But, large changes in the propagation axes, such as event 2, can force the CMEs to miss Earth altogether.

The maximum K_p index forecast did not change for the 4 events which hit Earth, with all forecasts predicting a maximum K_p index of 9 (Table 25 and Figure 56). This

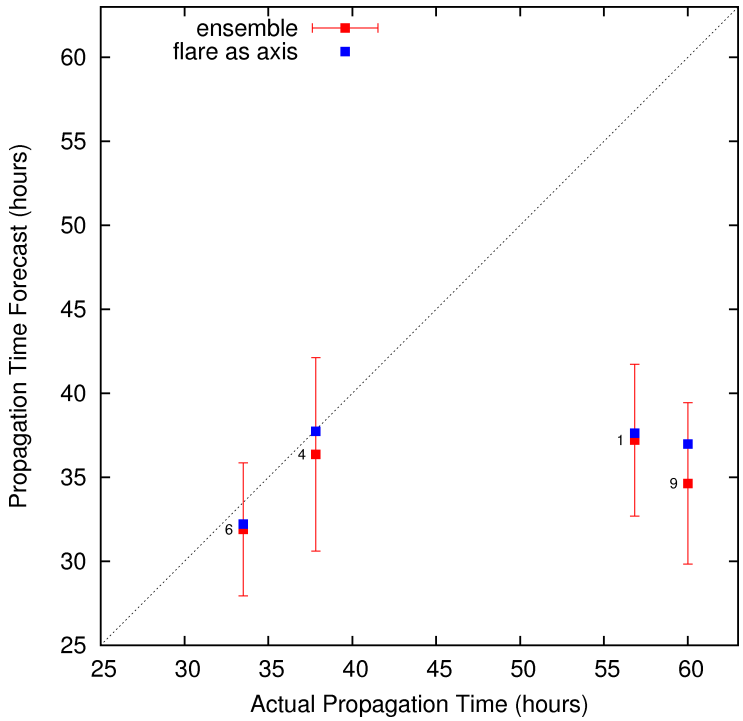

Figure 55. The propagation time forecasts using the flare locations as the propagation axes versus the actual propagation times, along with the ensemble forecasts. The error bars are the standard deviations of the ensembles.

indicated that moderate changes in the propagation axes did not affect the maximum K_p index forecasts.

While moderate changes in the propagation axes alone did not produce large changes in the forecasts, moderate changes in the propagation axes predicted by the Coned Model should have larger effects on the forecasts due to the fact that the cone parameters are interdependent, and an increase in the magnitude of the propagation axes angles (latitude/longitude) would decrease the velocity estimated by the Coned Model (see the discussion concerning Figure 22 for more detail). This combination of changes should have a large effect on forecasts, while changes in the propagation axes alone do not.

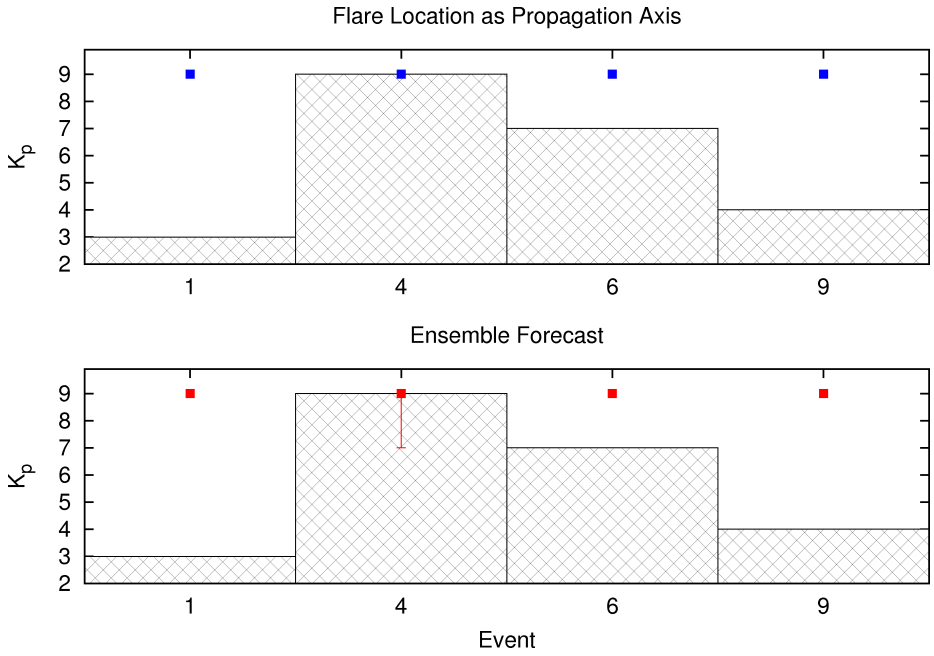

Figure 56. The maximum $\mathrm{K_p}$ index forecasts using the flare locations as the propagation axes along with the actual maximum $\mathrm{K_p}$ index and the ensemble forecasts. The bars are the actual maximum $\mathrm{K_p}$ indices, and the error bars are the ranges of the ensembles.

V. Conclusion

The core analysis consisted of using the WSA-ENLIL version 2.7 with Coned Model version 1.3 to produce ensemble forecasts of 15 halo-CMEs. The ensemble forecasts consisted of the propagation times to the L_1 Lagrangian point and the associated maximum K_p indices due to the impact of the CMEs on the Earth's magnetosphere. 100 sets of input parameters were derived from the Coned Model for each CME, which were used as input to WSA-ENLIL to calculate the propagation times and maximum K_p indices. The ensemble forecasts were compared to the actual propagation times and maximum K_p indices to test the accuracy of the ensemble forecasting approach.

The propagation time ensemble forecasts estimated 5 of 15 events with accuracy such that the actual propagation time lay within the ensemble average plus or minus the ensemble standard deviation. All 5 of the events had actual propagation times between 30 and 46 *hours*. 8 of 15 events were forecast with accuracy such that the actual propagation time lay within the range of the ensemble.

The mean absolute forecast error, for the 15 CMEs, was calculated to be 9.1 *hours*. This was greater than the mean absolute forecast error of 6.9 *hours* calculated for the analytic Cone Model by *Taktakishvili et al.* [2011], but less than the mean absolute forecast error of 11.2 *hours* calculated for the automatic Cone Model (Coned Model) using the median values of the cone parameter distributions as the cone parameters for a single ENLIL run by *Taktakishvili et al.* [2011].

The ensemble propagation times were mostly accurate for CMEs with actual propagation times between 27 and 46 *hours*. The forecasts for CMEs with actual propagation times less than 20 *hours* overestimated the propagation times by about 9 *hours*, due to an underestimation of the CME velocity. The forecasts for CMEs with actual propagation times greater than 46 *hours* were inaccurate. The large nega-

tive forecasting errors for the CMEs with actual propagation times greater than 46 *hours* were most likely due to the combination of velocity overestimations and miscalculations of the propagation axes by Coned Model version 1.3. The propagation axes derived from the Coned Model tended to be pushed towards the Sun-Earth line, forming a narrow distribution relative to the large spread of associated solar flare locations. The velocities and magnitudes of the propagation axes angles (latitude and longitude) predicted by the Coned Model were shown to be inversely related, which indicated that forcing the propagation axes towards the Sun-Earth line may have forced overestimations of the velocities for the slower events. This tendency could be corrected by modifying the optimization routine used by the Coned Model to allow for additional information to be taken into account, such as the eruption location and propagation axis information derived from STEREO.

Perhaps the most important result of this analysis was the dynamic quantification of the forecast uncertainty derived strictly from measurements (LASCO imagery) of the particular CME of interest. The forecast uncertainty was dynamic because it depended on the measurements of the particular event of interest, and varied from event to event. The average of the standard deviations of the propagation time ensembles, for all 15 events, was calculated to be 4.6 *hours*. The average of the ranges of the propagation time ensembles was calculated to be 22.2 *hours*. While these values were not a measure of the forecast accuracy, they did provide a measure of the uncertainty in the forecasts based on the uncertainty in the measurements of the initial conditions. The uncertainty of a forecast is useful information, since it describes the distribution of forecasts which were used to create the average forecast and provides a measure of the range of possible forecasts.

The maximum K_p indices were calculated using the maximum K_p index formula derived from *Newell et al.* [2007], with the assumption that the magnetic field was

completely southward. The ensemble forecast predicted maximum K_p indices of 9 for all events, which was an overestimation for many of the events. 10 of the 15 events were forecast with accuracy such that the actual maximum K_p index lay within the range of the ensemble forecast. 7 of the 15 events had an actual maximum K_p index of 9, which indicated that only 3 of the 8 events with actual maximum K_p indices less than 9 had forecasts with the actual value inside the range of the ensemble.

The mean absolute forecast error for the maximum K_p index was calculated to be 1.66, with an average ensemble standard deviation of 0.11, and an average ensemble range of 0.74. Only 4 of the 15 events had non-zero uncertainties due to the overestimation of the maximum K_p indices and the fact that any maximum K_p index estimate over 9 had to be rounded down to 9. Therefore, the averages of the maximum K_p uncertainties were not extremely meaningful.

One possible cause of the overestimation of the maximum K_p indices was the assumption that the magnetic field was completely southward. An alternative approach was analyzed, where the expected value of the clock-angle term in the *Newell et al.* [2007] maximum K_p index formula was calculated assuming a randomly oriented clock-angle with a uniform distribution. Using the expected value for the clock-angle term lowered the forecasts such that 9 was not predicted for every event. Furthermore, 9 of the 15 events were forecast with accuracy such that the actual maximum K_p index lay within the range of the ensemble. 6 of the 15 forecasts underestimated the maximum K_p index. The mean absolute forecast error was calculated to be 1.80, which indicated that using the expected value for the clock-angle term performed slightly less accurately than the completely southward magnetic field forecasts. The forecasts completed using the expected value for the clock-angle term were more accurate than the forecasts completed assuming the magnetic field was competely southward for the events with actual maximum K_p indices less than 9, but were less accurate for the

events with actual maximum K_p indices of 9. This displayed an alternative method for calculating the impact of a CME, which could be used in conjunction with the completely southward magnetic field forecast to provide a range of possible maximum K_p indices.

Overall, the ensemble propagation time forecast outperformed all of the reference models, including STOA, ISPM, the LASCO first-order POS velocity, the type II speed, the average Coned Model velocity, and the ENLIL "single-shot" forecast. While the ensemble forecast did not perform more accurately for all of the separate events, it did perform more accurately overall. The average of the ensemble propagation time was shown to perform slightly more accurately than the median of the ensemble propagation time. The ensemble maximum K_p index forecasts performed exactly the same as the ENLIL "single-shot" forecasts, with a skill score of zero, but the ensemble forecasts provided a range of values while the "single-shot" forecasts did not.

The core analysis was repeated using Coned Model version 1.2. Overall, the propagation time forecasts were less accurate while the maximum K_p forecasts were slightly more accurate. Additionally, Coned Model version 1.2 tended to accurately forecast the propagation times for the events with actual propagation times greater than 46 *hours* due to a decrease in the velocities calculated by version 1.3.

With the knowledge that Coned Model version 1.2 performed more accurately for events with actual propagation times greater than 46 *hours*, an unsuccessful attempt was made at locating the slower events strictly from data available at the time of the CME eruption. No clear patterns emerged for the propagation time forecast error for Coned Model version 1.3 versus the associated solar flare location, type II speed, LASCO first-order POS velocity, or Coned Model parameters.

A generalized linear model (GLM) was employed to determine if a combination

of parameters could locate the slower CMEs. The GLM was created with 3 different predictor sets: the cone parameters, the non-cone parameters, and a combination of the cone and non-cone parameters. When applied to 4 test CMEs, the predictor set of the non-cone parameters performed the best predicting 3 of the 4 events correctly. Overall, the GLM did not have enough data-points to perform an accurate logistic regression or to create an accurate statistical model, since only 15 data-points were available from this analysis. The framework was developed for a future application of a GLM to this problem when more data-points become available.

The ensemble forecast using the WSA-ENLIL with Coned Model was found to be robust with respect to changes in the input parameters other than the cone parameters. The variation in the ensemble size caused a maximum propagation time forecast change of 4%, and no change in the maximum K_p index forecast. The variation in ensemble size did change the propagation time range by 49%, which was most likely due to the improper sampling of the input parameter distributions by the Coned Model for the smaller ensemble sizes. Therefore, ensemble sizes greater than or equal to 100 should always be used for ensemble forecasting using the WSA-ENLIL with Coned Model. The variation in the magnetogram source locations caused a maximum change of 3% in the propagation time forecast, and no change in the maximum K_p index forecast. The variation in the images used for the Coned Model caused a 3% change in the propagation time forecast, but changed the propagation time range by 29%. No change in the maximum K_p forecast was observed. The variation in the magnetic field scaling factor caused a maximum change of 3% in the propagation time forecasts, and a 17% change in the propagation time range. No change in the maximum K_p forecasts were observed. The variation in the magnetic field scaling factor did cause a change in the minimum value for the maximum K_p indices (and therefore a change in the range) for 3 of the 11 events analyzed, which was due to

the change in the magnetic field magnitude estimates.

5.1 Future Efforts

The next step in ensemble forecasting of CMEs using the WSA-ENLIL with Coned Model should be to update the Coned Model to allow for the location of the CME eruption (associated solar flare location) and propagation axis information from STEREO to be taken into account when calculating the cone parameters. This analysis showed that the Coned Model tends to push the propagation axes of CMEs towards the Sun-Earth line, which is not always the actual propagation axis for CMEs. An improvement in the direction of propagation may also improve the accuracy of the velocity estimations due to the fact that the cone parameters calculated by the Coned Model are interdependent. Allowing for propagation axes further on the solar limb would force the Coned Model to predict slower velocities, which may alleviate the problem of the slower CMEs which caused large negative forecast errors. The more accurately the Coned Model represents the initial state of a CME, the more accurate the forecasts will become.

The next version of ENLIL will allow for an internal magnetic field structure in the CME "cloud", which may help to improve the maximum K_p forecasts. Even though this addition will not allow for the calculation of a meaningful magnetic field clock-angle at Earth, due to the fact that there is no current capability to measure the initial orientation of the magnetic field inside of a CME, it may improve the estimates of the magnetic field magnitude which would improve the maximum K_p forecasts.

Additional CMEs should be analyzed to obtain a larger set of results, which would help locate any trends or problems with the models. Additional sets of results could also be used to help improve the GLM, which could be used to determine the most accurate version of the Coned Model to use for a particular event. To help increase

the number of events analyzed, the model execution speed should be increased. This analysis required around 36 *hours* to complete one ensemble forecast, which limited the number of events that could be analyzed. If the model execution experiences a significant increase in speed, a larger number of events could be analyzed in a shorter time.

The goal in the next series of ensemble forecasting analyses should be to forecast the propagation times and maximum K_p indices with accuracy such that all of the ensemble ranges contain the actual values. Once this is achieved, the goal for the propagation time should be to forecast the events with accuracy such that the actual value is inside of the ensemble average plus or minus one standard deviation, for all events.

Appendix A. Ensemble Forecasting Procedures

The first step in producing an ensemble forecast using WSA-ENLIL with Coned Model is to run the Coned Model for a particular event. The Coned Model can be run through A. Pulkkinen's machine using a secure shell (SSH) protocol. The Coned Model requires a time series of LASCO C3 images of the CME eruption, which can be found at CCMC's iNtegrated Space Weather Analysis System (iSWSA) located at `http://iswa.ccmc.gsfc.nasa.gov:8080/IswaSystemWebApp/`. This analysis used three LASCO C3 images with a time span of at least one-hour between the first and last image. The time stamps of the LASCO images are used as input to the Coned Model along with the filtering threshold level. The time stamps of the images used as input to the Coned Model as well as the threshold filtering level used for the images, for the 15 CMEs used in this analysis, are displayed in Table 26.

The image time stamps and threshold filtering levels must be input to the Octave script RunEnsembleAnalysis.m. The RunEnsembleAnalysis.m script must then be executed in Octave. After the script is executed, 100 sets of input parameters are created along with a separate control file produced for each set. The RunEnsemble-Analysis.m script will produce a snapshot of the filtered LASCO images as well as the distribution of the 100 sets of input parameters. If the filtered LASCO images show large outliers of CME mass, then the threshold filter should be adjusted and the RunEnsembleAnalysis.m script should be re-executed. The Coned Model requires about one hour to complete when using SSH.

The 100 control files containing the 100 sets of input parameters must be transferred to A. Taktakishvili's machine to be used as input for WSA-ENLIL. The control files can be transferred via Secure Copy (SCP). In order to run WSA-ENLIL, WSA must be run for the appropriate Carrington rotation, and the solar wind and IMF solution must be available on A. Taktakishvili's machine. If the solar wind and IMF

Table 26. A list of the time stamps of the LASCO C3 images used as input to the Coned Model along with the threshold level used for filtering the images.

CME Start Date (YYYYMMDD)	LASCO C3 Image Time Stamps (YYYYMMDDHHMMSS)	Filtering Threshold Level
20010329	20010329114200	0.56
	20010329121800	
	20010329124200	
20031029	20031029211900	0.56
	20031029214200	
	20031029221800	
20041106	20041106021800	0.56
	20041106024200	
	20041106041800	
20031028	20031028114200	0.56
	20031028121800	
	20031028124200	
20000714	20000714111800	0.56
	20000714114200	
	20000714121800	
20011104	20011104170000	0.56
	20011104173000	
	20011104180200	
19990503	19990503074200	0.60
	19990503081800	
	19990503084200	
20041203	20041203014200	0.58
	20041203021800	
	20041203024200	
20011117	20011117064200	0.56
	20011117074200	
	20011117084200	
20011009	20011009134200	0.56
	20011009141800	
	20011009144200	
20100403	20100403114200	0.56
	20100403121800	
	20100403134200	
20040720	20040720151800	0.56
	20040720154200	
	20040720161800	
20010924	20010924111800	0.56
	20010924114200	
	20010924121800	
20000404	20000404164300	0.56
	20000404171800	
	20000404174200	
20010410	20010410061800	0.58
	20010410064200	
	20010410074200	

solution from WSA is not available, P. MacNeice must be contacted to run WSA for the Carrington rotation and magnetogram source location of interest. Once the 100 control files and the WSA solar wind and IMF solution is in place, a number of scripts must be edited before ENLIL is launched. The following scripts must be edited to point to the correct directories containing the control files, the WSA

solution, and the desired output directory: run_cone_ensemble.sh, wsafr-cone-run-script, produce_CME_estimate.sh, and produce $_{C}$ME_ensemble.sh. After the scripts are edited accordingly, the run_cone_ensemble.sh script can be executed.

The wsafr-cone-run-script provides the WSA solar wind and IMF solution for the particular Carrington rotation to ENLIL. The produce_CME_estimate.sh script finds the arrival times and K_p values from the ENLIL output. The produce $_{C}$ME_ensemble.sh script is used to execute the produce_CME_estimate.sh script for the entire ensemble. The run_cone_ensemble.sh script controls the other scripts, and is the only script that needs to be executed to launch ENLIL, calculate the propagation time, and calculate the maximum K_p for all 100 control files. Around 3 days are required to produce the 100 sets of results.

After the model runs are complete, the 100 sets of input parameters and results can be transferred to a different machine for analysis (my machine in this case). The files can be transferred via SCP. The analysis required for this study was to calculate the statistics of the different distributions, calculate forecast errors, and plot the data. The author created a script to calculate the statistics, calculate the forecast error, and plot the data, and it will be available on A. Taktakishvili's machine for future use. The script is named extract$_{r}$esults.sh, and it will call a number of additional scripts to complete the analysis. The CME eruption date and time, actual propagation time, and actual maximum K_p must be edited, for each CME, in the extract$_{r}$esults.sh script. After the CME particulars are added to the script, it can be executed and will produce a plot of the initial parameter distributions, a plot of the forecast distributions, and a text file with the statistics and forecast errors of the ensemble.

Appendix B. Ensemble Plots

The filtered LASCO images for the 15 CMEs in this analysis, derived from the Coned Model, are displayed in this appendix. The input parameter, propagation time, and maximum K_p ensembles, for the 15 CMEs in this analysis, are also displayed. The input parameters and propagation times, for each of the 100 sets of input parameters, are also displayed for each of the 15 CMEs.

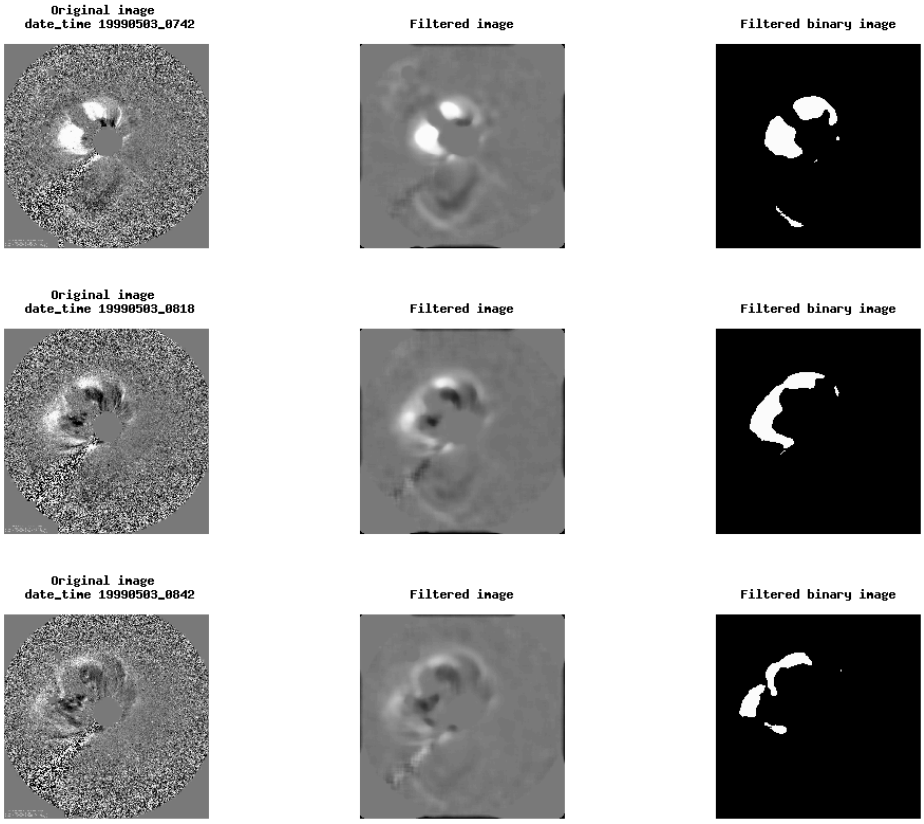

Figure 57. The filtered LASCO images for the 3 May 1999 CME (event 1), derived from Coned Model version 1.3.

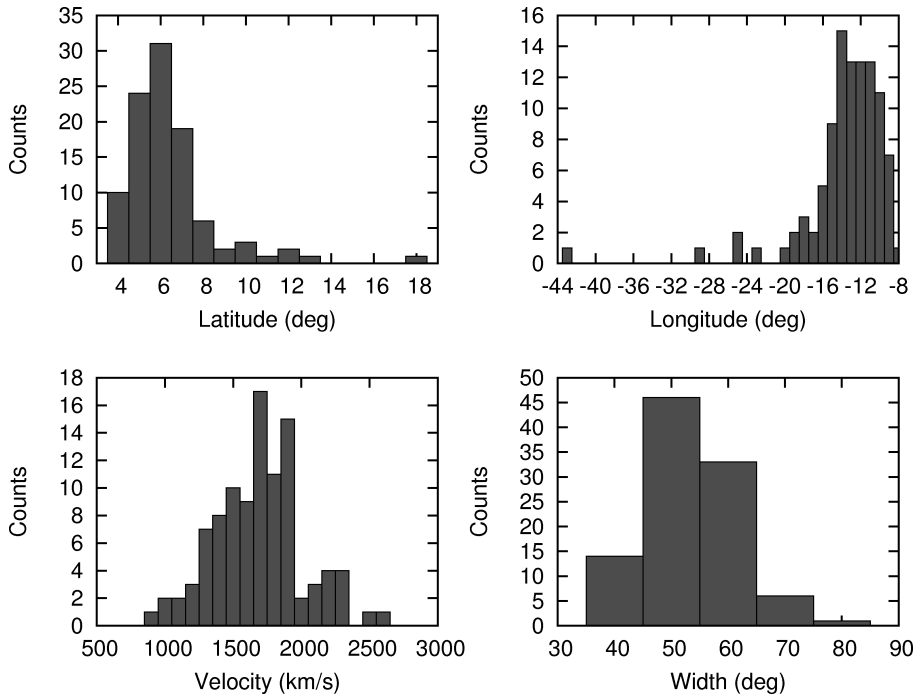

Figure 58. The input cone parameter distributions for the 3 May 1999 CME (event 1), derived from Coned Model version 1.3.

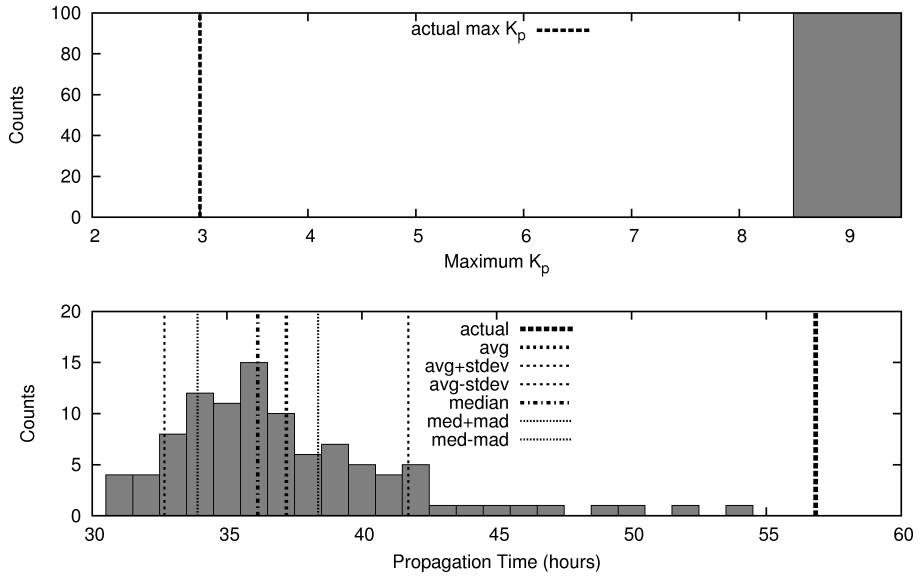

Figure 59. The propagation time and maximum K_p distributions for the 3 May 1999 CME (event 1). In this figure, *avg* stands for average, *stdev* stands for standard deviation, *med* stands for median, and *mad* stands for median absolute deviation.

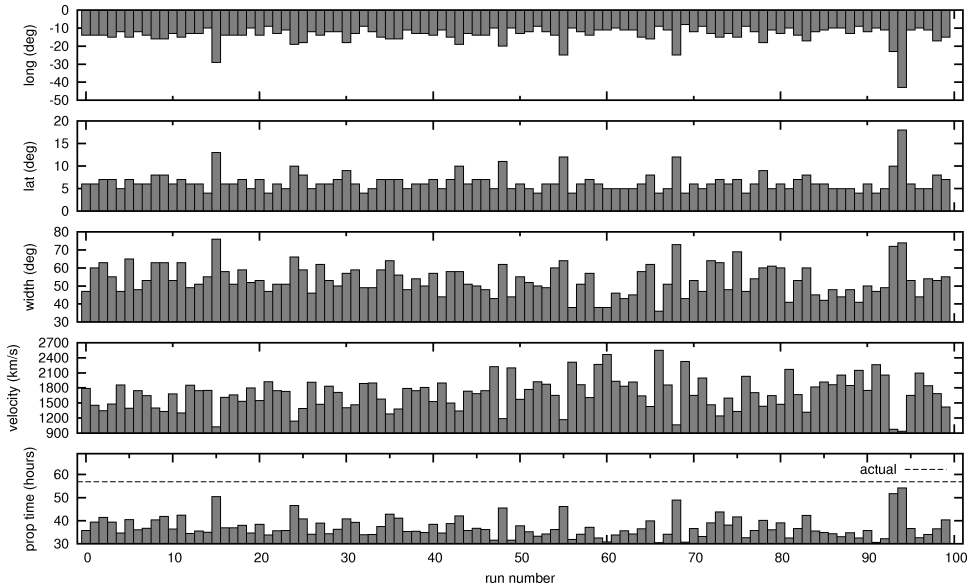

Figure 60. The 100 sets of cone parameters and propagation time forecasts composing the ensemble for the 3 May 1999 CME (event 1).

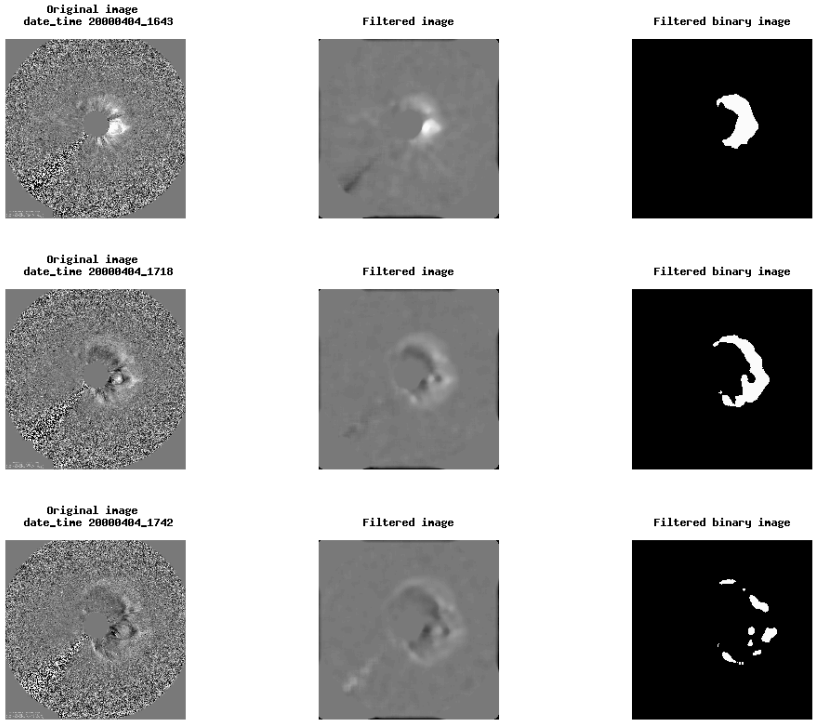

Figure 61. The filtered LASCO images for the 4 Apr 2000 CME (event 2), derived from Coned Model version 1.3.

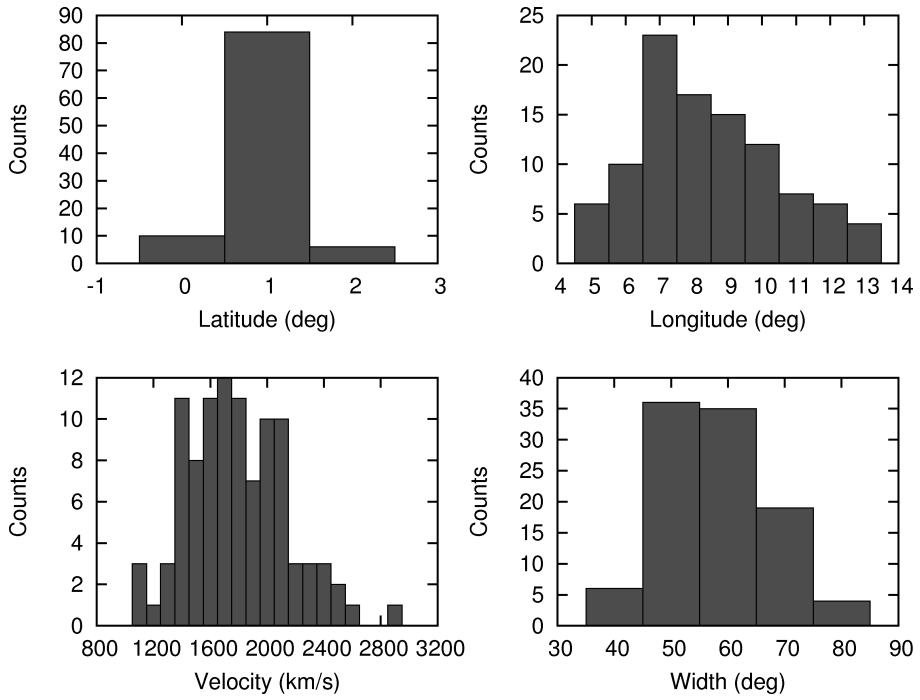

Figure 62. The input cone parameter distributions for the 4 Apr 2000 CME (event 2), derived from Coned Model version 1.3.

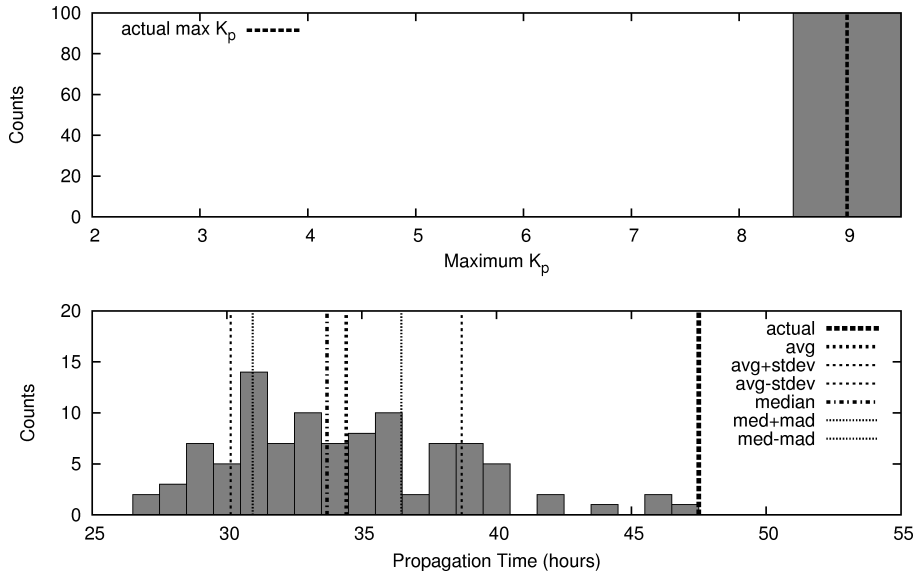

Figure 63. The propagation time and maximum K_p distributions for the 4 Apr 2000 CME (event 2). In this figure, *avg* stands for average, *stdev* stands for standard deviation, *med* stands for median, and *mad* stands for median absolute deviation.

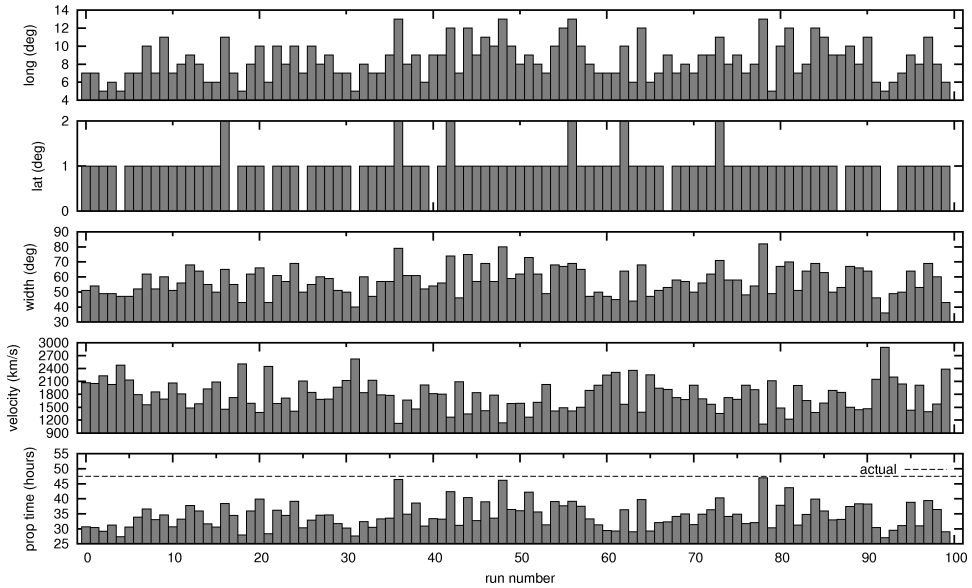

Figure 64. The 100 sets of cone parameters and propagation time forecasts composing the ensemble for the 4 Apr 2000 CME (event 2).

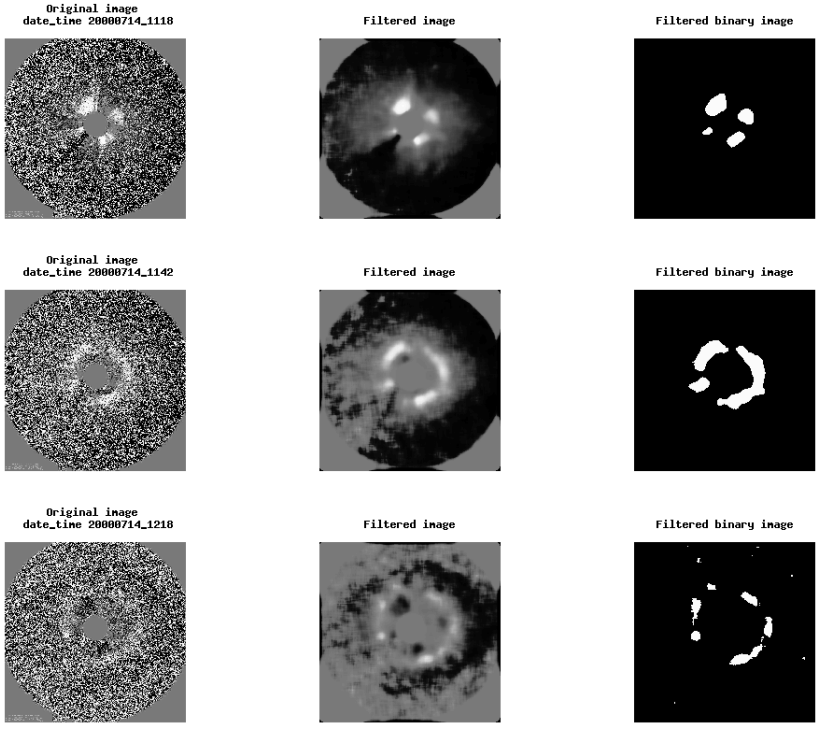

Figure 65. The filtered LASCO images for the 14 Jul 2000 CME (event 3), derived from Coned Model version 1.3.

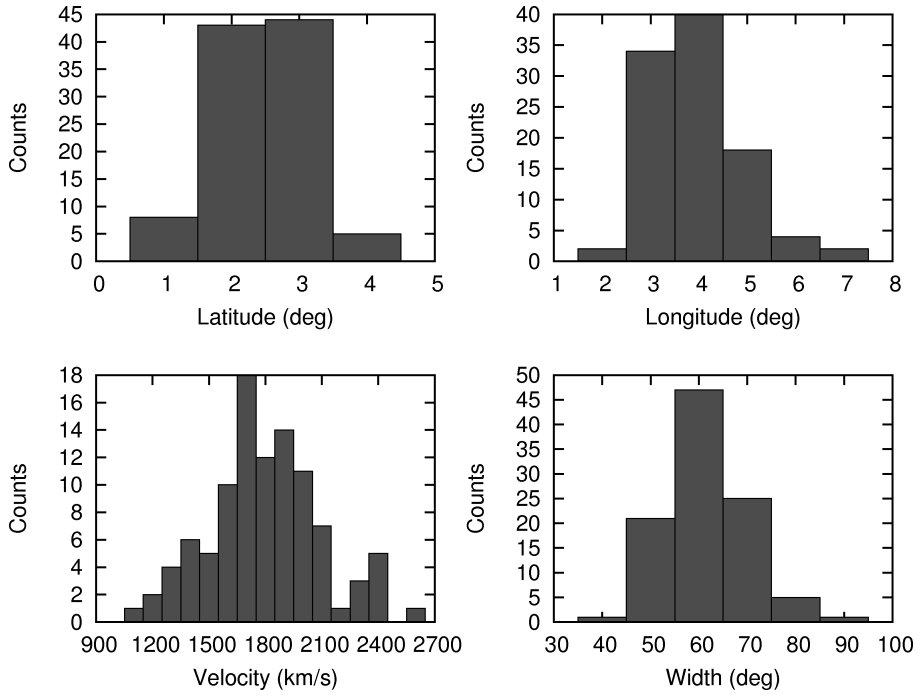

Figure 66. The input cone parameter distributions for the 14 Jul 2000 CME (event 3), derived from Coned Model version 1.3.

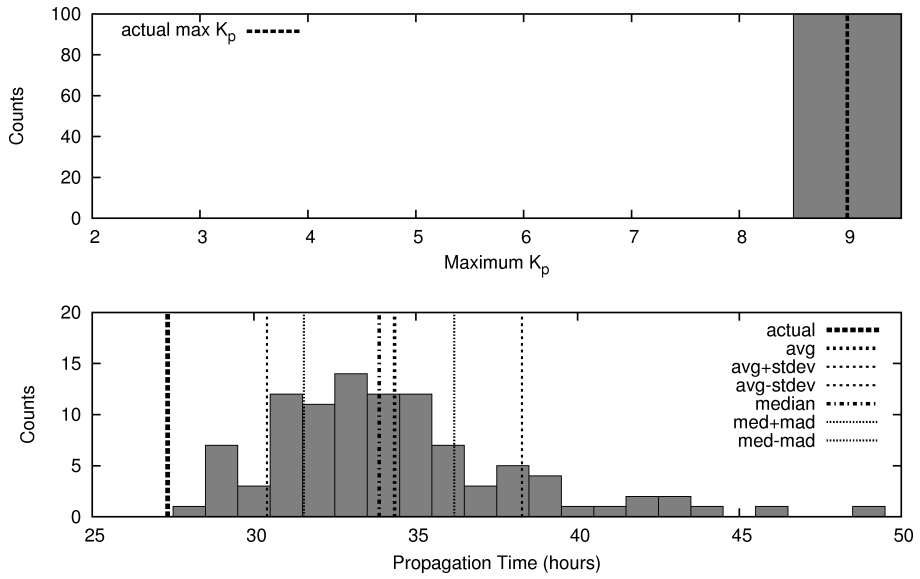

Figure 67. The propagation time and maximum $\mathrm{K_p}$ distributions for the 14 Jul 2000 CME (event 3). In this figure, *avg* stands for average, *stdev* stands for standard deviation, *med* stands for median, and *mad* stands for median absolute deviation.

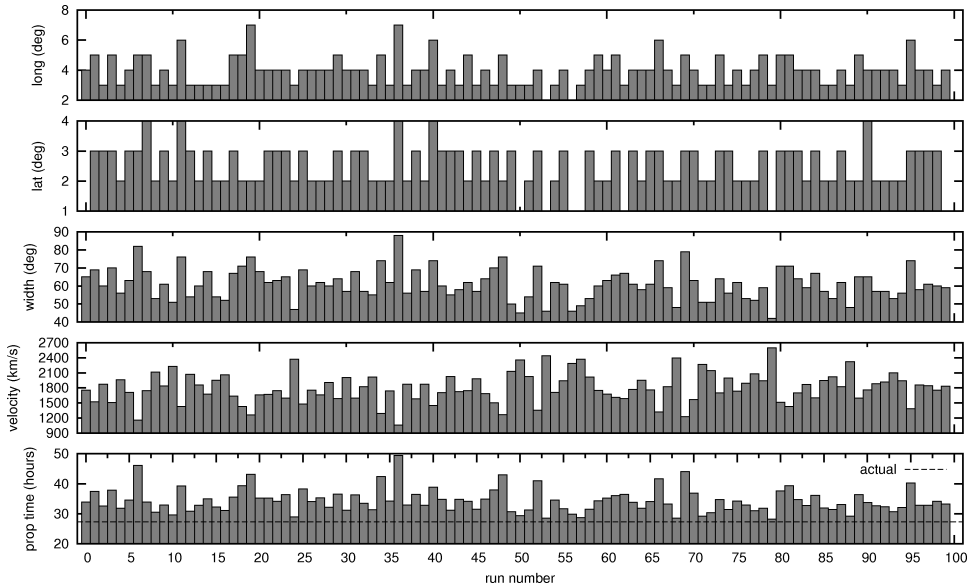

Figure 68. The 100 sets of cone parameters and propagation time forecasts composing the ensemble for the 14 Jul 2000 CME (event 3).

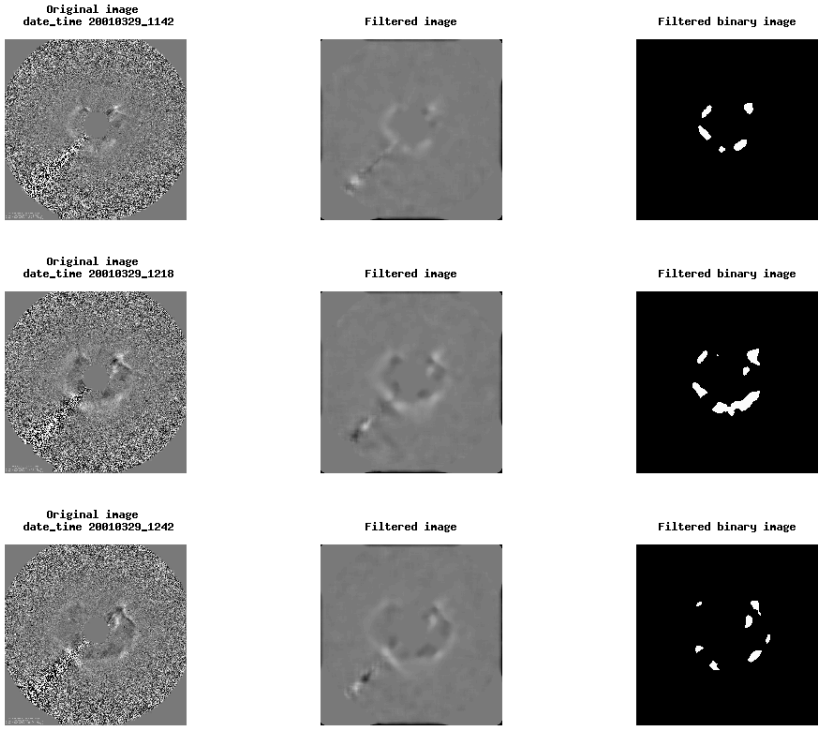

Figure 69. The filtered LASCO images for the 29 Mar 2001 CME (event 4), derived from Coned Model version 1.3.

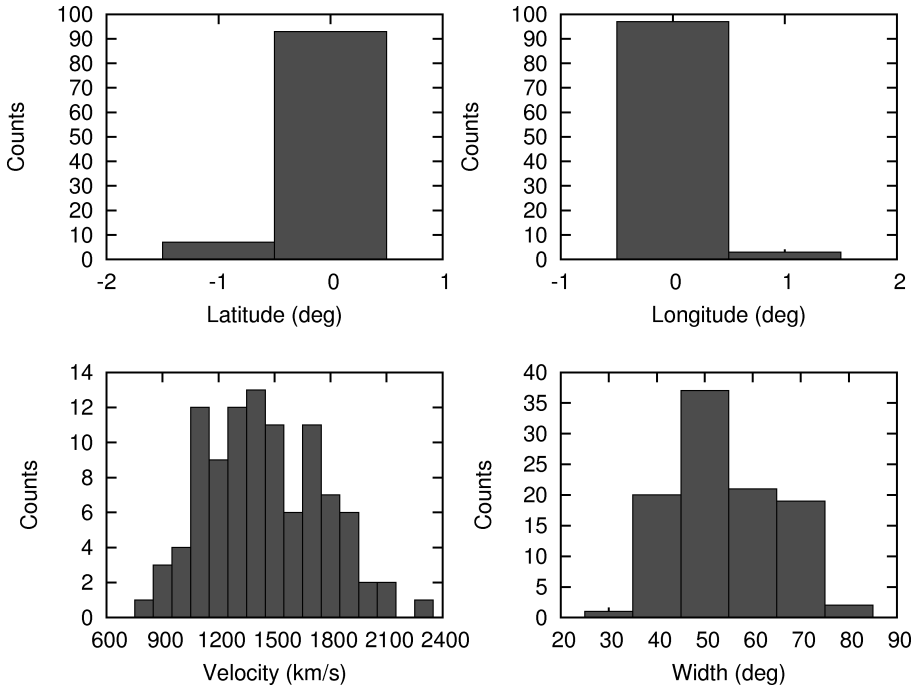

Figure 70. The input cone parameter distributions for the 29 Mar 2001 CME (event 4), derived from Coned Model version 1.3.

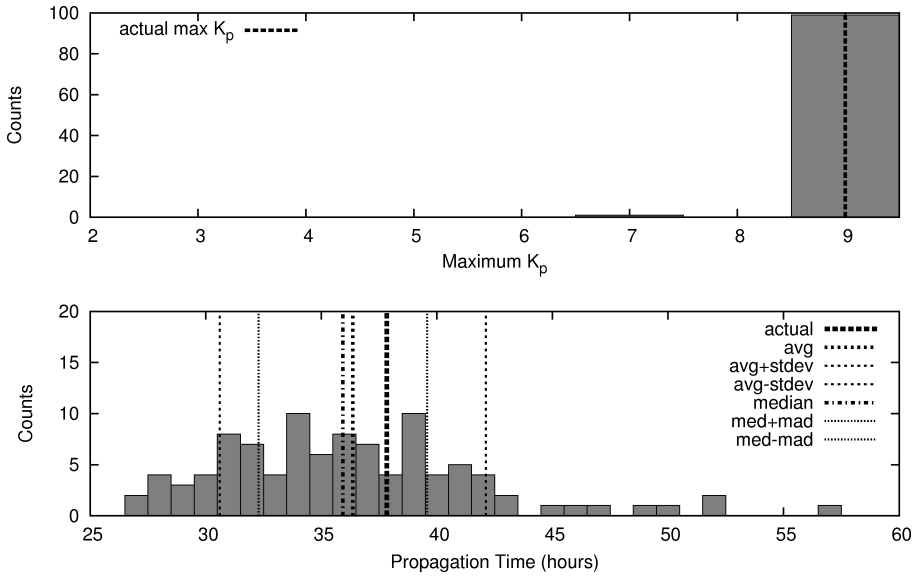

Figure 71. The propagation time and maximum $\mathrm{K_p}$ distributions for the 29 Mar 2001 CME (event 4). In this figure, *avg* stands for average, *stdev* stands for standard deviation, *med* stands for median, and *mad* stands for median absolute deviation.

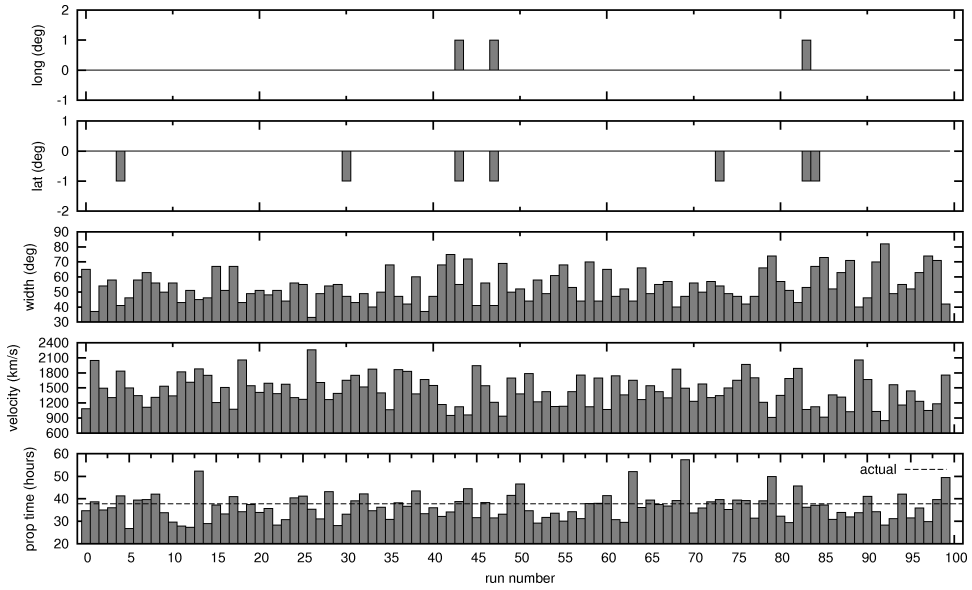

Figure 72. The 100 sets of cone parameters and propagation time forecasts composing the ensemble for the 29 Mar 2001 CME (event 4).

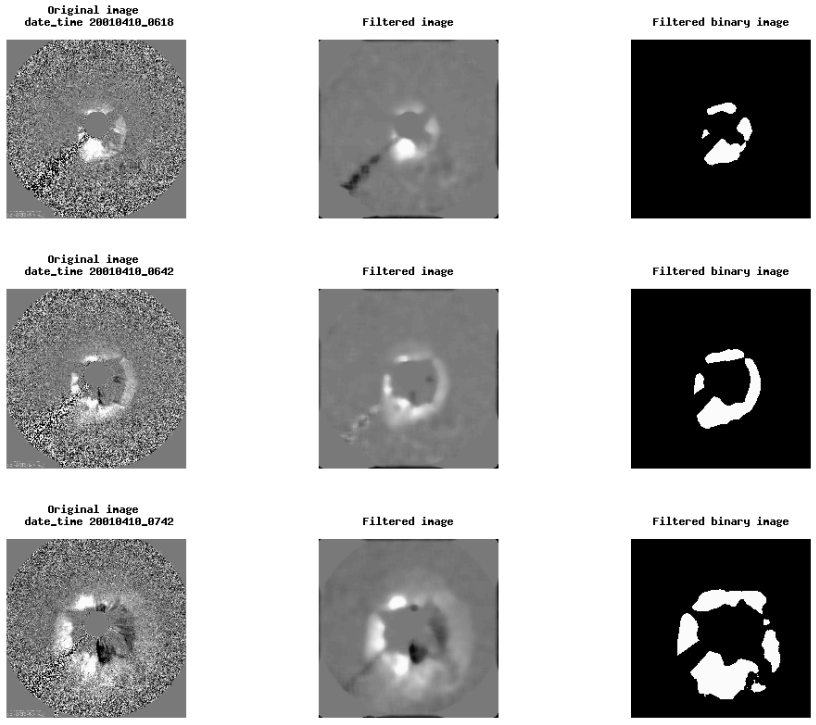

Figure 73. The filtered LASCO images for the 10 Apr 2001 CME (event 5), derived from Coned Model version 1.3.

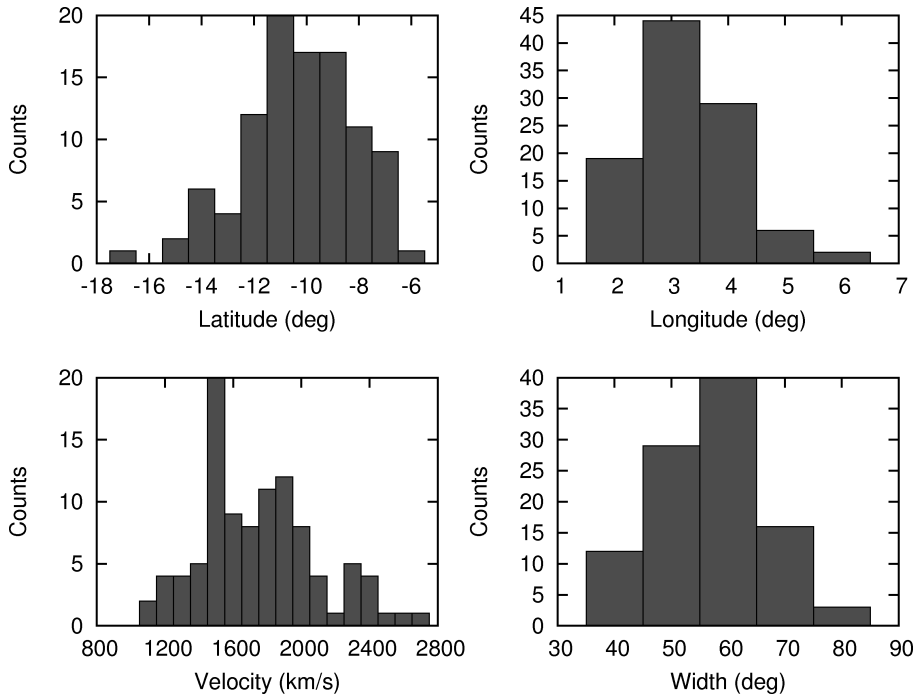

Figure 74. The input cone parameter distributions for the 10 Apr 2001 CME (event 5), derived from Coned Model version 1.3.

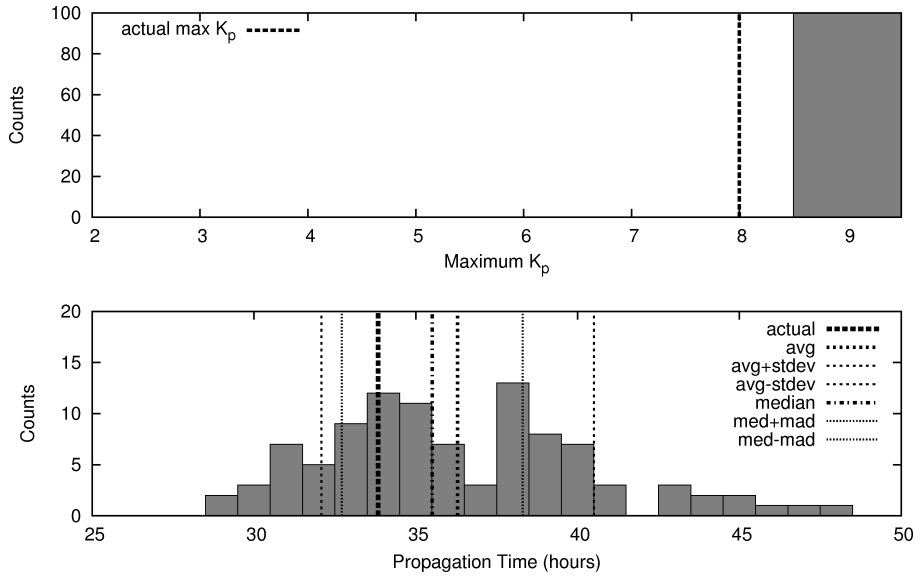

Figure 75. The propagation time and maximum K_p distributions for the 10 Apr 2001 CME (event 5). In this figure, *avg* stands for average, *stdev* stands for standard deviation, *med* stands for median, and *mad* stands for median absolute deviation.

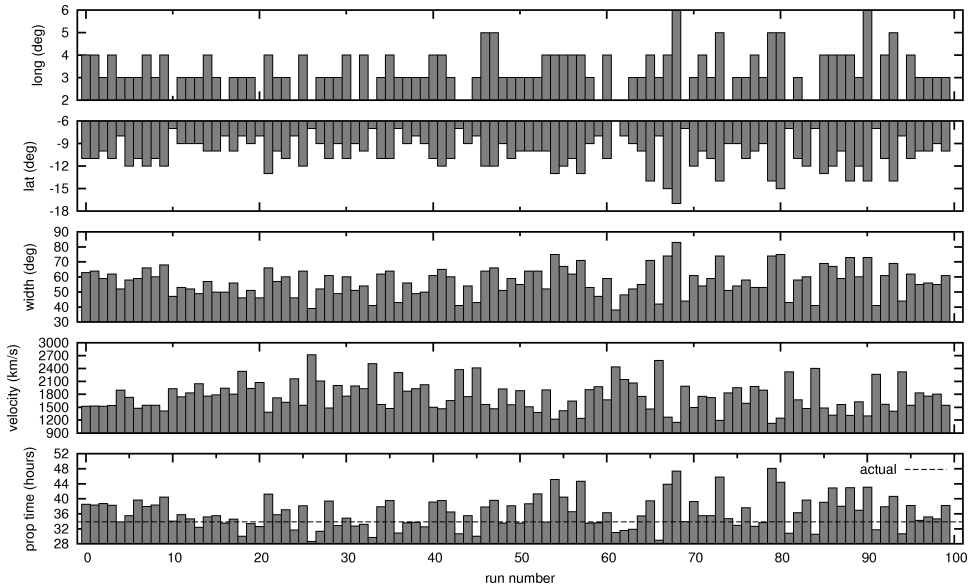

Figure 76. The 100 sets of cone parameters and propagation time forecasts composing the ensemble for the 10 Apr 2001 CME (event 5).

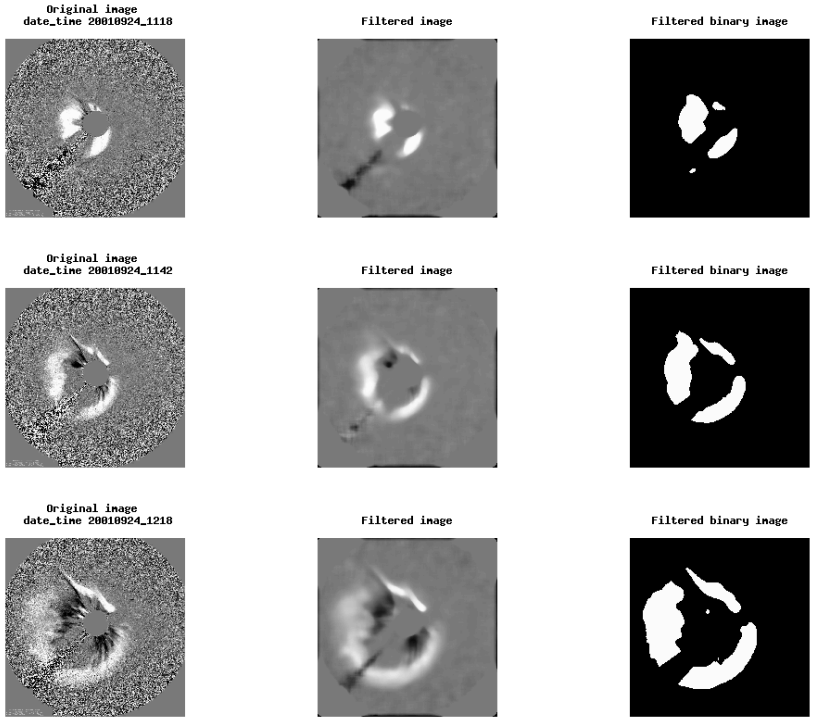

Figure 77. The filtered LASCO images for the 24 Sep 2001 CME (event 6), derived from Coned Model version 1.3.

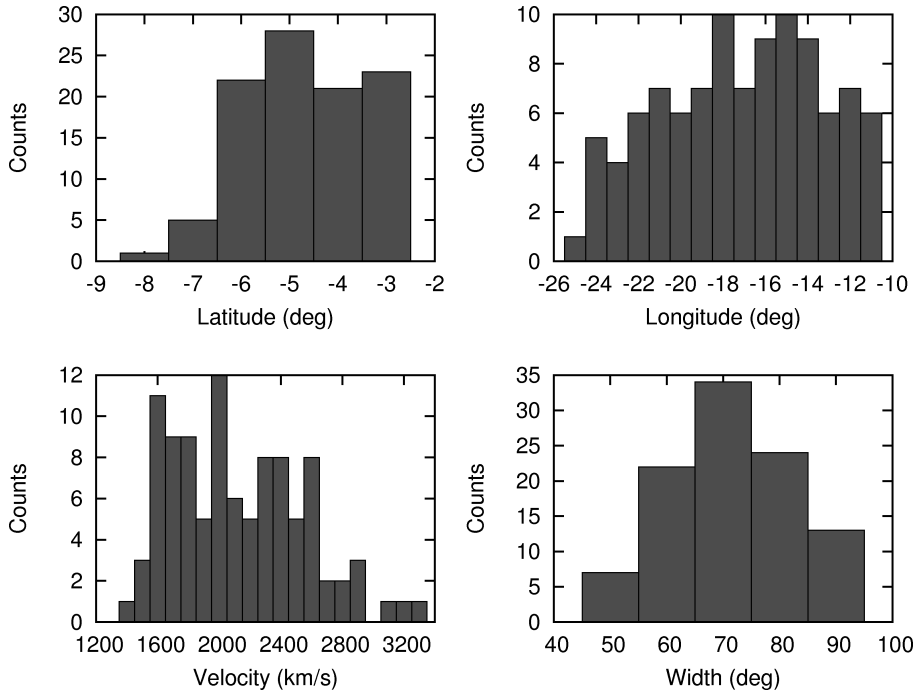

Figure 78. The input cone parameter distributions for the 24 Sep 2001 CME (event 6), derived from Coned Model version 1.3.

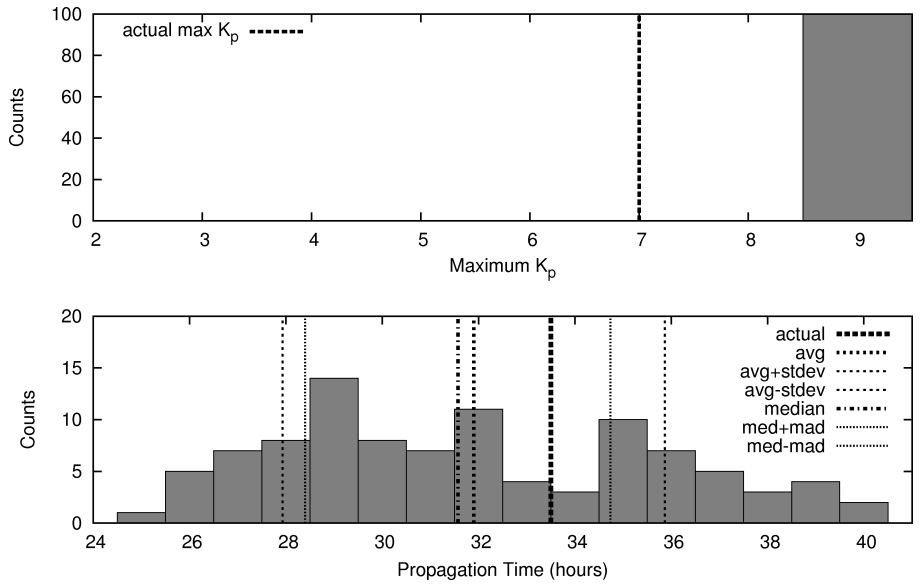

Figure 79. The propagation time and maximum $\mathrm{K_p}$ distributions for the 24 Sep 2001 CME (event 6). In this figure, *avg* stands for average, *stdev* stands for standard deviation, *med* stands for median, and *mad* stands for median absolute deviation.

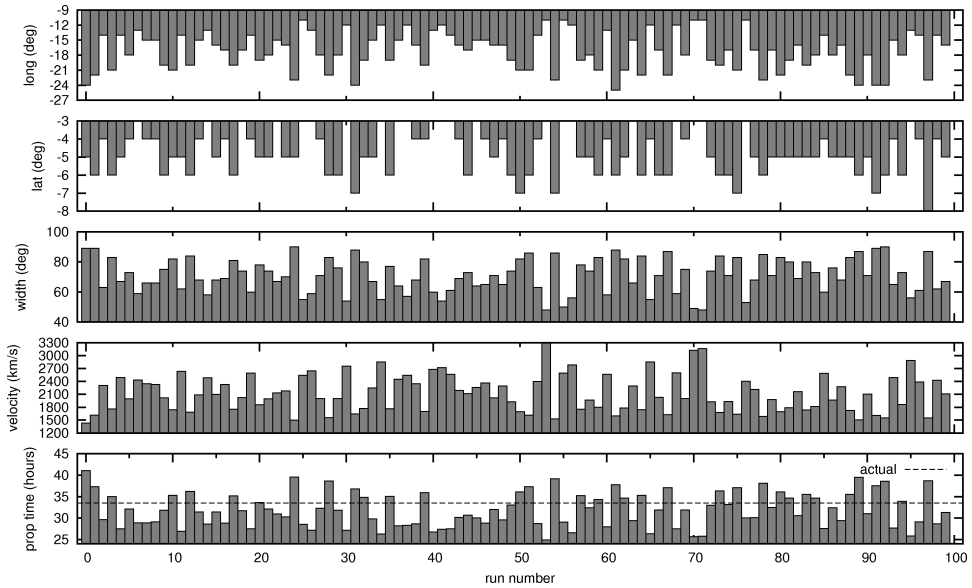

Figure 80. The 100 sets of cone parameters and propagation time forecasts composing the ensemble for the 24 Sep 2001 CME (event 6).

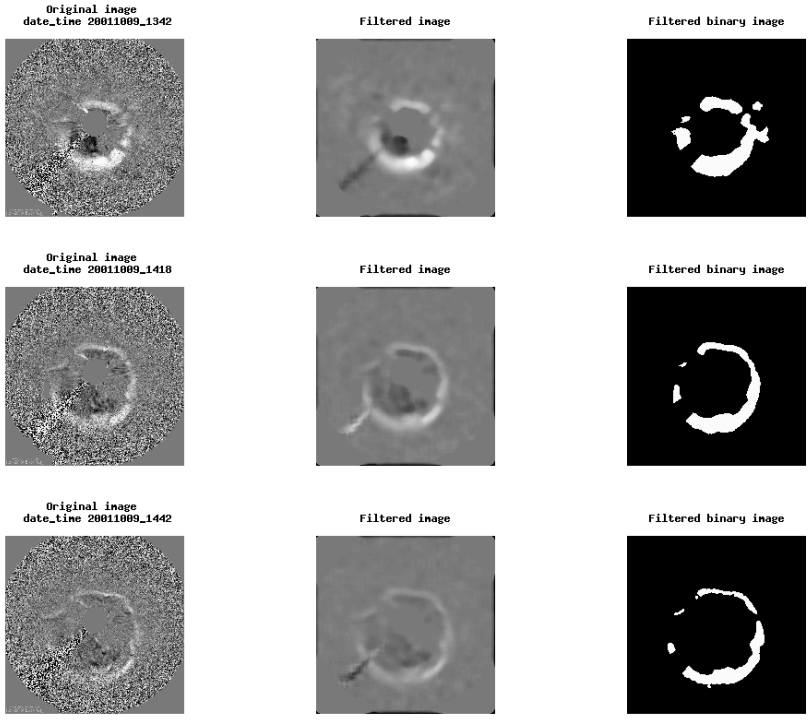

Figure 81. The filtered LASCO images for the 9 Oct 2001 CME (event 7), derived from Coned Model version 1.3.

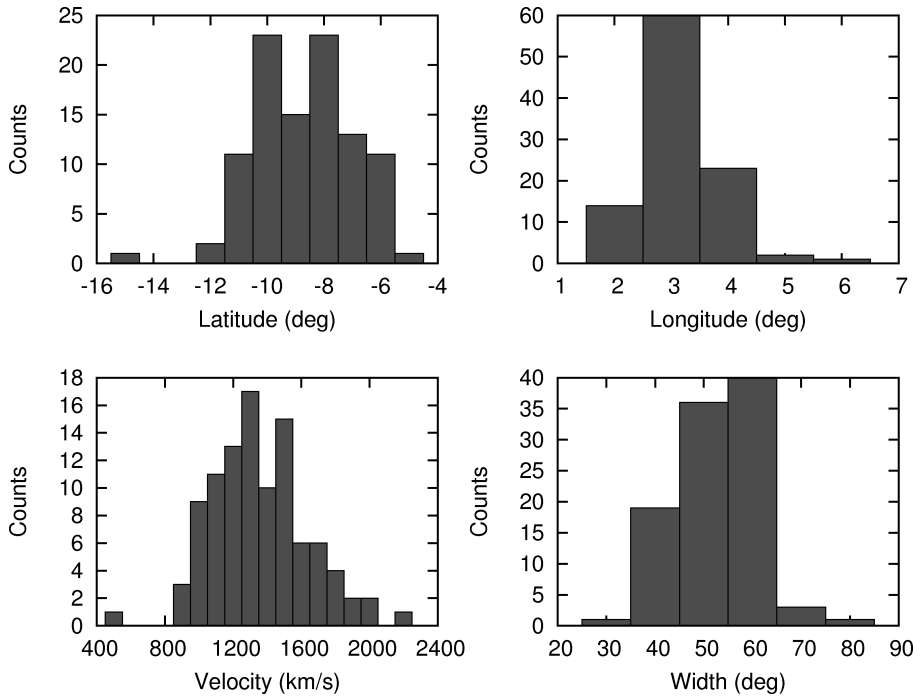

Figure 82. The input cone parameter distributions for the 9 Oct 2001 CME (event 7), derived from Coned Model version 1.3.

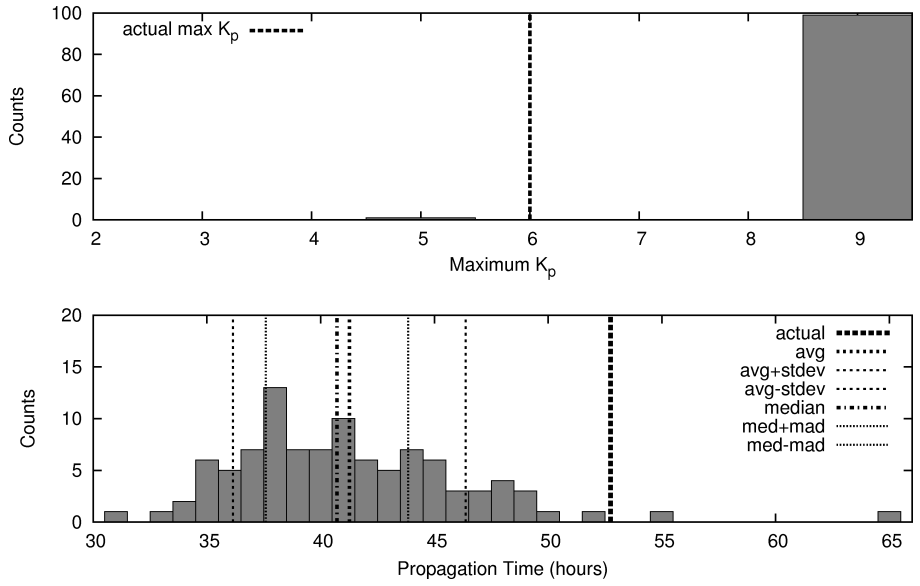

Figure 83. The propagation time and maximum $\mathrm{K_p}$ distributions for the 9 Oct 2001 CME (event 7). In this figure, *avg* stands for average, *stdev* stands for standard deviation, *med* stands for median, and *mad* stands for median absolute deviation.

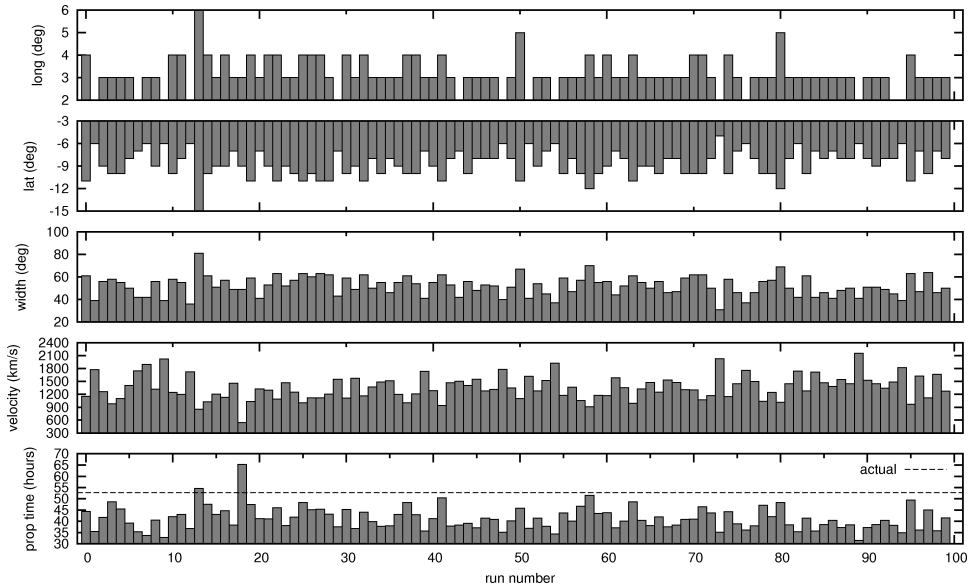

Figure 84. The 100 sets of cone parameters and propagation time forecasts composing the ensemble for the 9 Oct 2001 CME (event 7).

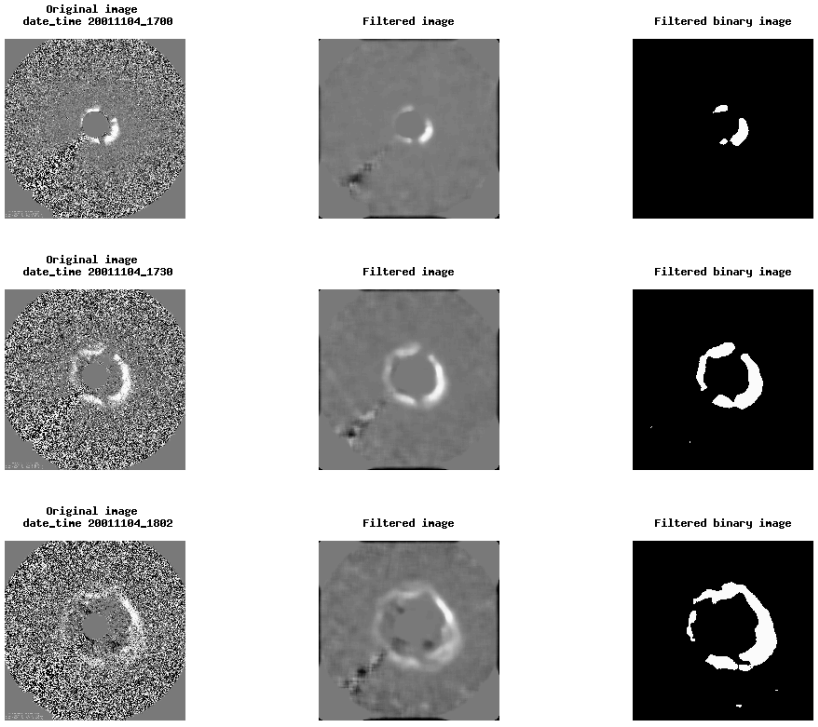

Figure 85. The filtered LASCO images for the 4 Nov 2001 CME (event 8), derived from Coned Model version 1.3.

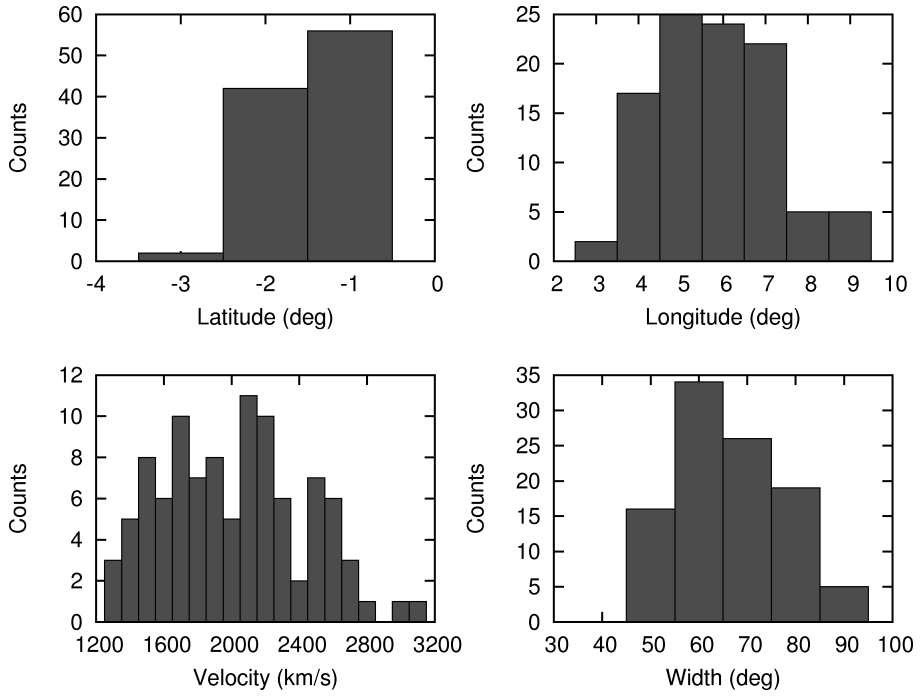

Figure 86. The input cone parameter distributions for the 4 Nov 2001 CME (event 8), derived from Coned Model version 1.3.

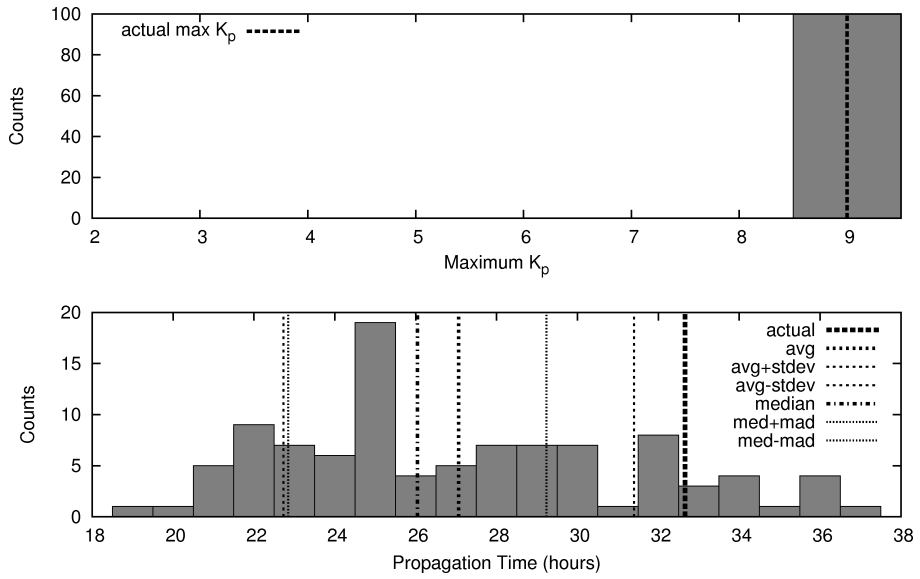

Figure 87. The propagation time and maximum $\mathrm{K_p}$ distributions for the 4 Nov 2001 CME (event 8). In this figure, *avg* stands for average, *stdev* stands for standard deviation, *med* stands for median, and *mad* stands for median absolute deviation.

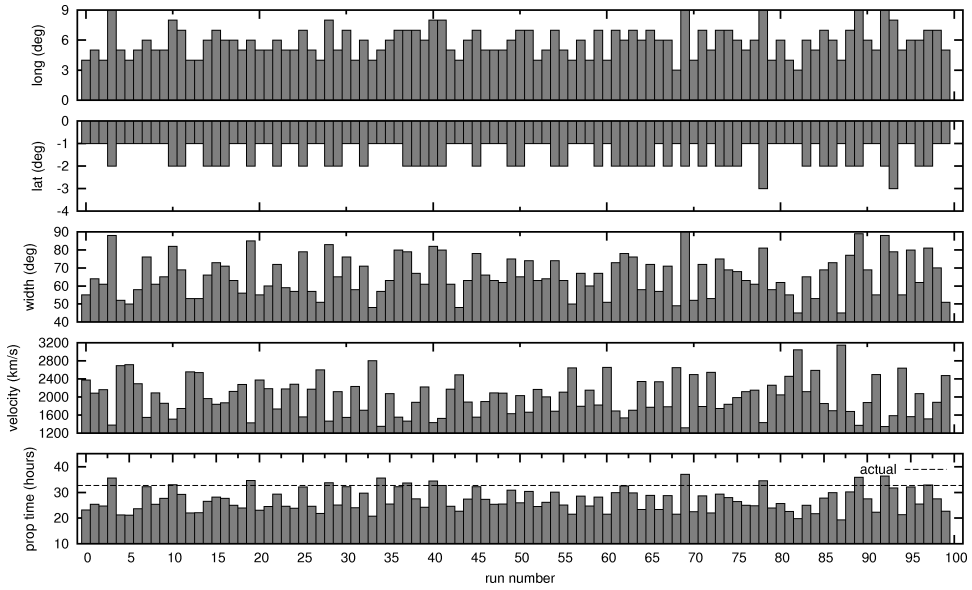

Figure 88. The 100 sets of cone parameters and propagation time forecasts composing the ensemble for the 4 Nov 2001 CME (event 8).

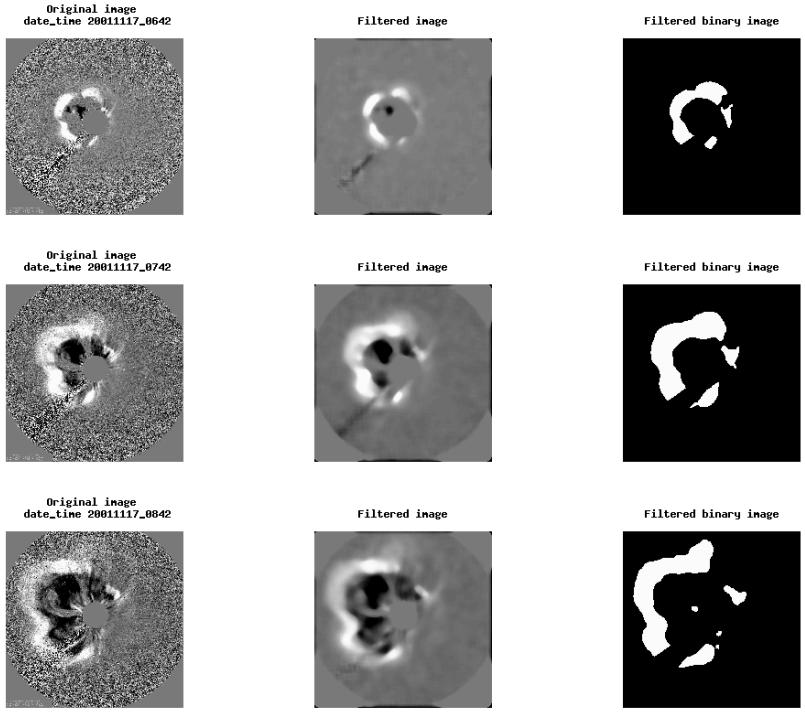

Figure 89. The filtered LASCO images for the 17 Nov 2001 CME (event 9), derived from Coned Model version 1.3.

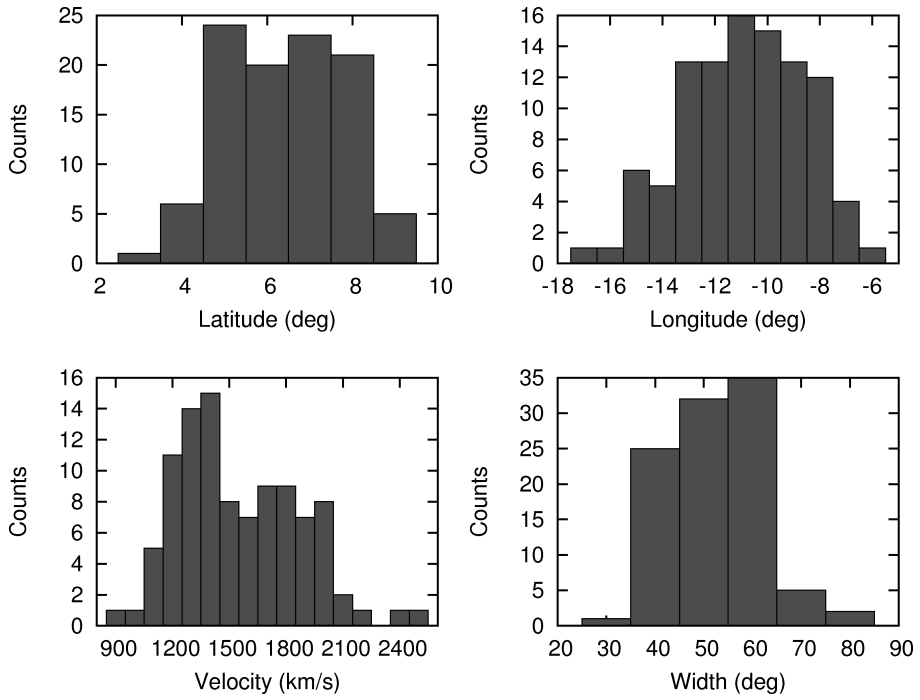

Figure 90. The input cone parameter distributions for the 17 Nov 2001 CME (event 9), derived from Coned Model version 1.3.

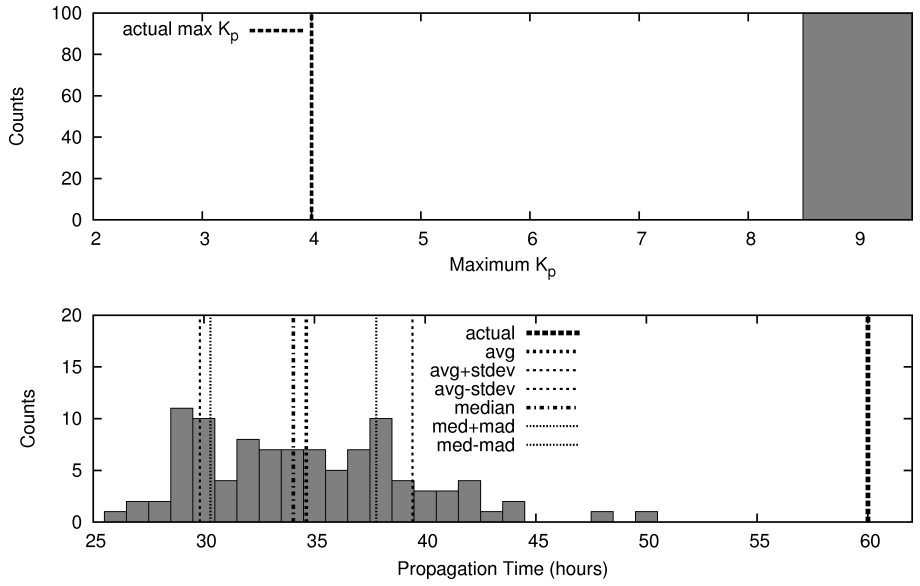

Figure 91. The propagation time and maximum K_p distributions for the 17 Nov 2001 CME (event 9). In this figure, *avg* stands for average, *stdev* stands for standard deviation, *med* stands for median, and *mad* stands for median absolute deviation.

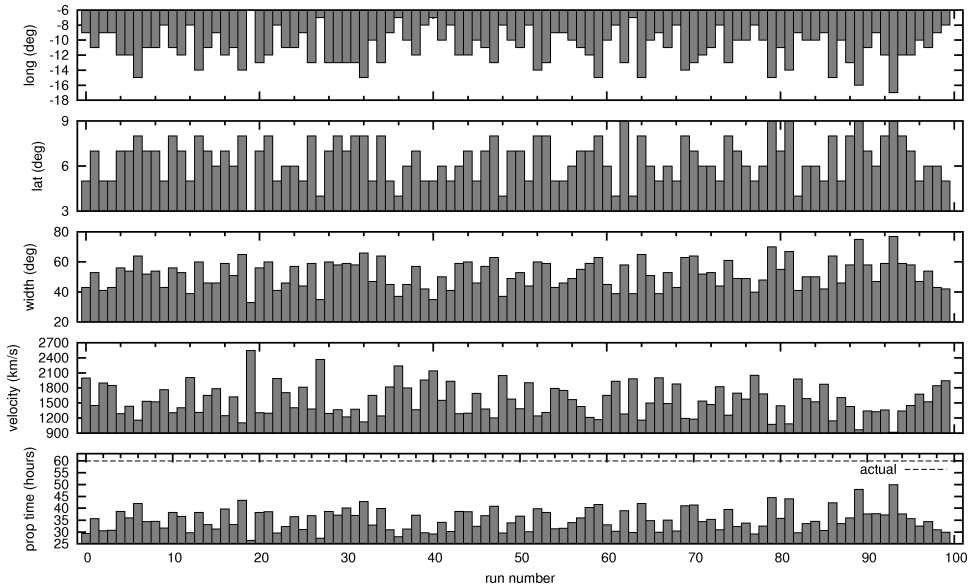

Figure 92. The 100 sets of cone parameters and propagation time forecasts composing the ensemble for the 17 Nov 2001 CME (event 9).

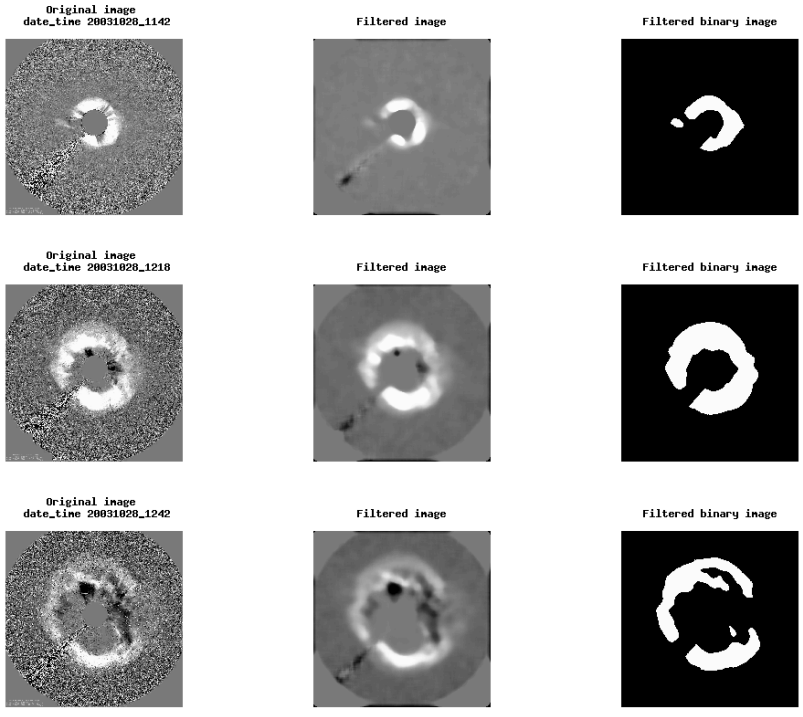

Figure 93. The filtered LASCO images for the 28 Oct 2003 CME (event 10), derived from Coned Model version 1.3.

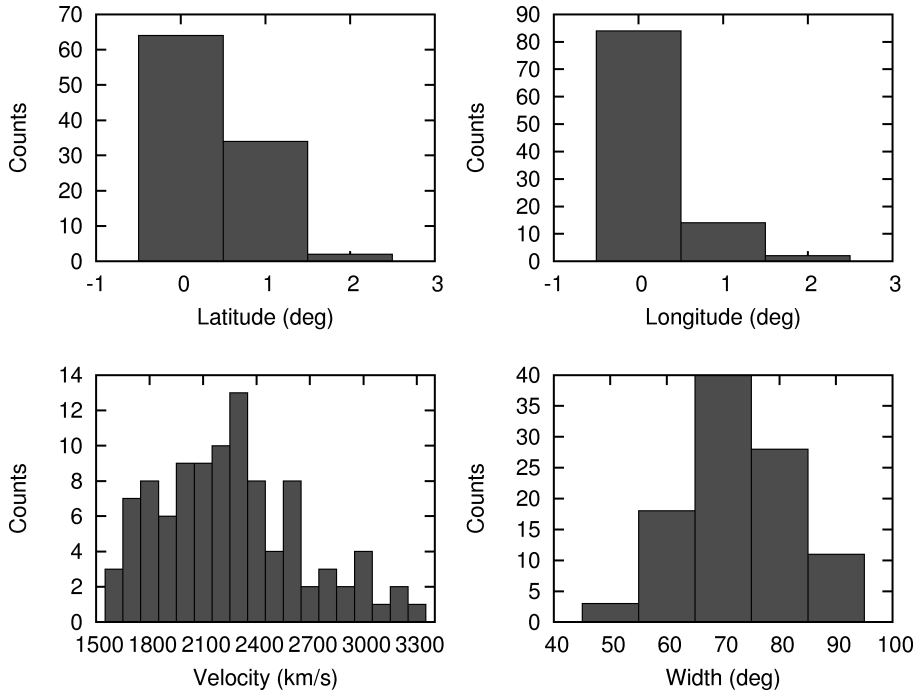

Figure 94. The input cone parameter distributions for the 28 Oct 2003 CME (event 10), derived from Coned Model version 1.3.

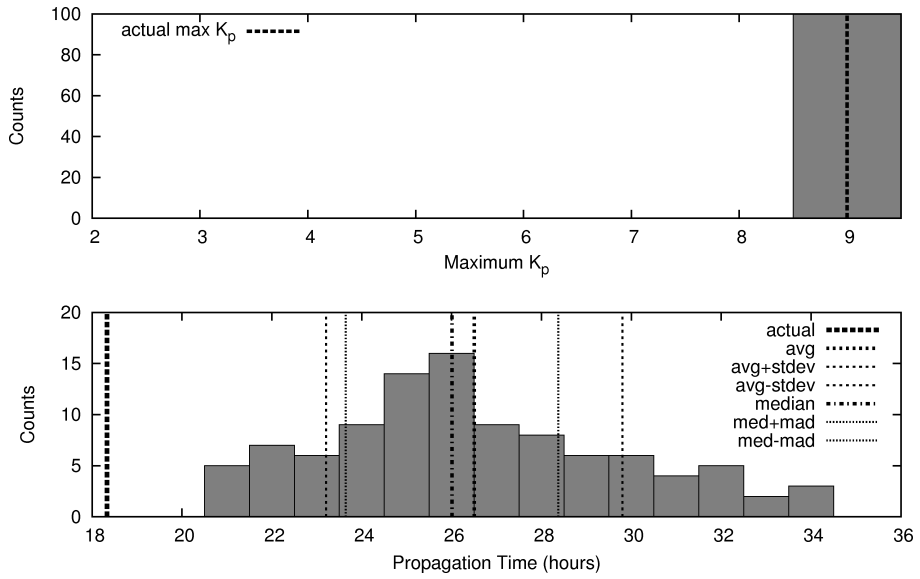

Figure 95. The propagation time and maximum $\mathrm{K_p}$ distributions for the 28 Oct 2003 CME (event 10). In this figure, *avg* stands for average, *stdev* stands for standard deviation, *med* stands for median, and *mad* stands for median absolute deviation.

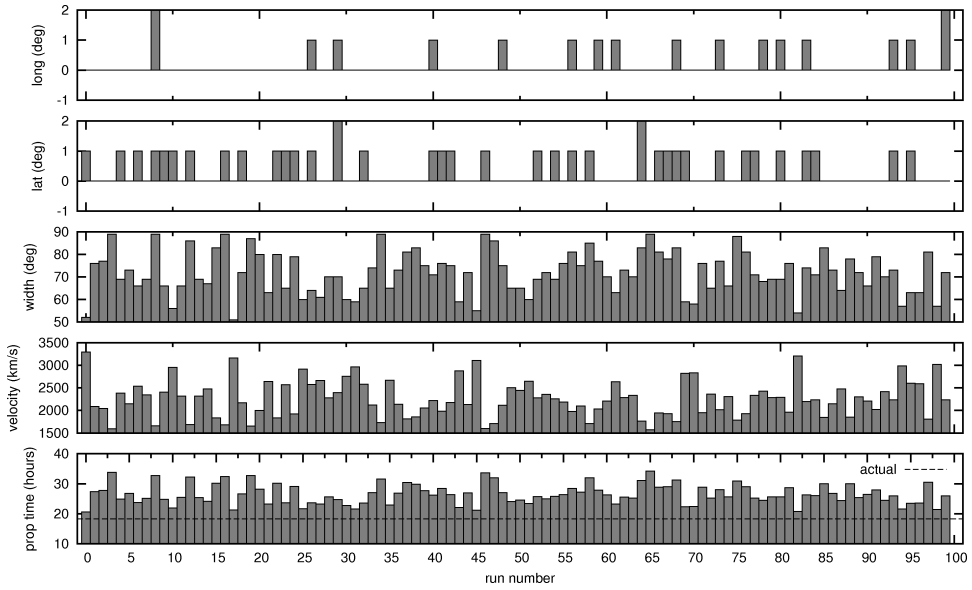

Figure 96. The 100 sets of cone parameters and propagation time forecasts composing the ensemble for the 28 Oct 2003 CME (event 10).

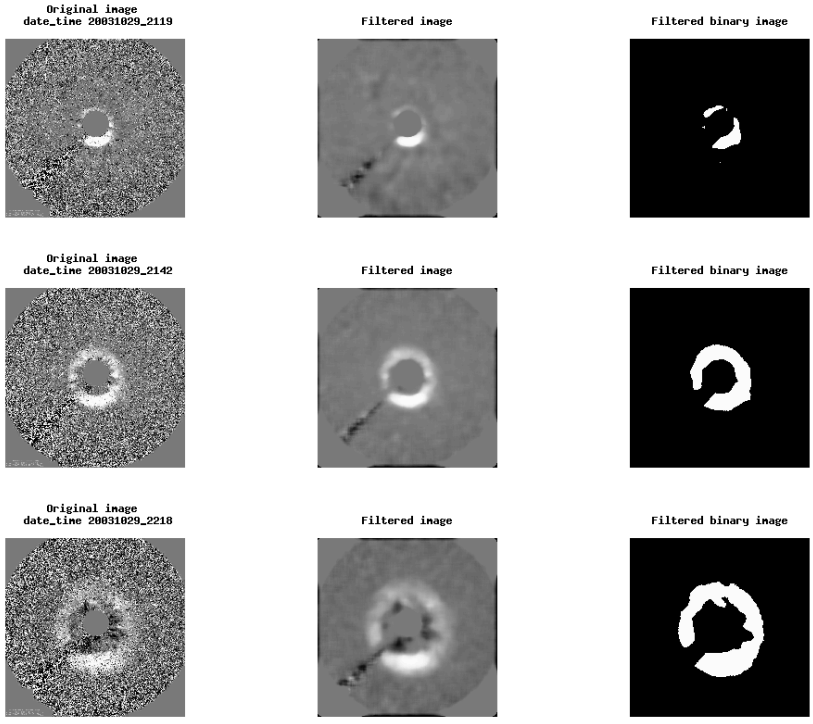

Figure 97. The filtered LASCO images for the 29 Oct 2003 CME (event 11), derived from Coned Model version 1.3.

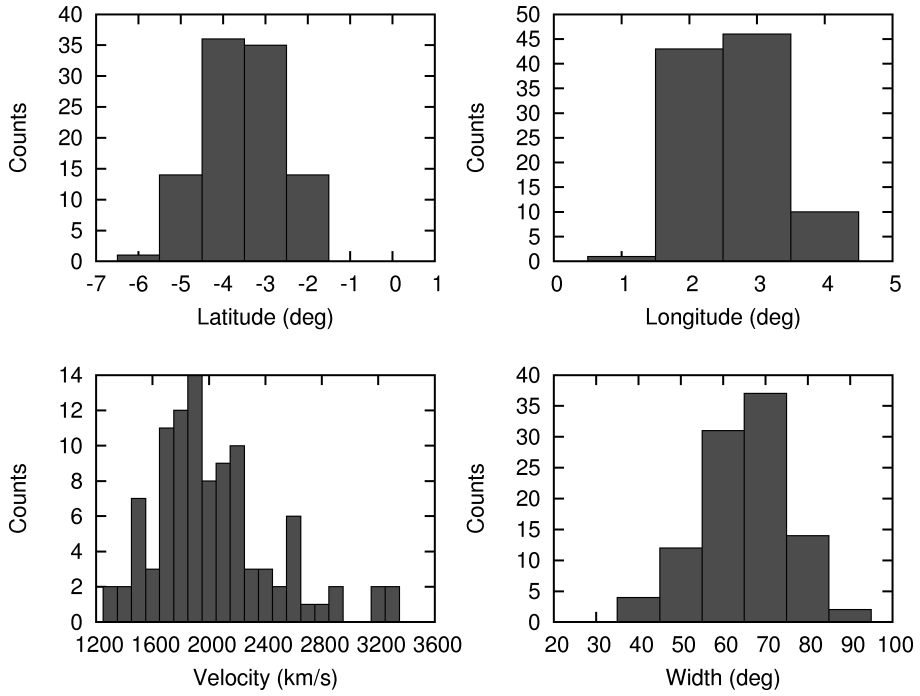

Figure 98. The input cone parameter distributions for the 29 Oct 2003 CME (event 11), derived from Coned Model version 1.3.

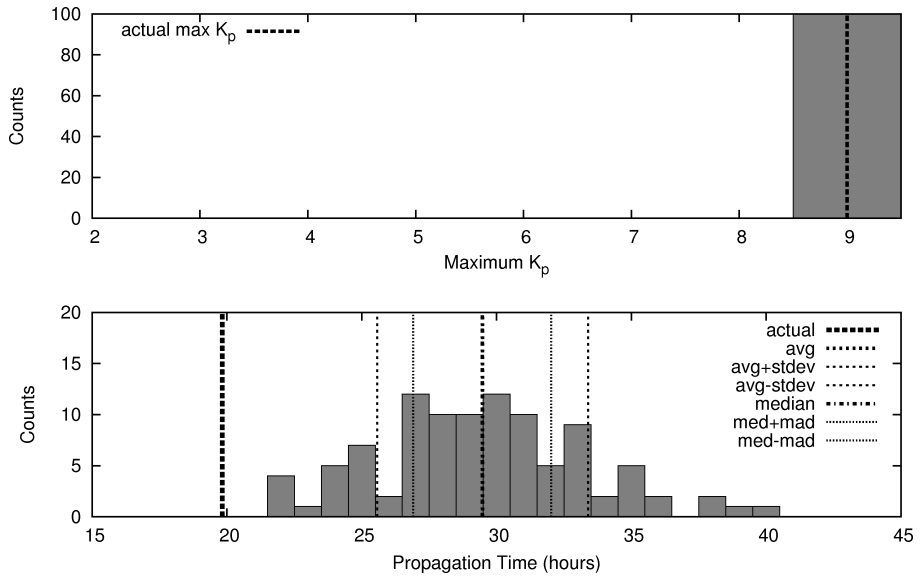

Figure 99. The propagation time and maximum $\mathrm{K_p}$ distributions for the 29 Oct 2003 CME (event 11). In this figure, *avg* stands for average, *stdev* stands for standard deviation, *med* stands for median, and *mad* stands for median absolute deviation.

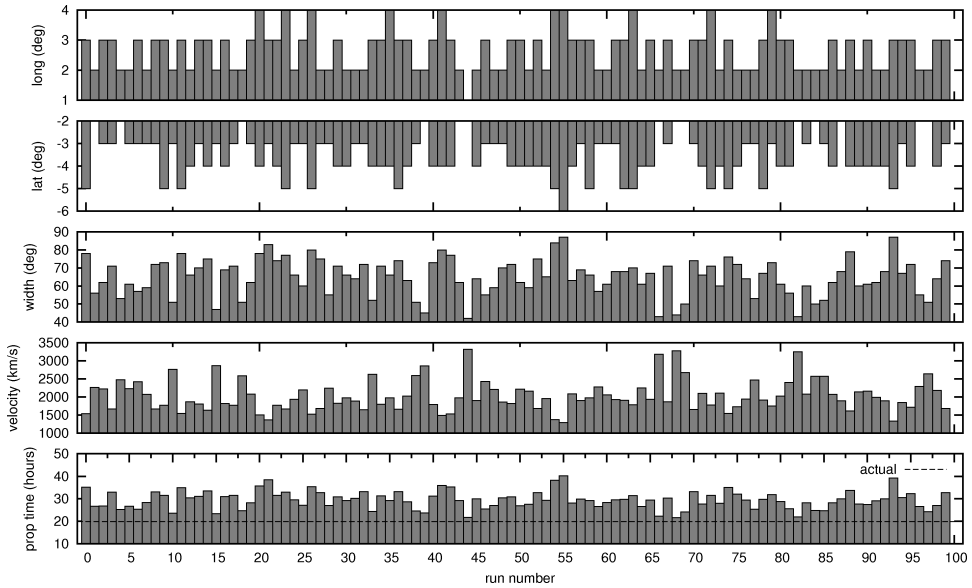

Figure 100. The 100 sets of cone parameters and propagation time forecasts composing the ensemble for the 29 Oct 2003 CME (event 11).

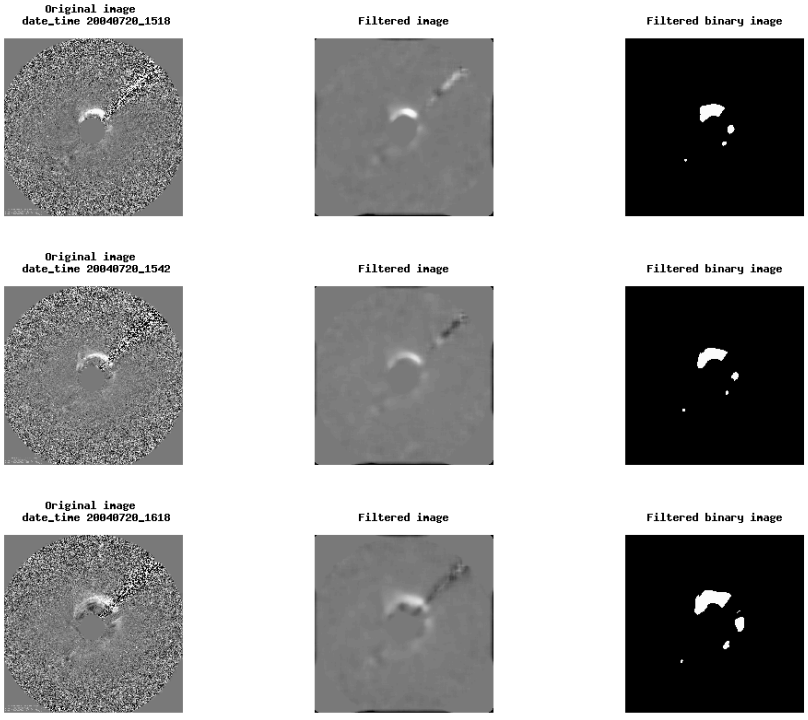

Figure 101. The filtered LASCO images for the 20 Jul 2004 CME (event 12), derived from Coned Model version 1.3.

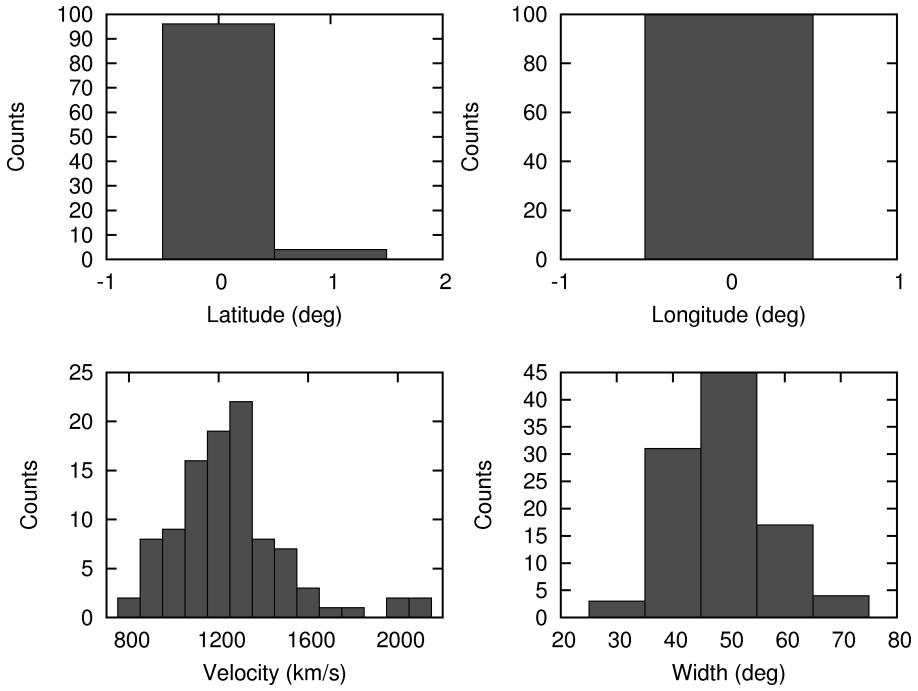

Figure 102. The input cone parameter distributions for the 20 Jul 2004 CME (event 12), derived from Coned Model version 1.3.

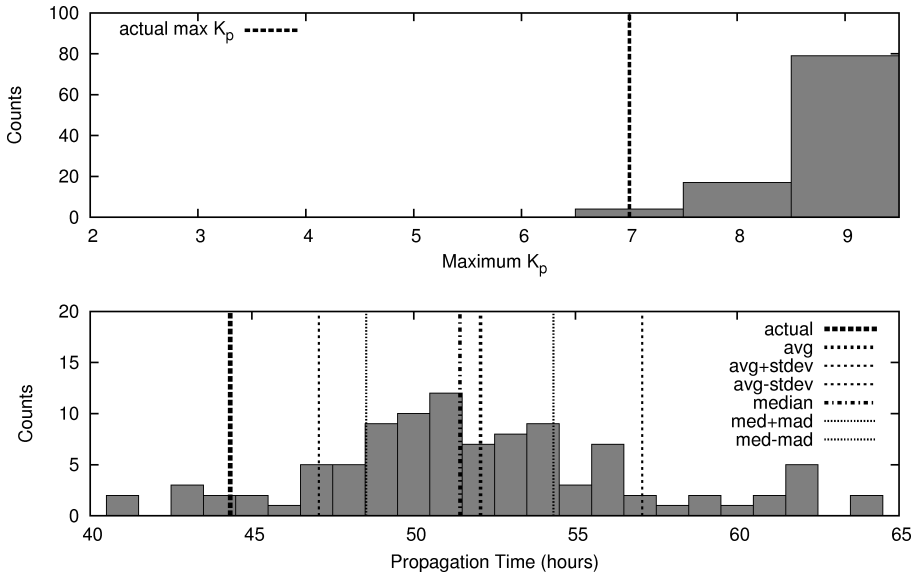

Figure 103. The propagation time and maximum $\mathrm{K_p}$ distributions for the 20 Jul 2004 CME (event 12). In this figure, *avg* stands for average, *stdev* stands for standard deviation, *med* stands for median, and *mad* stands for median absolute deviation.

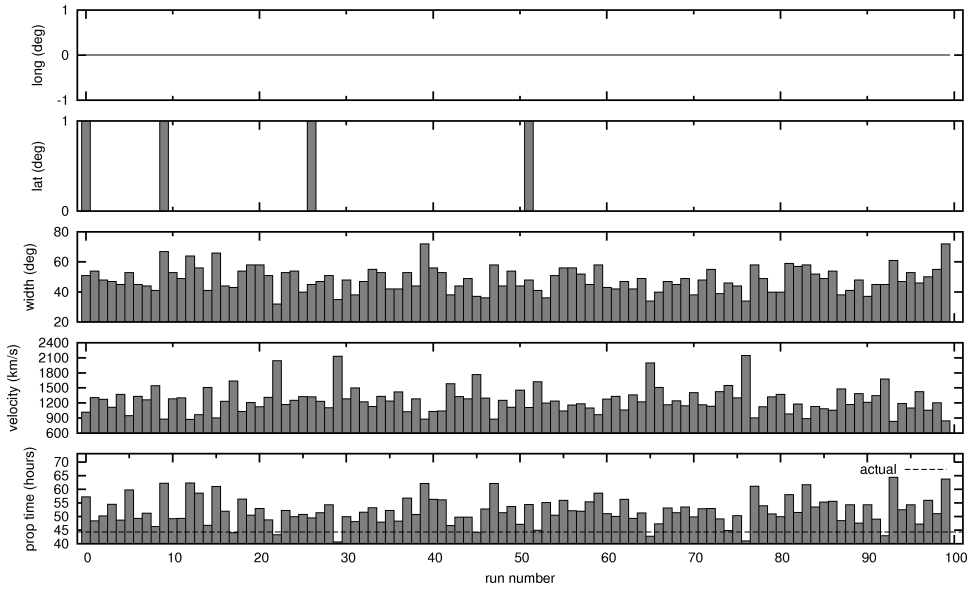

Figure 104. The 100 sets of cone parameters and propagation time forecasts composing the ensemble for the 20 Jul 2004 CME (event 12).

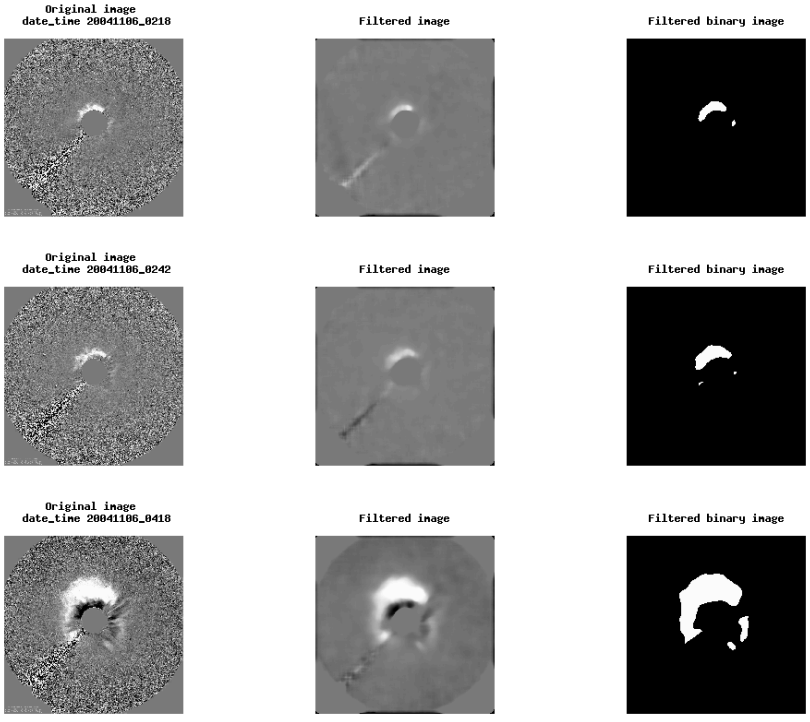

Figure 105. The filtered LASCO images for the 6 Nov 2004 CME (event 13), derived from Coned Model version 1.3.

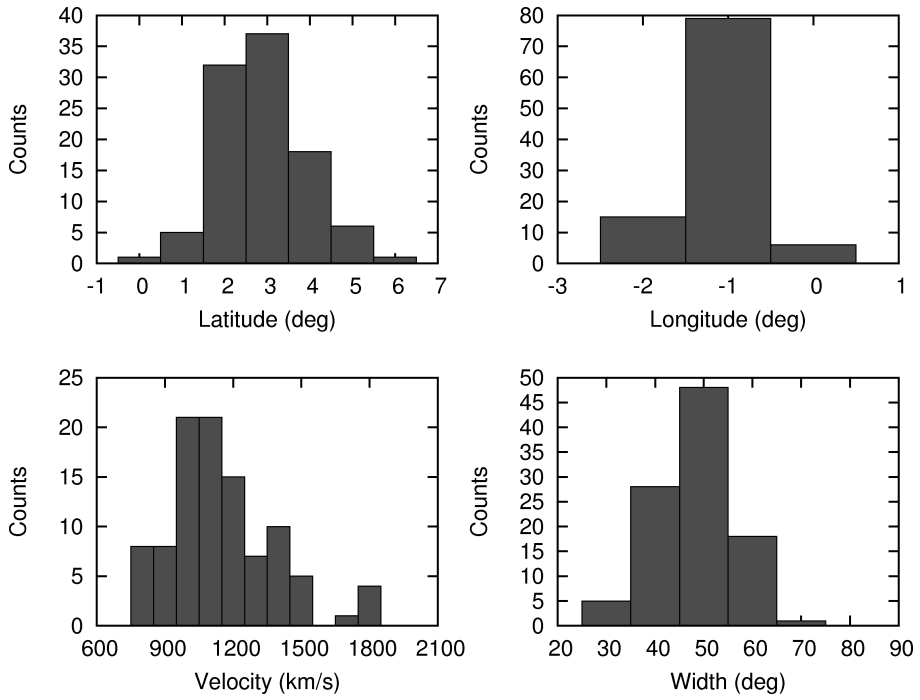

Figure 106. The input cone parameter distributions for the 6 Nov 2004 CME (event 13), derived from Coned Model version 1.3.

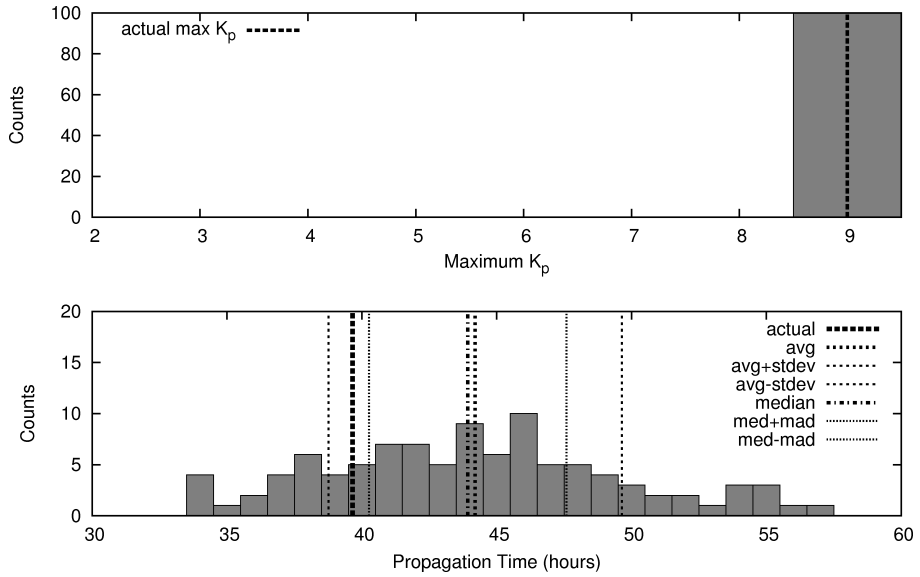

Figure 107. The propagation time and maximum $\mathrm{K_p}$ distributions for the 6 Nov 2004 CME (event 13). In this figure, *avg* stands for average, *stdev* stands for standard deviation, *med* stands for median, and *mad* stands for median absolute deviation.

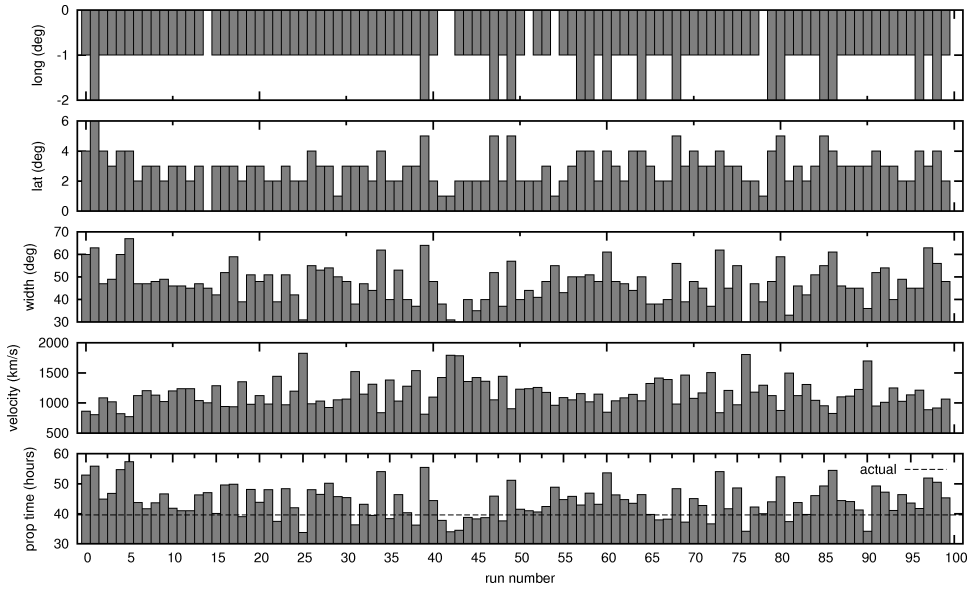

Figure 108. The 100 sets of cone parameters and propagation time forecasts composing the ensemble for the 6 Nov 2004 CME (event 13).

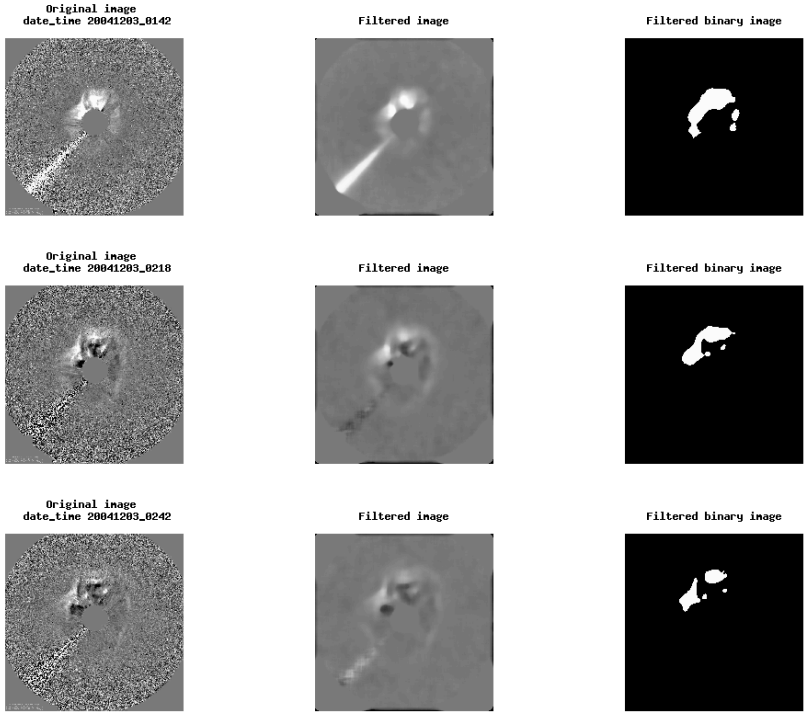

Figure 109. The filtered LASCO images for the 3 Dec 2004 CME (event 14), derived from Coned Model version 1.3.

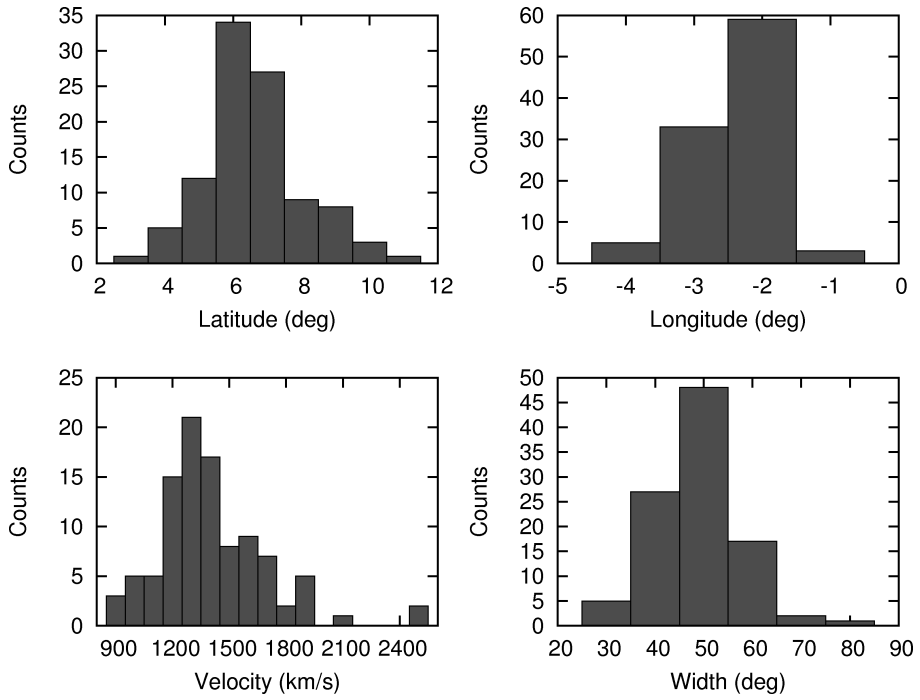

Figure 110. The input cone parameter distributions for the 3 Dec 2004 CME (event 14), derived from Coned Model version 1.3.

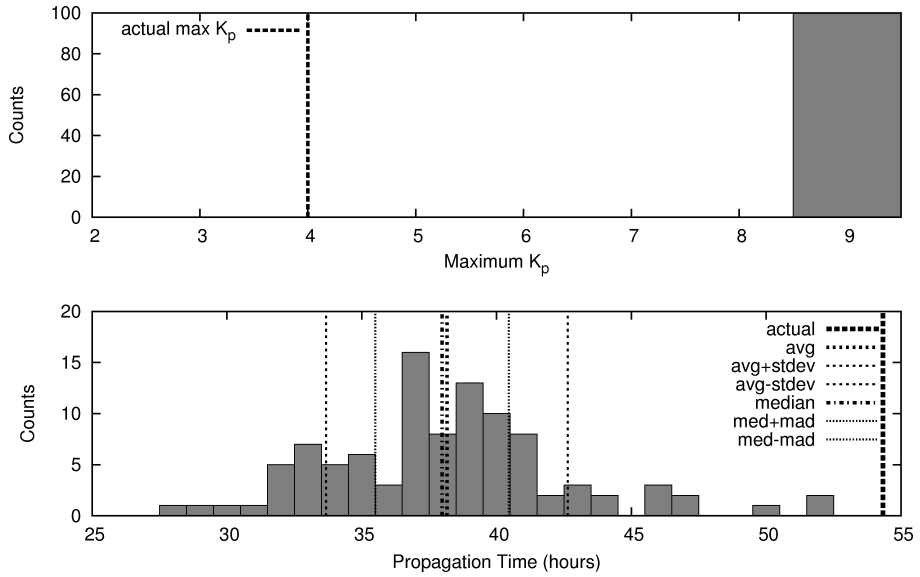

Figure 111. The propagation time and maximum $\mathrm{K_p}$ distributions for the 3 Dec 2004 CME (event 14). In this figure, *avg* stands for average, *stdev* stands for standard deviation, *med* stands for median, and *mad* stands for median absolute deviation.

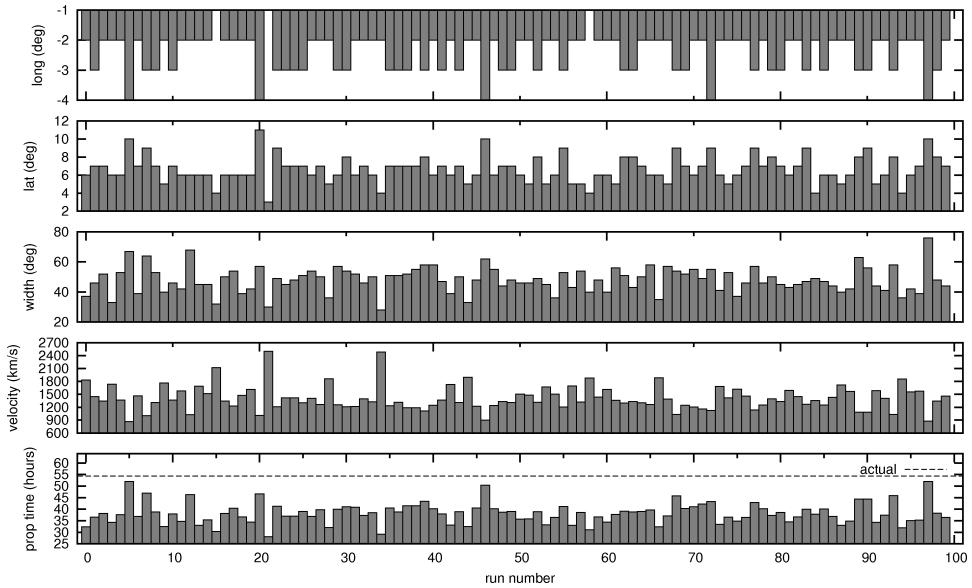

Figure 112. The 100 sets of cone parameters and propagation time forecasts composing the ensemble for the 3 Dec 2004 CME (event 14).

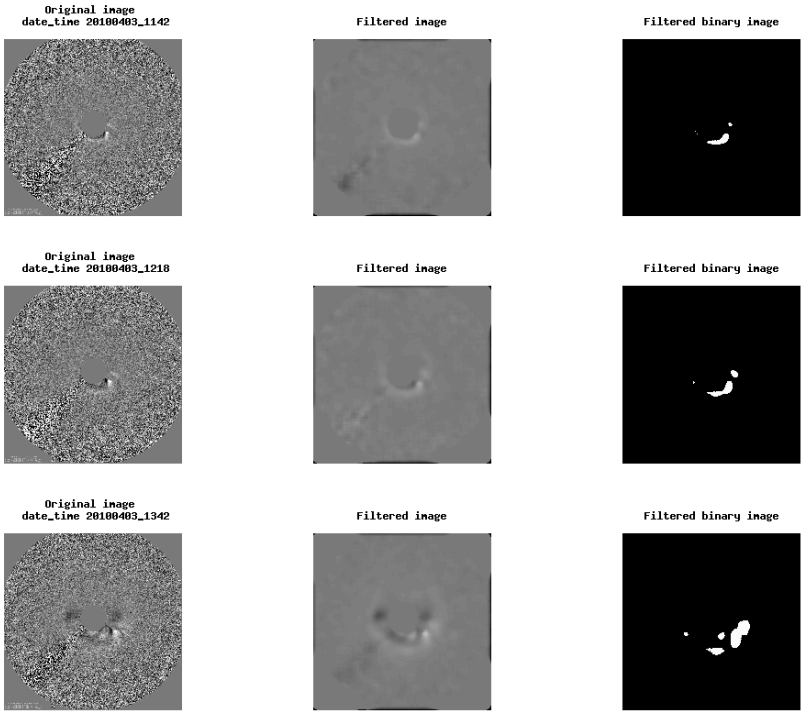

Figure 113. The filtered LASCO images for the 3 Apr 2010 CME (event 15), derived from Coned Model version 1.3.

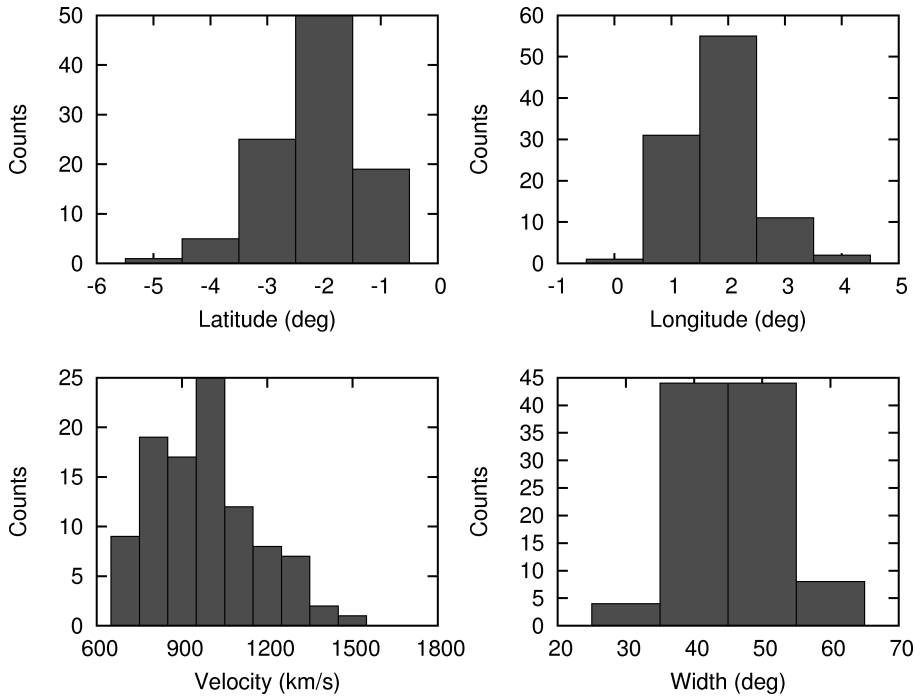

Figure 114. The input cone parameter distributions for the 3 Apr 2010 CME (event 15), derived from Coned Model version 1.3.

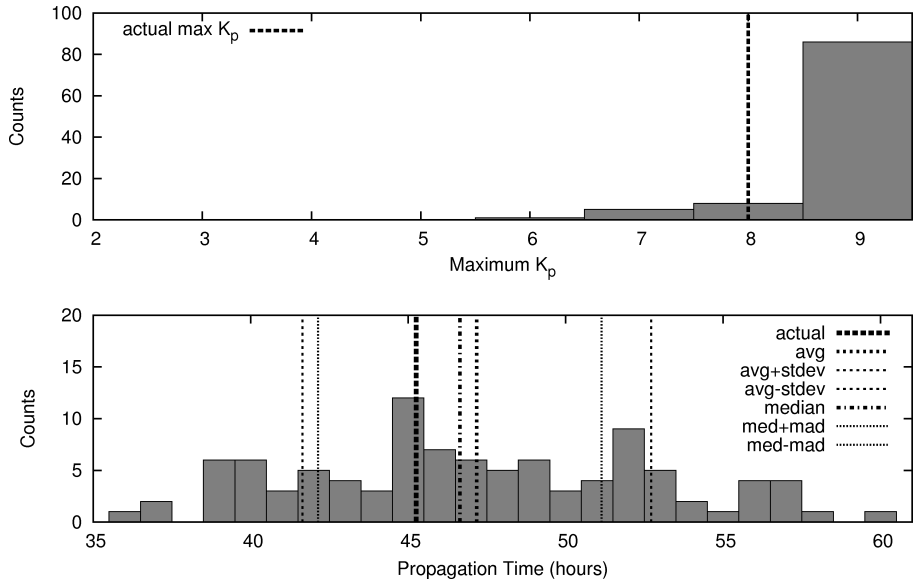

Figure 115. The propagation time and maximum $\mathrm{K_p}$ distributions for the 3 Apr 2010 CME (event 15). In this figure, *avg* stands for average, *stdev* stands for standard deviation, *med* stands for median, and *mad* stands for median absolute deviation.

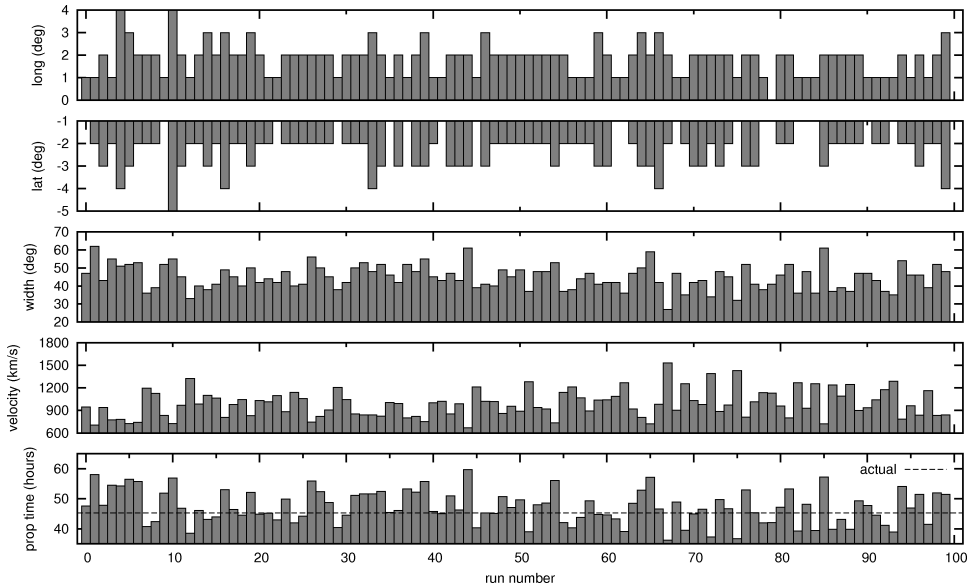

Figure 116. The 100 sets of cone parameters and propagation time forecasts composing the ensemble for the 3 Apr 2010 CME (event 15).

Appendix C. Coned Model Version 1.2 Input Parameters

The input parameter distributions, for the 15 CMEs, calculated with Coned Model version 1.2, are displayed in Tables 27 to 30. The averages and standard deviations of the input parameters, for each event, are displayed in Figure 117.

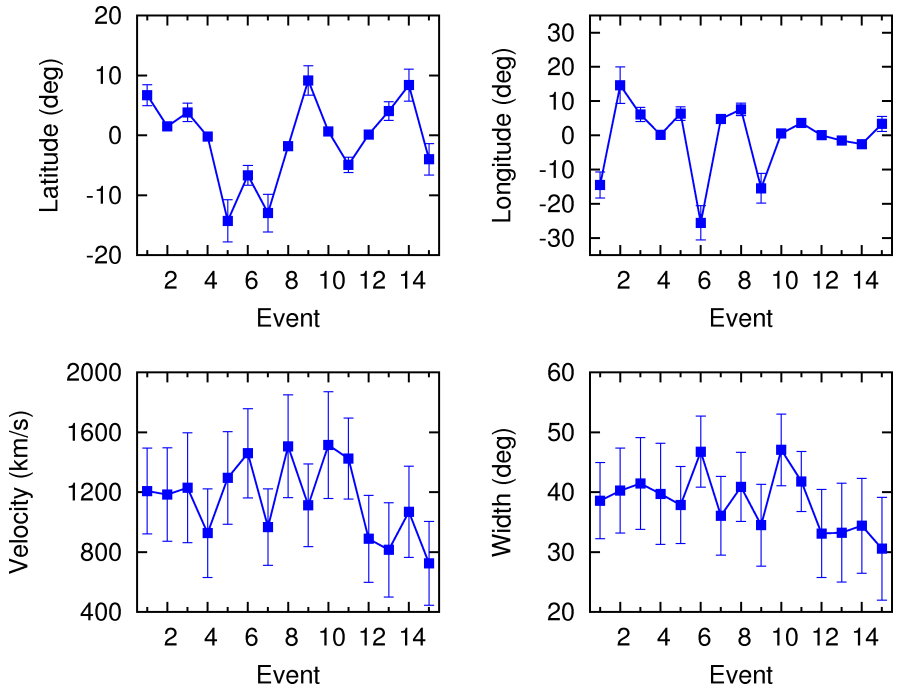

Figure 117. The averages and standard deviations of the input parameter distributions, for the 15 events, derived from Coned Model version 1.2.

Table 27. Statistics for the input velocity distributions of the 15 CMEs, using Coned Model version 1.2. The average and standard deviation of the columns are displayed at the bottom of the table.

CME date (YYYYMMDD)	average (km/s)	standard deviation (km/s)	median (km/s)	median absolute deviation (km/s)	range (km/s)	min (km/s)	max (km/s)
19990503	1207.74	286.86	1179.00	177.50	1550.00	661.00	2211.00
20000404	1183.50	312.20	1138.50	211.00	1627.00	723.00	2350.00
20000714	1229.53	367.21	1130.00	240.50	1725.00	610.00	2335.00
20010329	926.06	295.38	884.50	203.00	1606.00	458.00	2064.00
20010410	1294.95	308.66	1257.00	164.50	1652.00	723.00	2375.00
20010924	1459.95	297.79	1441.50	159.00	1574.00	944.00	2518.00
20011009	967.33	254.97	932.50	174.50	1241.00	539.00	1780.00
20011104	1506.66	343.42	1467.00	201.00	2051.00	1033.00	3084.00
20011117	1112.09	276.20	1073.00	170.50	1284.00	637.00	1921.00
20031028	1514.68	356.09	1457.50	231.50	1875.00	991.00	2866.00
20031029	1424.28	271.11	1373.00	174.00	1159.00	1005.00	2164.00
20040720	888.71	290.13	836.50	149.50	1633.00	498.00	2131.00
20041106	815.24	315.00	742.50	184.50	1585.00	431.00	2016.00
20041203	1068.97	304.06	1032.00	222.50	1836.00	454.00	2290.00
20100403	724.34	279.52	666.50	192.00	1211.00	333.00	1544.00
average	1154.94	303.91	1107.40	190.37	1573.93	669.33	2243.27
std	255.79	31.54	260.65	27.22	256.72	230.14	389.19

Table 28. Statistics for the input angular half-width distributions for the 15 CMEs, using Coned Model version 1.2. The average and standard deviation of the columns are displayed at the bottom of the table.

CME date (YYYYMMDD)	average (deg)	standard deviation (deg)	median (deg)	median absolute deviation (deg)	range (deg)	min (deg)	max (deg)
19990503	38.58	6.38	38.00	4.00	31.00	25.00	56.00
20000404	40.26	7.09	40.50	5.50	31.00	23.00	54.00
20000714	41.46	7.65	42.50	5.50	29.00	26.00	55.00
20010329	39.72	8.46	40.00	6.00	39.00	19.00	58.00
20010410	37.86	6.44	38.00	4.00	34.00	19.00	53.00
20010924	46.77	5.94	47.00	4.00	28.00	31.00	59.00
20011009	36.07	6.58	36.00	4.00	30.00	22.00	52.00
20011104	40.88	5.78	41.00	4.00	27.00	23.00	50.00
20011117	34.49	6.84	33.50	4.50	32.00	20.00	52.00
20031028	47.07	5.98	47.50	4.50	28.00	29.00	57.00
20031029	41.79	5.01	42.00	4.00	21.00	30.00	51.00
20040720	33.10	7.35	32.00	5.00	31.00	15.00	46.00
20041106	33.25	8.25	33.00	6.00	33.00	15.00	48.00
20041203	34.41	7.92	33.00	6.00	37.00	18.00	55.00
20041203	30.56	8.58	30.00	6.00	34.00	14.00	48.00
average	38.42	6.95	38.27	4.87	31.00	21.93	52.93
std	4.86	1.07	5.34	0.88	4.33	5.48	3.86

Table 29. Statistics for the input latitude distributions for the 15 CMEs, using Coned Model version 1.2. The average and standard deviation of the columns are displayed at the bottom of the table.

CME date (YYYYMMDD)	average (deg)	standard deviation (deg)	median (deg)	median absolute deviation (deg)	range (deg)	min (deg)	max (deg)
19990503	6.71	1.77	6.00	1.00	8.00	3.00	11.00
20000404	1.48	0.69	1.00	0.00	5.00	0.00	5.00
20000714	3.83	1.54	3.00	1.00	5.00	2.00	7.00
20010329	-0.21	0.46	0.00	0.00	2.00	-2.00	0.00
20010410	-14.27	3.53	-14.00	2.00	18.00	-24.00	-6.00
20010924	-6.65	1.65	-7.00	1.00	7.00	-11.00	-4.00
20011009	-12.97	3.13	-12.00	2.00	15.00	-22.00	-7.00
20011104	-1.83	0.70	-2.00	0.00	3.00	-4.00	-1.00
20011117	9.17	2.46	9.00	2.00	14.00	3.00	17.00
20031028	0.68	0.69	1.00	1.00	3.00	0.00	3.00
20031029	-4.93	1.26	-5.00	1.00	6.00	-8.00	-2.00
20040720	0.15	0.41	0.00	0.00	2.00	0.00	2.00
20041106	4.04	1.56	4.00	1.00	6.00	1.00	7.00
20041203	8.38	2.67	8.00	1.00	15.00	3.00	18.00
20041203	-4.01	2.63	-3.00	1.00	14.00	-15.00	-1.00
average	-0.70	1.68	-0.73	0.93	8.20	-4.93	3.27
std	7.00	1.01	6.69	0.70	5.47	9.09	7.64

Table 30. Statistics for the input longitude distributions for the 15 CMEs, using Coned Model version 1.2. The average and standard deviation of the columns are displayed at the bottom of the table.

CME date (YYYYMMDD)	average (deg)	standard deviation (deg)	median (deg)	median absolute deviation (deg)	range (deg)	min (deg)	max (deg)
19990503	-14.52	3.80	-14.00	2.00	18.00	-26.00	-8.00
20000404	14.64	5.35	14.00	3.00	24.00	6.00	30.00
20000714	6.11	2.03	6.00	2.00	8.00	3.00	11.00
20010329	0.16	0.37	0.00	0.00	1.00	0.00	1.00
20010410	6.38	1.98	6.00	1.00	11.00	2.00	13.00
20010924	-25.60	5.01	-25.00	4.00	23.00	-37.00	-14.00
20011009	4.80	1.32	5.00	1.00	8.00	2.00	10.00
20011104	7.59	1.84	7.00	1.00	8.00	4.00	12.00
20011117	-15.45	4.37	-15.00	3.00	26.00	-31.00	-5.00
20031028	0.51	0.75	0.00	0.00	3.00	0.00	3.00
20031029	3.59	0.87	4.00	1.00	4.00	2.00	6.00
20040720	0.00	0.00	0.00	0.00	0.00	0.00	0.00
20041106	-1.54	0.64	-1.50	0.50	3.00	-3.00	0.00
20041203	-2.54	0.88	-2.00	0.00	5.00	-6.00	-1.00
20041203	3.35	2.16	3.00	1.00	12.00	1.00	13.00
average	-0.83	2.09	-0.83	1.30	10.27	-5.53	4.73
std	10.35	1.74	10.03	1.25	8.62	13.80	10.69

Bibliography

Afraimovich, E., V. Demyanov, and T. Kondakova, Degradation of GPS performance in geomagnetically disturbed conditions, *GPS Solutions*, *7*(2), 109–119, 2003.

Arge, C., and V. Pizzo, Improvement in the prediction of solar wind conditions using near-real time solar magnetic field updates, *Journal of geophysical research*, *105*, 10, 2000.

Boteler, D., R. Pirjola, and H. Nevanlinna, The effects of geomagnetic disturbances on electrical systems at the Earth's surface, *Advances in Space Research*, *22*(1), 17–27, 1998.

Chen, P., Coronal mass ejections: Models and their observational basis, *Living Reviews in Solar Physics*, *8*, 2011.

Cyr, O., et al., Properties of coronal mass ejections: Soho lasco observations from january 1996 to june 1998, *Journal of Geophysical Research*, *105*(A8), 18,169–18, 2000.

DelSole, T., Predictability and information theory. part ii: Imperfect forecasts, *Journal of the atmospheric sciences*, *62*(9), 3368–3381, 2005.

Dryer, M., Interplanetary shock waves generated by solar flares, *Space Science Reviews*, *15*(4), 403–468, 1974.

Emslie, A., et al., Energy partition in two solar flare/CME events, *Journal of geophysical research*, *109*(A10), A10,104, 2004.

Falkenberg, T., A. Taktakishvili, A. Pulkkinen, S. Vennerstrom, D. Odstrcil, D. Brain, G. Delory, and D. Mitchell, Evaluating predictions of icme arrival at earth and mars, *Space Weather*, *9*(9), S00E12, 2011.

Forbes, T., A review on the genesis of coronal mass ejections, *Journal of geophysical research*, *105*(23153), 79, 2000.

Forbes, T., et al., CME theory and models, *Coronal Mass Ejections*, pp. 251–302, 2006.

Foukal, P. V., *Solar Astrophysics, 2nd, Revised Edition*, WILEY-VCH, 2004.

Goerss, J., Tropical cyclone track forecasts using an ensemble of dynamical models, *Monthly Weather Review*, *128*(4), 1187–1193, 2000.

Gopalswamy, N., and M. Kundu, Estimation of the mass of a coronal mass ejection from radio observations, *Astrophysical Journal*, *390*, L37–L39, 1992.

Gopalswamy, N., A. Lara, R. Lepping, M. Kaiser, D. Berdichevsky, and O. Cyr, Interplanetary acceleration of coronal mass ejections, *Geophysical research letters*, *27*(2), 145–148, 2000.

Gopalswamy, N., A. Lara, S. Yashiro, M. Kaiser, and R. Howard, Predicting the 1-au arrival times of coronal mass ejections, *Journal of Geophysical Research. A. Space Physics*, *106*, 29, 2001.

Gopalswamy, N., A. Lara, S. Yashiro, S. Nunes, and R. Howard, Coronal mass ejection activity during solar cycle 23, in *Solar Variability as an Input to the Earth's Environment*, vol. 535, pp. 403–414, 2003.

Gopalswamy, N., A. Lara, P. Manoharan, and R. Howard, An empirical model to predict the 1-au arrival of interplanetary shocks, *Advances in Space Research*, *36*(12), 2289–2294, 2005.

Gosling, J., The solar flare myth, *Journal of geophysical research*, *98*(A11), 18,937–18, 1993.

Hill, T., and P. Lewicki, Statistics methods and applications. tulsa, ok: Statsoft, 2007.

Hilmer, R., Af-geospace user's manual version 2.0 and version 2.0p, *by Air Force Research Laboratory*, 2001.

House, L., W. Wagner, E. Hildner, C. Sawyer, and H. Schmidt, Studies of the corona with the Solar Maximum Mission coronagraph/polarimeter, *The Astrophysical Journal*, *244*, L117–L121, 1981.

Howard, R., A historical perspective on coronal mass ejections, *GEOPHYSICAL MONOGRAPH-AMERICAN GEOPHYSICAL UNION*, *165*, 7, 2006.

Hudson, H., L. Acton, and S. Freeland, A long-duration solar flare with mass ejection and global consequences, *The Astrophysical Journal*, *470*, 629, 1996.

Hundhausen, A., C. Sawyer, L. House, R. Illing, and W. Wagner, Coronal mass ejections observed during the solar maximum mission: Latitude distribution and rate of occurrence, *Journal of Geophysical Research*, *89*(A5), 2639–2646, 1984.

Illing, R., and A. Hundhausen, Observation of a coronal transient from 1.2 to 6 solar radii, *Journal of Geophysical Research*, *90*(A1), 275–282, 1985.

Jackson, B., Imaging of coronal mass ejections by the Helios spacecraft, *Solar physics*, *100*(1), 563–574, 1985.

Klein, L., and L. Burlaga, Interplanetary magnetic clouds at 1 AU, *Journal of Geophysical Research*, *87*(A2), 613–624, 1982.

Leith, C., Theoretical skill of monte carlo forecasts(stochastic atmospheric processes), *Monthly Weather Review*, *102*, 409–418, 1974.

Lorenz, E., Deterministic nonperiodic flow1, *Atmos J Sci*, *20*, 130–141, 1963.

MacQueen, R., J. Eddy, J. Gosling, E. Hildner, R. Munro, G. Newkirk Jr, A. Poland, and C. Ross, The outer solar corona as observed from Skylab: preliminary results, *The Astrophysical Journal*, *187*, L85, 1974.

Newell, P., T. Sotirelis, K. Liou, C. Meng, and F. Rich, A nearly universal solar wind-magnetosphere coupling function inferred from 10 magnetospheric state variables, *J. Geophys. Res*, *112*, 1–16, 2007.

Odstrcil, D., Modeling 3-D solar wind structure, *Advances in Space Research*, *32*(4), 497–506, 2003.

Odstrčil, D., and V. Pizzo, Three-dimensional propagation of coronal mass ejections (CMEs) in a structured solar wind flow 1. CME launched within the streamer belt, *Journal of geophysical research*, *104*(A1), 483–492, 1999.

Odstrcil, D., P. Riley, and X. Zhao, Numerical simulation of the 12 may 1997 interplanetary cme event, *J. Geophys. Res*, *109*, A02,116, 2004.

Odstrcil, D., V. Pizzo, and C. Arge, Propagation of the 12 may 1997 interplanetary coronal mass ejection in evolving solar wind structures, *Journal of geophysical research*, *110*(A2), A02,106, 2005.

Owens, M., P. Cargill, C. Pagel, G. Siscoe, and N. Crooker, Characteristic magnetic field and speed properties of interplanetary coronal mass ejections and their sheath regions, *J. Geophys. Res*, *110*, 105, 2005.

Peduzzi, P., J. Concato, E. Kemper, T. Holford, and A. Feinstein, A simulation study of the number of events per variable in logistic regression analysis, *Journal of clinical epidemiology*, *49*(12), 1373–1379, 1996.

Prölss, G., *Physics of the Earth's space environment: an introduction*, Springer Verlag, 2004.

Pulkkinen, A., private communication, 2011.

Pulkkinen, A., T. Oates, and A. Taktakishvili, Automatic determination of the conic coronal mass ejection model parameters, *Solar Physics*, *261*(1), 115–126, 2010.

Raychaudhuri, P., Variability of Coronal Mass Ejections, *Proceedings of the International Astronomical Union*, *2004*(IAUS226), 211–212, 2004.

Riley, P., J. Linker, and Z. Mikić, An empirically-driven global mhd model of the solar corona and inner heliosphere, *Journal of geophysical research*, *106*(A8), 15,889–15, 2001.

Robbrecht, E., D. Berghmans, and R. Van der Linden, Automated LASCO CME catalog for solar cycle 23: are CMEs scale invariant?, *The Astrophysical Journal*, *691*, 1222, 2009.

Rycroft, M. J., and S. K. Runcorn (Eds.), *The Solar Corona*, 1973.

Sivillo, J., J. Ahlquist, and Z. Toth, An ensemble forecasting primer, *Weather and Forecasting*, *12*(4), 809–818, 1997.

Smith, Z., and M. Dryer, Mhd study of temporal and spatial evolution of simulated interplanetary shocks in the ecliptic plane within 1 au, *Solar Physics*, *129*(2), 387–405, 1990.

Spaulding, J., Predicting solar protons: A statistical approach, *Tech. rep.*, DTIC Document, 2009.

Taktakishvili, A., private communication, 2011.

Taktakishvili, A., M. Kuznetsova, P. MacNeice, M. Hesse, L. Rastatter, A. Pulkkinen, A. Chulaki, and D. Odstrcil, Validation of the coronal mass ejection predictions at the earth orbit estimated by enlil heliosphere cone model, *Space Weather*, *7*, 2009.

Taktakishvili, A., P. MacNeice, and D. Odstrcil, Model uncertainties in predictions of arrival of coronal mass ejections at earth orbit, *Space Weather*, *8*(6), S06,007, 2010.

Taktakishvili, A., A. Pulkkinen, P. MacNeice, M. Kuznetsova, M. Hesse, and D. Odstrcil, Modeling of coronal mass ejections that caused particularly large geomagnetic storms using enlil heliosphere cone model, *Space Weather*, *9*(6), S06,002, 2011.

Tascione, T. F., *Introduction to the space environment*, Krieger Publishing Company Malabar, Florida, 1994.

Thomas, J., *Numerical partial differential equations*, Springer, 1995.

Tóth, G., and D. Odstrcil, Comparison of some flux corrected transport and total variation diminishing numerical schemes for hydrodynamic and magnetohydrodynamic problems, *Journal of Computational Physics*, *128*(1), 82–100, 1996.

Wang, Y., and J. Zhang, A comparative study between eruptive X-class flares associated with coronal mass ejections and confined X-class flares, *The Astrophysical Journal*, *665*, 1428, 2007.

Wang, Y., N. Sheeley, et al., Observations of correlated white-light and extreme-ultraviolet jets from polar coronal holes, *The Astrophysical Journal*, *508*, 899, 1998.

Webb, D., and A. Hundhausen, Activity associated with the solar origin of coronal mass ejections, *Solar physics*, *108*(2), 383–401, 1987.

Wenzel, W., and K. Hamacher, Stochastic tunneling approach for global minimization of complex potential energy landscapes, *Physical Review Letters*, *82*(15), 3003–3007, 1999.

Xie, H., L. Ofman, and G. Lawrence, Cone model for halo CMEs: Application to space weather forecasting, *Journal of geophysical research*, *109*(A3), A03,109, 2004.

Yashiro, S., N. Gopalswamy, G. Michalek, O. Cyr, S. Plunkett, N. Rich, and R. Howard, A catalog of white light coronal mass ejections observed by the SOHO spacecraft, *Journal of geophysical research*, *109*(A7), A07,105, 2004.

Yashiro, S., N. Gopalswamy, S. Akiyama, G. Michalek, and R. Howard, Visibility of coronal mass ejections as a function of flare location and intensity, *J. Geophys. Res*, *110*(A12), 2005.

Zhang, J., K. Dere, R. Howard, M. Kundu, and S. White, On the temporal relationship between coronal mass ejections and flares, *The Astrophysical Journal*, *559*, 452, 2001.

Zhao, X., J. Hoeksema, and P. Scherrer, Modeling boot-shaped coronal holes using soho-mdi magnetic measurements, in *Fifth SOHO Workshop: The Corona and Solar Wind Near Minimum Activity*, vol. 404, p. 751, 1997.

Zhao, X., S. Plunkett, and W. Liu, Determination of geometrical and kinematical properties of halo coronal mass ejections using the cone model, *J. Geophys. Res*, *107*(1223), 10–1029, 2002.

Vita

Capt Daniel Emmons was born in 29 Palms, CA in 1983. The rest is history.

REPORT DOCUMENTATION PAGE

Form Approved
OMB No. 0704–0188

1. REPORT DATE *(DD–MM–YYYY)*	2. REPORT TYPE	3. DATES COVERED *(From — To)*
22–03–2012	Master's Thesis	Aug 2010 — Mar 2012

4. TITLE AND SUBTITLE

Ensemble Forecasting of Coronal Mass Ejections Using the WSA-ENLIL with Coned Model

5a. CONTRACT NUMBER

5b. GRANT NUMBER

5c. PROGRAM ELEMENT NUMBER

6. AUTHOR(S)

Emmons II, Daniel J., Captain, USAF

5d. PROJECT NUMBER

5e. TASK NUMBER

5f. WORK UNIT NUMBER

7. PERFORMING ORGANIZATION NAME(S) AND ADDRESS(ES)

Air Force Institute of Technology
Graduate School of Engineering and Management (AFIT/EN)
2950 Hobson Way
WPAFB OH 45433-7765

8. PERFORMING ORGANIZATION REPORT NUMBER

AFIT/APPLPHY/ENP/12-M04

9. SPONSORING / MONITORING AGENCY NAME(S) AND ADDRESS(ES)

Antti Pulkkinen
NASA - Goddard Space Flight Center
Greenbelt, MD 20771
301-286-0652 antti.a.pulkkinen@nasa.gov

10. SPONSOR/MONITOR'S ACRONYM(S)

NASA/GSFC

11. SPONSOR/MONITOR'S REPORT NUMBER(S)

12. DISTRIBUTION / AVAILABILITY STATEMENT

APPROVED FOR PUBLIC RELEASE; DISTRIBUTION UNLIMITED.

13. SUPPLEMENTARY NOTES

14. ABSTRACT

The combination of the Wang-Sheeley-Arge (WSA) coronal model, ENLIL heliospherical model version 2.7, and Coned Model version 1.3 (WSA-ENLIL with Coned Model) was employed to form ensemble forecasts for 15 halo coronal mass ejections (CME's). The input parameter distributions were formed from 100 sets of CME cone parameters derived from the Coned Model. The Coned Model employed image processing along with the bootstrap approach to automatically calculate cone parameter distributions from SOHO-LASCO imagery based on techniques described by *Pulkkinen et al.* [2010]. The input parameter distributions were used as input to WSA-ENLIL to calculate the temporal evolution of the CME's, which were analyzed to determine the propagation times to the L_1 Lagrangian point and the maximum K_p indices due to the impact of the CME's on the Earth's magnetosphere. The *Newell et al.* [2007] maximum K_p index formula was employed to calculate the maximum K_p indices based on the solar wind parameters near Earth.

15. SUBJECT TERMS

Coronal Mass Ejection, Ensemble Forecasting, WSA-ENLIL with Coned Model

16. SECURITY CLASSIFICATION OF:			17. LIMITATION OF ABSTRACT	18. NUMBER OF PAGES	19a. NAME OF RESPONSIBLE PERSON
a. REPORT	b. ABSTRACT	c. THIS PAGE			Lt Col Ariel O. Acebal
U	U	U	U	191	19b. TELEPHONE NUMBER *(include area code)* (937) 255-3636, x4518; ariel.acebal@afit.edu